5

Field-Block Scale

The field-block scale represents the largest scale which is investigated experimentally in this context. The installation of an in-situ test site allows all experimental approaches to be employed on the field-block scale in a certain area of the real aquifer. In this manner, it becomes possible to check the scale-dependence and assignability of core-scale or bench-scale results to almost natural aquifer conditions. Thus, the idea behind investigations on the field-block scale is to create a link between the experimental results on the core- or bench-scale and the real aquifer environment. Depending on the geological characteristics of the system under investigation and on the kind of experiment, the size of the chosen area has significant influence on the transferability of the evaluated data to the real aquifer. To make this upscaling-process possible, the investigated area should ideally describe at least one representative elemental volume (Luckner and Schestakow (1986)) of the whole heterogeneous aquifer system. The size of this REV has to be chosen individually in each case and depends primarily on the characteristics of the fracture system such as orientation, density and length of fractures.

Usually, fractured porous aquifers are not readily accessible without major expenses incurred by drilling and sampling. Therefore, an approach involving an equivalent system above ground was chosen for the tests under controlled boundary conditions. This hard-rock aquifer-analogue approach is based on the investigation of accessible outcrops of the aquifer material in the unsaturated zone such as can be found in a quarry. Their sedimentological and lithological properties can be considered to be analogous to the less accessible groundwater system at greater depth.

5.1 Choice of the Field Block Location

C. Thüringer, M. Weede, H. Hötzl

The test site has to fulfil two conditions: on the one hand, the rock matrix porosity should be exceptionally high and, on the other, the material should be fractured densely and as homogeneously as possible. The local infrastructure had to be kept in mind as well. The search thus soon concentrated on quarries of Middle- or Upper Triassic sandstones in the central and southern parts of Germany.

5.1.1 Regional Positioning

The search for a suitable location of the test site was subject to the following fundamental criteria. For both geological and technical reasons, the best place to set up a hard-rock test site is generally an active quarry. There, it is likely that the chosen cutout of the hard-rock aquifer has been exposed to weathering processes for only a short period of time. In addition, the infrastructure necessary to install and operate a hydrogeological test site is usually available at an operating quarry, with water and power supply and sufficient access roads.

The rock material to be investigated should preferably have both a high matrix porosity and a homogeneously distributed and dense fracture system. Thus, the Triassic sandstones of *Buntsandstein* and *Keuper* in Baden-Württemberg were shortlisted. Table 5.1 gives an overview of the physical properties of the various sandstones initially selected.

A comparison of the data shows that the *Buntsandstein* of the Southern Black Forest (Lahr District) and the *Schilfsandstein* of the *Kraichgau* seem to have the highest matrix porosities of 18 % to 21 %. In contrast, sandstones of the *Odenwald* and the greater part of the *Stubensandstein* of the Pliezhausen area show comparably low porosities of only 13 %.

In order to choose a suitable location for the test site, an inquiry concerning active sandstone quarries in Baden-Württemberg was undertaken with the following criteria:

- densely and homogeneously fractured hard rock with as high a matrix porosity as possible;
- absence of single fractures significantly dominating flow and transport;
- availability of the location and its infrastructure for the duration of the project;
- possibility of excavating a fresh cut from the rock formation.

Initially, all the active sandstone quarries in Baden-Württemberg were registered. Böttger (1989) collected the data of 22 active quarries in all: *Buntsandstein* (7 quarries), *Schilfsandstein* (11 quarries), *Stubensandstein* and

Table 5.1. Physical properties of selected sandstone quarries in Baden-Württemberg (Grimm (1990), Kulke (1967), Ufrecht (1987)).

Formation	Name	Stratigraphic Horizon	Density [g/cm^3]	Porosity [Vol.-%]	Max. Water Absorption [Vol.-%]
Buntsandstein	Lahrer Sandstein	su	2.16	18.29	18.29
	Neckartäler, red	su	2.25	15.23	15.23
	Neckartäler, red-white	su	2.33	11.83	11.83
Schilfsandstein	Maulbronner Sandstein	km2	2.19	15.3	-
	Pfaffenhofener Sandstein	km2	2.00	21.1	-
	Niederhofener Sandstein	km2	2.06	17.9	-
	Weiler Sandstein	km2	2.15	18.1	-
	Mühlbacher Sandstein	km2	2.15	15.9	-
Stubensandstein	Pliezhausener Sandstein (Lower Bed)	km4	2.31	13.77	13.77
	White Variety	km4	-	-	13.5
	Yellow Variety	km4	-	-	17.2
Stubensandstein	Pliezhausener Sandstein (Upper Bed)	km4	2.24	21.5	20.6

Rötsandstein (together 4 quarries). The resources database of the Geological Survey of Baden-Württemberg (LGRB) listed 21 companies with 26 active sandstone quarries in early 1995. Eleven of these quarries were working *Buntsandstein*, 12 *Schilfsandstein* (Middle Keuper, km2) and one each *Stubensandstein* (Middle Keuper, km4), *Schilfsandstein* (Upper Keuper, ko), and *Lettenkohlensandstein* (Lower Keuper, ku). In addition, some information could be gained from geologists, with experience of the geology of South-Western Germany. In this way, the number of inspected *Stubensandstein* quarries increased, although most of these were either used for the extraction of sand or were abandoned and recultivated.

The inquiry revealed that the highly porous *Schilfsandstein* (Kraichgau) and the *Buntsandstein* (Black Forest) are inconsistent with the aims of the project due to their fracture systems. They are either dominated by very high fracture distances of up to 2 m or by widely gaping fractures. The criterion of a homogeneous and dense fracture system cannot be fulfilled for the field block. This also applies to the *Stubensandstein* layer which is extracted from the quarry near Pliezhausen and which is called 'Lower Bed'. The overlying

'Upper Bed', however, is characterized by quite a dense fracture system with fracture distances of an estimated 0.25 m to 0.5 m (Figs. 5.1 and 5.4). Later on, these values are confirmed by a statistical fracture-system analysis (Section 5.3.1).

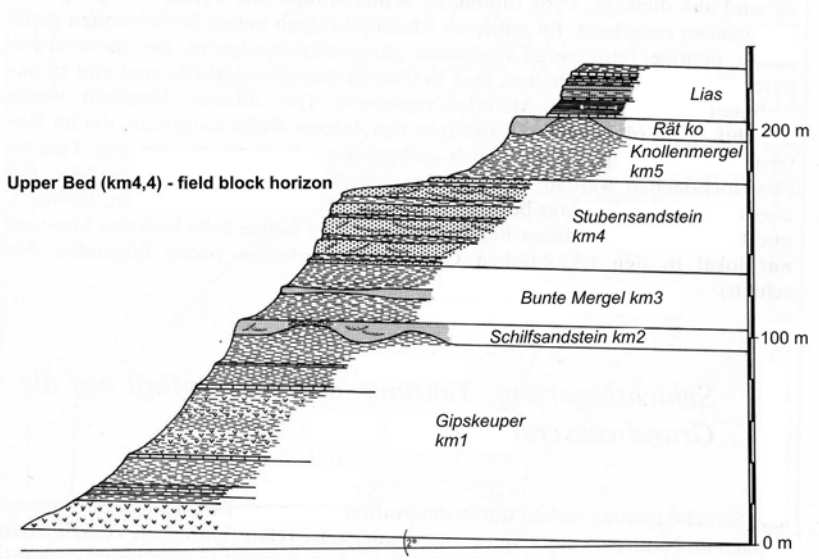

Fig. 5.1. Stratigraphic overview from Middle Keuper to Lower Lias (Einsele and Agster (1986), mod.).

The intensive inquiry into *Stubensandstein* quarries showed quarry *Fauser*, at Pliezhausen-Rübgarten near Reutlingen, to be the only *Stubensandstein* quarry in Baden-Württemberg which is still in use. At other quarries, the sandstone disintegrated during cutting, so that it was used for the extraction of sand (region of Löwensteiner Berge and Mainharder Wald) or limestone production (e.g. quarry *Bayer*, Kernen/Esslingen). Numerous other quarries had already been filled in the course of recultivation processes.

The *Stubensandstein* of the Upper Bed turned out to have more favorable rock characteristics (smaller mean fracture distance) and better rock-matrix properties (expected porosity of approximately 20 %) than the *Schilfsandstein* of the Kraichgau area. Thus, following an inspection of the potential areas, the quarry *Fauser* in Pliezhausen-Rübgarten (Fig. 5.2) was selected to be the location of the hard-rock test site.

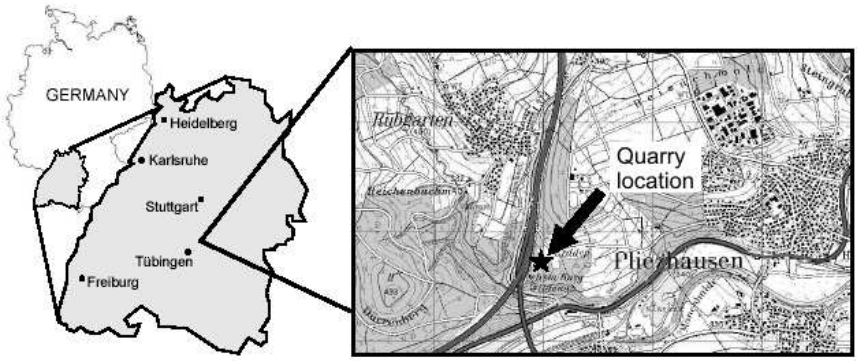

Fig. 5.2. Position of the test site near Pliezhausen/Baden-Württemberg.

5.1.2 Local Positioning

After quarry *Fauser* near Pliezhausen has been chosen as the best location for setting up the test site, the exact field-block boundaries had to be fixed. In this context, the following limiting aspects had to be kept in mind:

- limited thickness and lateral extension of the sandstone facies of the Upper Bed due to numerous quick lithofacial changes within the *Stubensandstein* horizon,
- limited amount of space for the test site due to the nearby slope of a neighboring landfill site, north of the quarry area,
- intended and approved enlargement of the quarry to the east with an access road from the south-east.

At quarry Fauser, there are outcrops of the 3^{rd} and the 4^{th} *Stubensandstein* (Lower Bed and Upper Bed with field-block horizon). Above these sandstone layers follows the silty *Knollenmergel* (km5) with a thickness of more than 3 m. Only the Upper Bed of the *Stubensandstein* features the high matrix porosity and small fracture distances, so that it was finally chosen as field-block horizon (Fig. 5.1).

During the search for a suitable test site within the quarry area, a spur next to a small biotope pond in the north-western part of the quarry was initially considered (Fig. 5.3). This spur presented an isolated sandstone block with only a rather thin coverage of loose material of 1.7 m to 2.9 m at that time. However, based on a facial analysis (Bengelsdorf, 1997), this area was identified as part of an older slip-off-slope sedimentation. Its petrographic characteristics are the same as those of the Lower Bed (3^{rd} *Stubensandstein*) with fracture distances of up to 2 m. Thus, it turned out to be unsuitable as a location for the test site.

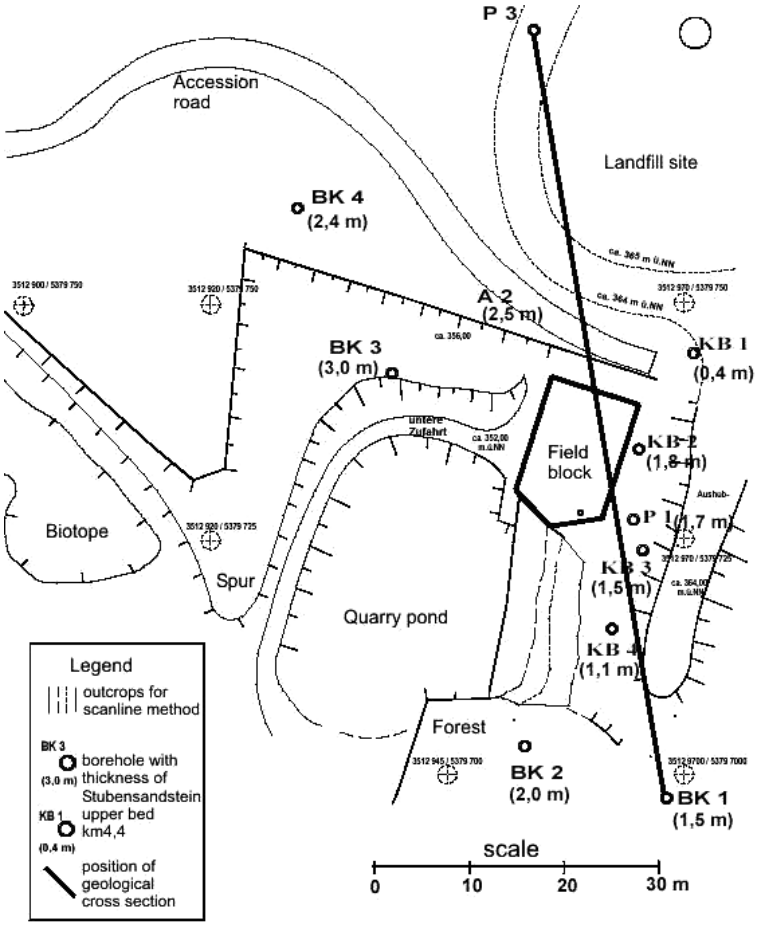

Fig. 5.3. Map of the quarry area with position of the test site when the project started in 1996 and position of geological cross-section (cf. Fig. 5.4).

While the exact test site boundaries were being established, information gained from former quarry-investigation boreholes could be used. Boreholes in the north-eastern part of the quarry indicated a thickness of the *4th Stubensandstein* of 2.2 m to 2.5 m. An analysis of the variations in thickness of the Upper Bed at the different boreholes and a correlation of these data with the current outcrops led to the assumption that the maximum thickness of this sandstone layer was in the north-eastern part of the quarry with an average of to 2 m to 3 m. This part of the quarry is bordered to the north by a landfill site for building rubble and ground excavation material (Fig. 5.3).

At the test site, the technique of ground-penetrating radar was applied in order to gain additional information on the sandstone thickness. However,

3 m-thick layers of silty and clayey *Knollenmergel* (km5) significantly reduced the penetration depth of the electromagnetic waves. As a result, it was not possible to determine the thickness of the sandstone layer on the basis of the measured reflectograms.

To investigate depth and thickness of the Upper Bed (km4,4 - sandstone horizon) in the north-eastern part of the quarry in more detail, four core drillings were set up at the projected field-block location. The drillings indicated a sandstone thickness of 1.8 m to 2.1 m, quickly decreasing further to the north-east (Fig. 5.4). In spite of a covering of more than 3 m of *Knollenmergel*, this area was finally selected as the best location for setting up the test site.

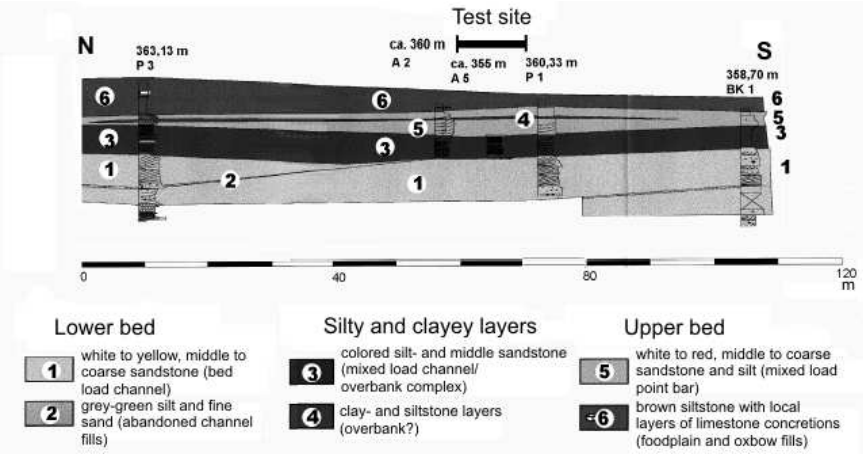

Fig. 5.4. Geological cross-section of the test-site quarry (Bengelsdorf (1997), mod.).

5.2 Preparing a Test Site on the Field-Block Scale

C. Thüringer, M. Weede, H. Hötzl

The preparation of the test site is very extensive and time-consuming and can be divided into two main phases. During the first phase, the rock formation is excavated and shaped for complete encapsulation during the second phase. This sealing is one fundamental requirement for setting up controlled experimental boundary conditions.

5.2.1 Excavating and Cutting

The field block was prepared in several steps. First, the raw field block was carefully excavated step by step during the expansion of the quarry area to the east. For this, excavators were used. At that time, digging in the lower sandstone bed in the south-eastern part of the quarry was scheduled as part of the expansion plan and this fixed the southern boundary of the field block. To the north, the field block is bordered by the foot of the neighboring landfill *Schindhau*. To the west, the raw shape of the field block was delimited by the old quarry digging line and, to the east, the decreasing thickness of the sandstone layer limited the size of the test site.

Finally, the raw field block was shaped like an irregular polygon, excavated on three sides (Fig. 5.5).

Fig. 5.5. Raw field block from the south (length of scale rod in the center of the figure: 2 m).

South of the designated test-site area, a step-by-step removal of the Upper Bed (km4,4) (Figs. 5.1 and 5.4) was carried out. In this way, three more or less parallel outcrop walls were generated. These three walls, approximately 2 m high and 15 m to 20 m long, were used together with one orthogonally ori-

ented wall for a statistical determination of the fracture-system parameters as described in Sec. 5.3.1. Figure 5.3 shows the position of these walls.

The raw, irregular field block was cut to its final shape of an axis-symmetrical oblong pentagon by using a diving saw. Alternative methods, such as a wire saw or a sword saw, had been tested in the run-up to the project and found to be impracticable. When the diving saw technique is applied, the contours of the later field block initially have to be redrawn by vertical boreholes (diameter of boreholes: 210 mm) at a distance of 60 cm to 80 cm to each other. Then the guide rail of a diving-saw system can be lowered into each borehole. The blade of the diving saw cuts into the sandstone from each hole to the right and to the left. By inserting the saw into the next hole, cutting down and repeating this procedure for every single borehole, the final shape of the field block is achieved. Figure 5.6 illustrates the hydraulically powered diving-saw system used at test site Pliezhausen.

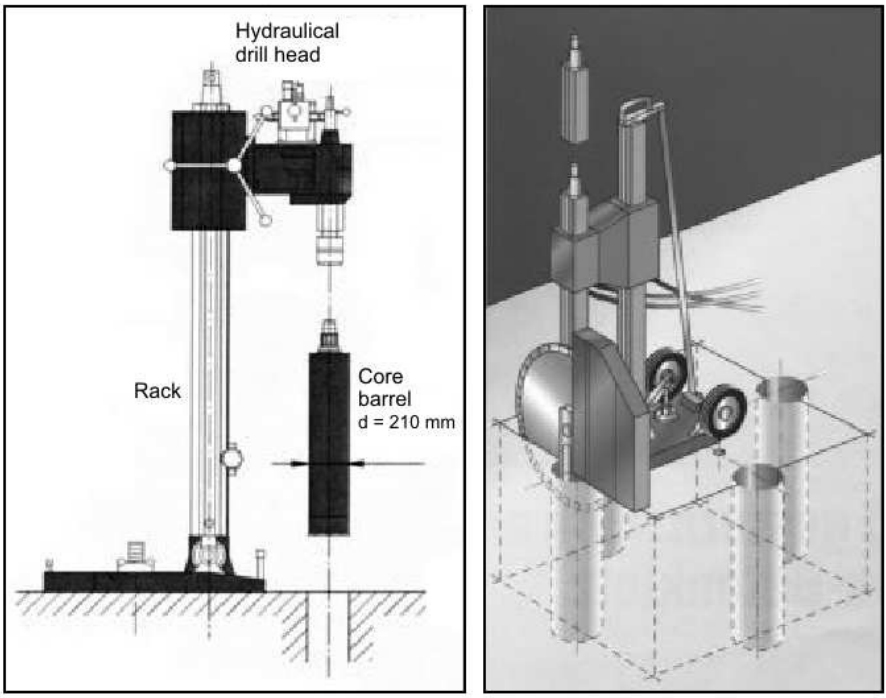

Fig. 5.6. Hydraulically driven diving-saw system used to shape the field block (Hilti Corporation, mod.).

In order to create field block side walls that are as plain as possible, a lateral overlapping of the cuts had to be achieved. To this end, the distance between two neighboring boreholes had to be chosen in accordance with the

saw blade diameter. With saw blades with a maximum diameter of 100 cm, the borehole distance was chosen to vary between 60 cm and 80 cm. The core-drilling technique was used in connection with a rinsing system, with water supplied by the small quarry pond.

The cuttings must follow the same cutting plane to avoid a blocking of the diving-saw system and material damage. When the saw is moved to the next borehole, the orientation of the saw blade must not be changed horizontally or vertically. To ensure this in spite of the rough and bumpy sandstone surface, the diving-saw system was mounted on a platform, which could be moved along two parallel rails. This construction was fixed on the sandstone surface using rock dowels, with the platform oriented horizontally. In this way, it was possible to shift the drilling and diving-saw systems a distance of approximately 3 m without lifting them. Afterwards, the whole rail construction was moved and fixed again.

Despite this significant improvement of the saw system, meeting a fracture at an acute angle turned out to be a problem. Sandstone fragments very often broke off the field block and wedged between saw blade and sandstone. This caused a slowdown of the cutting progress and sometimes even a blocking of the saw blade because its cutting plane shifted.

After the raw field block had been cut into a pentagon the cutting slots were widened by hydro-pressure cushions (Fig. 5.7). In this way, separated rock mass could be lifted off the field block. The sandstone was chopped up and spread around the test site by an excavator, creating a level and dry working area.

Fig. 5.7. Widening the cutting slots with hydro-pressure cushions (left) while shaping the field block (right); direction of view: south-east.

At this point, the field block was shaped. However, in order to create controlled flow fields under controlled boundary conditions inside the sandstone, the whole block had to be sealed.

5.2.2 Sealing Process and Installations

One of the main advantages of experiments on the laboratory scale is the possibility to control the boundary conditions completely when hydrogeological tests are carried out. Within the hard-rock aquifer-analogue project, this advantage is transferred to the field-block scale by sealing the whole natural aquifer cut-out.

As already described in Sec. 5.1.1, the *Stubensandstein* formation is characterized by a changing sequence of sandstone beds and silty to clayey layers. Several core drillings from the test-site location investigation phase show that also the field block bases on a clay layer of 3 to 4 m thickness. This clay is nearly impermeable, as revealed by laboratory tests. Thus, it may be regarded as a natural basal sealing of the field block. Consequently, in order to encapsulate the block, only the five side walls (approx. 85 m^2 altogether) and the surface (approx. 90 m^2) have to be covered artificially. In terms of the provided investigation program, the coating should be both water- and gas-proof. During the starting phase of the project, a two-component epoxy-resin system was used. Previous adhesion tests with fragments of the *Stubensandstein* had shown this to be the most suitable system. One fundamental prerequisite for the successful application of the epoxy resin is the complete dryness of the sandstone surface. Thus, the coating could only be applied during completely rainless days. This was done between July and September 1998 in four steps.

At first, loose rock material was removed and every surface of the field block was sand-blasted thoroughly. In a second step, the walls were primed with an epoxy primer in order to improve the adhesion of the resin. Afterwards, the main fracture traces and some points of disruption were filled with cement. Smaller fractures were closed by a grout of resin and silica sand. In the last step, the prepared surfaces of the field block were covered by at least two layers of two-component epoxy-resin coating. The mean thickness of this coating was approximately 5 mm.

Although the coating was applied with great care and despite the promising results already gained with resin coatings in the laboratory, this method proved in time to be completely unsuitable for field conditions. The great differences in temperature, which may be up to 50 °C at the test site Pliezhausen in the course of one year, induced stresses between resin and sandstone. Cracks appeared in the coating after two years and the sealing started to flake. The now unusable resin coating had to be ablated and removed in the following weeks.

The failure of the resin coating illustrates the enormous operational demands on the coating material over the years. Temperature changes may create significant stresses between materials of different coefficients of heat expansion. From then on, a multi-layer coating of special water- and gas-proof concrete with an expansion comparable to that of sandstone was used. The application of this coating can be divided into three main steps:

1. building a basal ring of concrete around the field block as a foundation for the casing walls;
2. erecting casing walls of limestone bricks, enclosing the field block and setting up a core wire frame as a reinforcement,
3. filling in the gap between wall and field block with concrete and sealing the block surface.

During the first construction phase, a 40 cm-thick ring of concrete is cast around the base of the field block. It has to perform two main tasks. On the one hand, it represents the foundation of the side walls of the encapsulation. Without this ring, the construction of the 2.20 m-high supporting walls would have been impossible on the soft and plastic clay layers. On the other hand, a drainage pipe is installed inside the concrete foundation in contact with the sandstone base. This pipe allows a continuous irrigation of the sandy to silty basement of the field block. This is to prevent these layers from drying out and leaking during gas-flow and gas-tracer experiments. When a suitable hydraulic head is connected to this inlet pipe, the whole sandstone block may be saturated from its basement step by step. In addition, drainage pipes are installed inside the concrete ring, through which the seepage water from the outcrop walls behind the field block can be discharged. Figure 5.8 shows the unsealed field block after construction phase 1 with the cast concrete ring as the foundation of the supporting walls. The white tarpaulin acts as a temporary provisional weathering protection during the construction.

What cannot be seen in this photo are lengths of reinforcing wire, which are fixed in the concrete foundation at a lateral distance to the field block

Fig. 5.8. Unsealed field block with concrete ring foundation; direction of view: northeast.

of approximately 20 cm. Reaching once around the whole field block and protruding 15 cm vertically from the concrete strip around it, they provide fixing points for a construction of reinforcing wire, installed in construction phase 2.

During this second phase, retaining walls of limestone brick (40 cm × 10 cm × 20 cm) are erected and the whole field block is enclosed in a cage of reinforcing steel wire. Steel mats (2.50 m × 5.00 m, diameter of wire: 5 mm) are placed and fixed onto the protruding wire strips installed during construction phase 1 so that they overlap (Fig. 5.9).

Fig. 5.9. Reinforcing wire at the north-western edge of the field block and overlapping steel mats, tied by twisted wires.

If the steel mats are higher than the field block, they are bent at right angles and fixed to the steel mats lying on the field-block surface. Reinforcing bar spacers ensure that the steel mats are not in direct contact with the sandstone. In this way, a completely closed cage of reinforcing wire is built, in order to compensate for tensile stresses caused by frost-thew-changes. It should be mentioned that all ground-penetrating radar techniques (Sec. 5.5.2) had been applied before the reinforcing wire was used. The rather close-meshed steel mats make any measurements based on the penetration of electromagnetic waves impossible.

Afterwards, a 2.50 m-high wall of limestone bricks is built, around the whole field block and the steel cage at a distance of approximately 30 to 40 cm (20 cm distance between steel and sandstone). The wall can be adapted by shaping the individual bricks and installations (see below) can be integrated.

During the third and final construction phase, the gap between the retaining walls and the sandstone block is filled with special concrete using a concrete pump. During this process, the wall has to be supported from the outside because of the immense pressure exerted by the concrete when the whole 2.50 m gap is filled up. Ideally, the gap is filled in two to three layers and the concrete should be mixed in such a way that it can flow, but will set quickly. Every concrete layer has to be consolidated accurately in order

to avoid significant inclusions of air between the reinforcement wire and the field-block side wall. The block surface should also be covered with concrete layer by layer. Applying this method avoids major inhomogeneities inside the encapsulation. In hot sunshine, the setting process of the concrete on the block surface should be delayed to avoid cracking as a result of over-rapid hardening. This can be done with a wet tarpaulin, for example.

In all, approximately 54 m^3 of special concrete were used to seal the test site. Figure 5.10 shows the completely sealed field block with the retaining walls and the block surface completely covered with concrete.

Fig. 5.10. Completely encapsulated field block; direction of view: south-east.

The completely sealed field block is accessible for hydrogeological experimentation by means of different installations. First, there are several boreholes, with which different investigations can be carried out. The boreholes are the results of core drilling with a diameter of 50 mm, carried out before the field block was sealed. Each borehole is between 1.80 and 2.20 m deep and thus reaches down through the sandstone layer into the underlying impermeable clay. It is necessary to distinguish between the marginal boreholes at the edges of the field block, made at an early stage of the project (Sec. 5.6.2), and the ring of boreholes in the central part of the test site (Sec. 5.6.3). Furthermore, measuring ports are fixed on both the side walls and the field-block surface, forming a regular grid with some additional ports on the traces of some of the main fractures (Fig. 5.11).

Each port consists of a PVC tube with a diameter of 40 mm at the block and 25 mm at the outer end. Without changing the natural aquifer properties, the tubes are fixed to the sandstone using a circular cut of 1 cm depth and

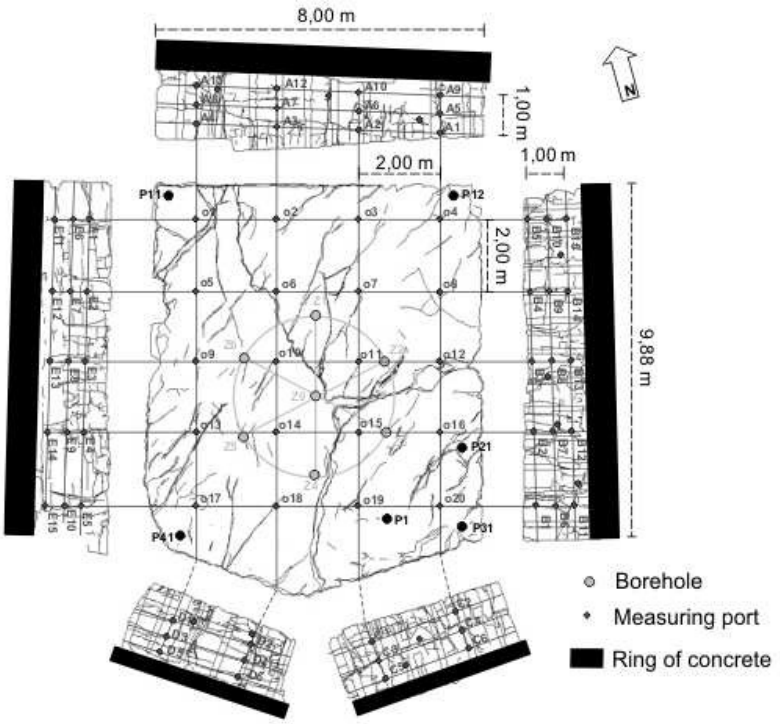

Fig. 5.11. Boreholes and measuring ports used at the field block.

caulking grout. By means of these tubes, the pressure distribution and tracer concentration can be logged, independently of the boreholes. The tubes have to be attached to the sandstone, fixed to the reinforcing steel and be inserted through holes in the retaining wall before the cement is poured. Figure 5.11 displays all the installations available for hydrogeological experimentation at the test site.

5.3 Characterization of the Rock-Matrix and Fracture-System

K. Witthüser, M. Weede, C. Thüringer, H. Hötzl

In order to assess the influence of the structural properties of the porous fractured aquifer on flow and solute transport processes, several structural parameters have to be estimated. Parameters of the fracture system and those of the hard rock matrix can be distinguished. In the following, the methods applied to the *Stubensandstein* field block and the associated evaluated parameters are described.

5.3.1 Statistical Evaluation of Fracture Parameters

In order to gain reliable and meaningful data on fracture allocation and orientation, as many fissures as possible have to be registered. The scanline method (Priest, 1993) is a feasible way of achieving this aim. In this method, the investigation is carried out at easily accessible outcrop walls, where a preferably representative part of the fracture system is visible. Depending on the fracture system, these walls should cross the fractured aquifer in several different orientations. In the case of the field block, three parallel outcrop walls and one orthogonally oriented wall can be analyzed (Fig. 5.3). First, the outcrop walls are covered with a grid of parallel marking lines. Then, every line is systematically scanned from one end to the other and analyzed for fractures which cross the line. For every single one of these fractures, parameters such as fracture orientation, fracture length (fracture-trace length at the outcrop wall), fracture spacing (distance between two neighboring fractures on the scanline), aperture and fracture characteristics (e.g. roughness, coating) are systematically registered.

With this method, about 300 fractures are recorded at the test site. After favored orientations among this large amount of fractures have been decided on, elements with an orientation within a certain limited deviation are assembled in clusters. Each cluster represents one main fracture orientation, to which properties such as aperture or fracture length can be statistically assigned. In this manner, a statistical model of the field block is obtained.

In addition to the scanline technique, another, less labor-intensive fracture registration method is used, namely stereophotogrammetric shooting. The method requires a stereometric camera and an analytical plotter. Initially, photographs are taken from all sides of the field block, using a stereometric camera. Fracture traces, visible in the stereo pictures, are then analyzed by an analytical plotter. At the test site, in all five walls undergo stereophotogrammetric fracture-orientation evaluation. Among these are two side walls of the raw field block and four exposed walls of the quarry, partly orthogonally oriented. The stereo pictures are analyzed by an analytical plotter at the Department of Photogrammetry and Remote Sensing at Karlsruhe University. Figure 5.12 shows a 3D view of the unsealed field block with all the fracture traces determined by the stereophotogrammetric shooting.

With the cosine-exponent-weighting method, the intersection points of the normal vectors of the fracture traces with the lower hemisphere are calculated. The result is visualized in a two-dimensional contour plot, as shown in Fig. 5.13. The main fracture-trace orientations are determined by identifying the peak discontinuity densities and choosing an acceptable angle of deviation for each cluster. The identified clusters are assumed to satisfy a Fisher distribution.

The measurement of fracture-trace lengths along an outcrop results in several sampling errors (Kulatilake *et al.* (1993), Pointe and Hudson (1985), Baecher *et al.* (1977)). These errors include the proportional length bias, the

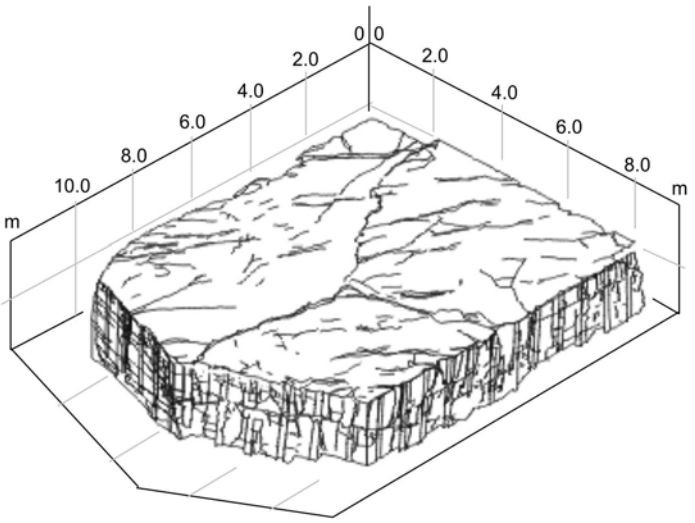

Fig. 5.12. 3D view of the field block, with stereophotogrammetrically registered fracture traces and boreholes; direction of view: north-west.

censoring bias and the truncation bias. While intensive field surveys have shown that the truncation bias is negligible for a short cut-off length, all other sampling errors can be treated and corrected mathematically. Since the trace lengths at the outcrop are assumed to follow an exponential distribution, the Erlang-2-distribution is fitted to the empirical scanline data for each cluster, always yielding high levels of statistical significance. The quality of this adaption can be tested by applying the Kolmogoroff-Smirnov test (Hartung, 1995).

The fracture spacings evaluated by the scanline technique are adapted by an exponential distribution, which can be derived for a random allocation of fracture elements (Priest and Hudson, 1976). For a further examination of a possible areal correlation, fracture-density variograms (Chilès and de Marsily, 1993) are calculated. The mean three-dimensional fracture density, i.e. the mean fracture plain [m^2] per rock mass volume [m^3] is calculated according to Chilès and de Marsily (1993).

Altogether, 947 fracture elements are measured at the test site, 300 by the scanline method and 647 by the stereophotogrammetric method. Fig. 5.13 shows the cluster orientation of all registered fractures. The associated statistical parameters are listed in Tab. 5.2. In the diagram, three main directions can be identified. There are two nearly vertical fracture orientations (clusters II and III), striking 56°and 139°, and one almost horizontal bedding plane (cluster I).

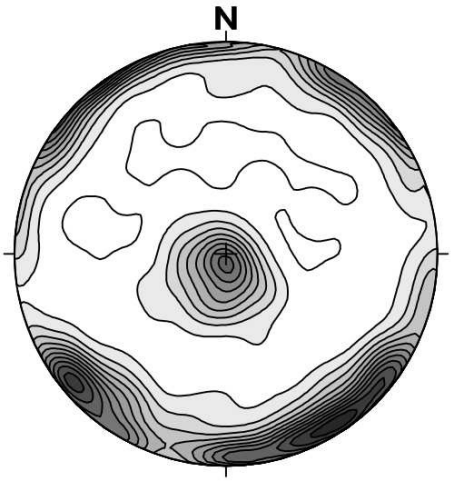

Fig. 5.13. Fracture-orientation-distribution diagram of Pliezhausen test site.

Table 5.2. Statistical parameters of the three main clusters.

Cluster	Dip Direction	Dip	Spherical Aperture
I	201°	85°	11.22°
II	146°	7°	12.05°
III	229°	8°	10.20°

Looking at the fracture-orientation-distribution diagram while distinguishing between scanline- respectively shooting-direction, the blind zones (Terzaghi, 1965) of the particular measurements can be clarified. Evaluating the orientation of the bedding plane is not possible by this means because it is parallel to the horizontal stereophotogrammetric shots. Thus, a correction of the geometric error is not practicable. Only by evaluating the data in three directions in space using the scanline technique or the stereophotogrammetric method does a realistic statistical description of fracture orientation become possible.

The empirical fracture-distance distribution, measured by the scanline method, can be adapted by an exponential distribution very well. The maximum deviation between the two distribution functions is only 0.0446. The mean fracture distance according to all scanline measurements is 0.231 m. The semivariograms of fracture density do not indicate a spatial correlation between the fracture intersections and the scanlines (Fig. 5.15).

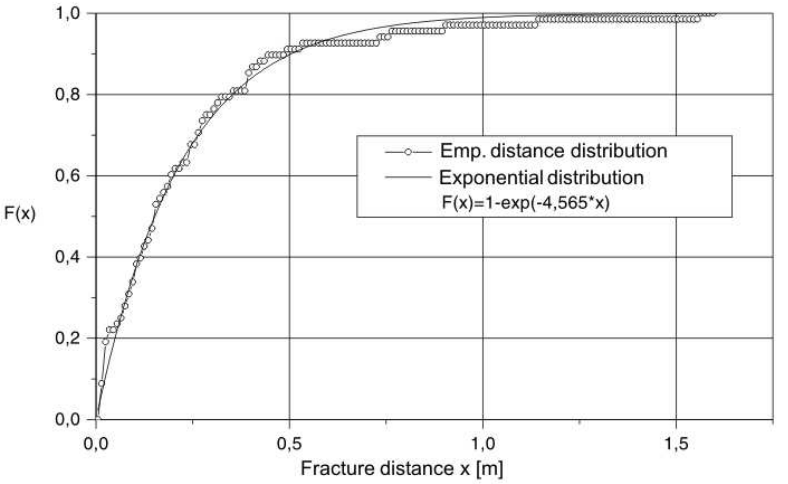

Fig. 5.14. Fracture-distance distribution at the test site (scanline technique).

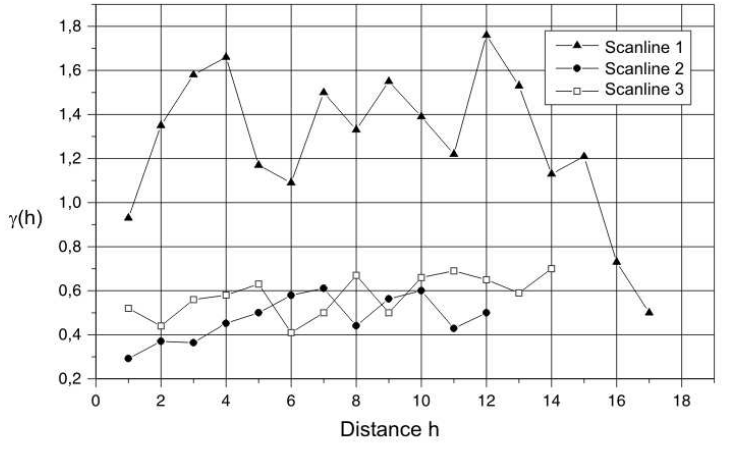

Fig. 5.15. Semivariograms of fracture density according to different scanlines.

A random fracture distribution in space is confirmed by a highly significant adaption of the expected exponential distribution for random fractures and the random variograms of fracture density. The mean fracture density is $11.337\,\mathrm{m}^2/\mathrm{m}^3$.

Fitting the horizontal and vertical fracture-trace lengths to Erlang-2-distributions shows high statistical significance. Figure 5.16 additionally describes the exponential distributions of the whole outcrop, corrected with regard to the proportional length bias.

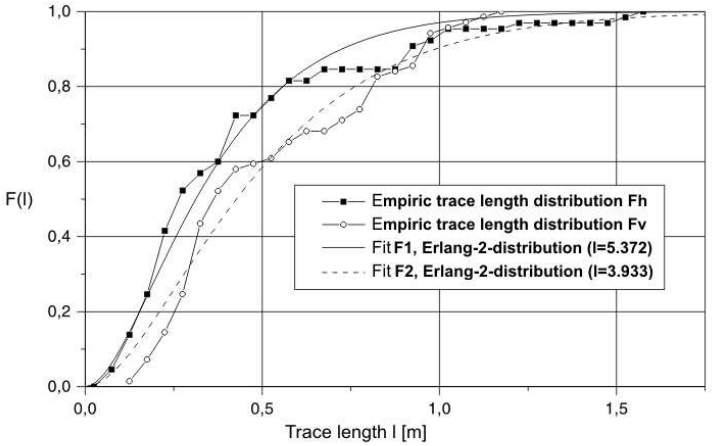

Fig. 5.16. Fracture trace lengths of the scanline measurements.

Describing the fracture-trace lengths according to cluster affiliation does not yield any significant difference in the distribution parameters. Fractures preferentially end at sedimentary boundaries, so that a common distribution function for two almost vertical fracture clusters and the horizontal bedding can be assumed.

For both the side walls and the surface of the field block, visible fracture traces have been recorded (Fig. 5.17). A 3D illustration of the test block can be created with the available information (Fig. 5.12).

5.3.2 Determination of Rock-Matrix Properties

Not only the fracture system, but also the properties of the hard-rock matrix have great influence on flow and transport processes. Thus, hydraulic and physical parameters such as density, porosity or permeability are determined in accompanying laboratory tests. Besides, X-ray diffractometry is an effective tool for estimating the retarding influence of fracture coatings and fracture fillings.

Fig. 5.17. Fracture traces on photo and digital plot (east face of the block).

5.3.2.1 Mercury Porosimetry

Mercury porosimetry is a popular method for determining the porosity of any solid material. Apart from the total porosity, the mean pore diameter and the pore-diameter distribution can also be evaluated. The mode of operation is based on the high surface tension (0.480 N/m) and the large contact angle of mercury. According to Washburn (1941), mercury, as a non-wetting liquid, only intrudes into pores if pushed by an external force. If the pores are pictured as a bunch of capillaries, the pressure which is necessary to push the mercury into a pore is inversely proportional to the pore diameter. This dependence is described by the WASHBURN equation:

$$d = -\frac{4\gamma \cdot \cos\theta_C}{p} \tag{5.1}$$

During the measuring process, the sample is surrounded by a gravimetrically determined volume of mercury. Then the whole sample chamber is pressurized step by step. With continuously increasing pressure, the volume of the mercury which is forced to intrude into the sample pores is recorded at every pressure step. According to the WASHBURN equation, every pressure can be associated with a certain diameter of the pores which get filled. Thus, it is possible to make a statement on porosity and pore-diameter distribution by measuring the volume of intruded mercury (Fig. 5.18).

The porosity of the sandstone matrix is determined, using mercury porosimetry on samples from different parts of the field block. The results range from about 19 % in the upper part of the block up to 23 % near the finely grained basement. In this context, it should be noticed that these results are not necessarily representative of the effective porosity, the volume accessible for groundwater movement. According to Busch *et al.* (1993), a flow of water due to gravity cannot take place through pore channels smaller than 0.008 mm (Fig. 5.18). Hydrostatic forces make all water inside these channels adhere to the walls, so that any flow is averted. The distribution of the

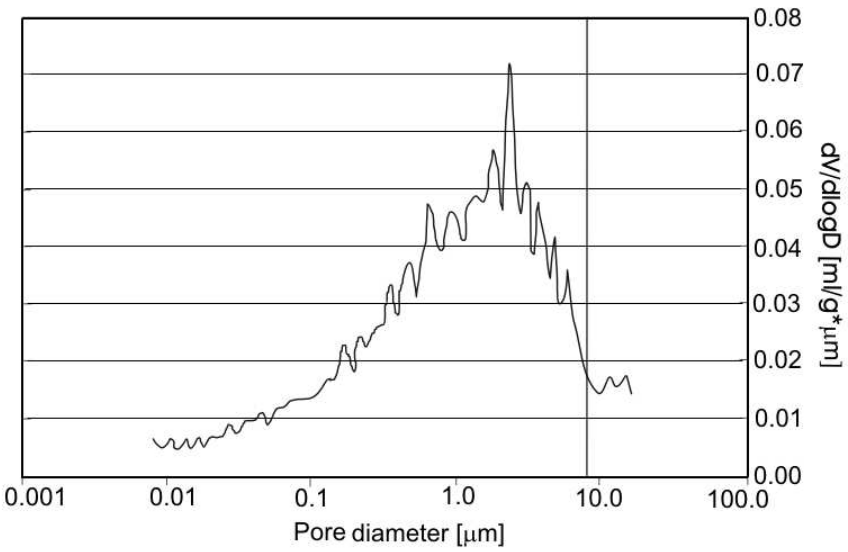

Fig. 5.18. Pore diameter distribution of Stubensandstein sampled at test site Pliezhausen, evaluated by mercury porosimetry; total porosity of this sample: 21.2 %.

sandstone pore diameters shows that the pore diameters in the field-block matrix are mostly between 0.001 and 0.005 mm (Fig. 5.18). These pores may not be added to the effective porosity. Besides, there are a certain number of dead-end pores which are not available for groundwater flow.

In summary, it should be noticed that the measured rock-matrix porosity can be seen as a guiding value. Even if these results are feasible for the assessment of diffusive transport processes between fracture and matrix on the one hand, they must on the other hand not be equated blindly with the hydraulically effective porosity of the rock matrix.

5.3.2.2 Permeability

In order to estimate the influence and the role of the rock matrix during flow and transport processes in fractured aquifers, the permeability of a compact, unfractured sandstone core sample should be evaluated in the laboratory by DARCY experiments. This approach simplifies the rock matrix to a homogeneous medium. The influence of dead-end pores, caused by the cementation of the hard rock is, together with the grain size distribution of the rock, the most significantly limiting factor for the hydraulic permeability.

The method is applied to completely saturated cylinder samples ($\varnothing$ = 10 cm) installed in pressure chambers. It is very time-consuming to achieve as complete a saturation of the cylinder samples as possible. The best results are

obtained rather quickly, by at first drying the samples in a drying chamber, until a constant weight is reached. Then, only the base plane of the cylindrical sample is irrigated with the aid of filter plates. Thus, water is pulled into the samples from the bottom by capillary forces, displacing trapped air upwards. When the water content inside the samples is stable, the water level is raised slightly and a new balanced water content is awaited. During the entire saturation process, the increasing water content of the sample should be monitored gravimetrically. In this way, the sandstone samples of 5 cm and 10 cm length can be saturated to approximately 90 %, during a period of only 3 to 4 days.

When a satisfactory saturation is reached, a constant hydraulic gradient is created, which causes a constant flow through the samples (Fig. 5.19). On the assumption of a homogeneous porous matrix throughout the sample, the hydraulic conductivity can be determined on the basis of the DARCY'S law by measuring the flow rate depending on the hydraulic gradient and the sample dimensions.

Fig. 5.19. Experimental set-up of the DARCY experiment, applied to samples of the field-block rock matrix.

The results of applying this experiment to core samples of the *Pliezhausen* test site were hydraulic conductivities varying from about $1.0{\cdot}10^{-7}\,\mathrm{m/s}$ to $1.0 \cdot 10^{-9}\,\mathrm{m/s}$. Table 5.3 exemplifies the measured pressure gradients, flow rates and sample dimensions.

Table 5.3. Results of the DARCY experiment, applied to cylindrical samples of *Stubensandstein* (d = diameter, l = length).

Sample dimension	Cross-sectional area [m^2]	Flow distance [m]	Hydraulic gradient [-]	Flow rate [m^3/s]	Permeability coefficient [m/s]
cylinder d = 9.8 cm l = 10.3 cm	$7.54 \cdot 10^{-3}$	0.103	13.235	$4.98 \cdot 10^{-10}$	$4.9 \cdot 10^{-9}$
cylinder d = 9.8 cm l = 10.1 cm	$7.54 \cdot 10^{-3}$	0.101	14.265	$6.99 \cdot 10^{-9}$	$6.5 \cdot 10^{-8}$
cylinder d = 9.8 cm l = 5.2 cm	$7.54 \cdot 10^{-3}$	0.052	18.854	$6.00 \cdot 10^{-9}$	$4.22 \cdot 10^{-8}$
cylinder d = 9.8 cm l = 5.1 cm	$7.54 \cdot 10^{-3}$	0.051	19.608	$3.15 \cdot 10^{-8}$	$2.13 \cdot 10^{-7}$

5.3.2.3 X-Ray Diffractometry

Fracture coatings and fillings may have great influence on the retardation potential of a fractured aquifer. To prepare the clay analysis, samples taken at the field test block are dried at 60 °C and milled in an agate mill. The qualitative mineral inventory was determined by X-ray diffractometry, using the JCPDS files of the International Center of Diffraction Data (ICDD, 1980). This method is based on the diffraction of monochromatic X-rays hitting the sample at the crystal grid layers. With the BRAGG equation, the grid-layer distance can be designated by means of the angle of maximum diffraction. These different layer distances of the crystal grid are characteristic for each mineral.

By comparison with the JCPDS files (ICDD, 1980), the mineral spectrum can be analyzed and identified. X-ray diffractometrical investigations of powder samples (particle size < 125 mm) at an angle range between 0° and 63° provides a review of the mineral inventory. A further identification of clay minerals occurs with air-dried texture compounds, so-called LuBOs. 1 g of the powder sample (grain size < 125 mm) is charged with 100 ml of distilled water, sodium pyrophosphate is added and this is then dispersed in an ultrasonic bath for 10 min. After separation of the clay fraction by centrifugation, the residual sample suspension is pipetted onto microscope slides. During the slow drying procedure, the clay mineral layers adjust in a horizontal position and thus increase the base reflections significantly. Further investigations occur in connection with the following usual clay-mineralogical procedures (Jasmund and Lagaly (1993), Wilson (1987)). To identify swellable clay minerals, the texture samples are vaporized with ethylene glycol in the

drying chamber at 60 °C for 96 hours after the first test series. The glycol saturation displaces the base reflections of swellable clay minerals so they can be distinguished from non-swellable species.

In order to differentiate between kaolinite and chlorite, the texture samples are cauterized in a muffle furnace at 550 °C and then reinvestigated with X-ray diffractometry. During the cauterization of the kaoline, the grid is destroyed completely while a diffraction peak caused by chlorite persists. The measurements are carried out with a SIEMENS D 500 X-ray-diffractometer with copper-potassium-tube.

To interpret the texture sample diffractograms, the benchmarks of Thorez (1975) and Thorez (1976) are used. The fraction of swellable clay minerals is determined by methylene blue adsorption (Hofmann *et al.*, 1976). In this method, the fraction of swellable clay minerals can be evaluated by the absorption of methylene blue, using a calibration value (Wyoming bentonite with 84 % by weight smectite).

The fracture fillings taken from a side wall at the raw test site and from borehole SB 46 at about 1.0 m depth are compared. X-ray diffractograms of both powder samples show a significant content of swellable clay minerals at an angle range from about 1° to 9°. These minerals are characterized by a grid-layer distance of 10 Å to 18 Å (illites, chlorites, smectites, vermiculites). The fraction of swellable clay minerals is about 30 % to 40 %, determined by the consumption of methylene.

The fraction of kaolinite in the side wall sample is estimated to be lower than 5 % on the basis of its peak face at 12.4°. By the cauterization of the normal LuBO sample, the 124°peak (basal distance 7 Å) disappeared completely. Thus, a content of chlorite in this sample can be ruled out. Halloysite is also apparently not present as a corresponding peak in the powder-sample diffractogram could not be found at 8.8°.

Small quantities of quartz could be verified at 20.9° (basal distance 4.26 Å) and 26.7° (3.34 Å). The fraction of kaolinite and feldspar is assumed to be lower than 5 % each, that of quartz should be lower than 10 %. The loss by combustion reaches about 4 %. The calcium carbonate content is very low (0.7 %).

Illite with its diffraction angle of 8.8°(basal distance 10 Å) can be verified in higher concentrations in the LuBO samples. It shows a second peak at 17.7°(5 Å) together with small amounts of muscovite at 19.95°(4.47 Å).

The fracture material taken from borehole SB 46 shows a higher fraction of quartz of about 30 % (Fig. 5.21) than the side wall sample (Fig. 5.20), which is caused by the higher content of sand in this material. This sample contains mainly illite and mixed-layer clay minerals.

The powder sample peak measured at 8.8° (basal distance 10 Å) is not only caused by illite but also by hydrated halloysite. This is confirmed by the 12.4°peak of the normal, air-dried sample, which cannot be caused by kaolinite because of the missing 7 Å-signal of the powder sample. In fact, this identifies the dehydrated halloysite, whose basal distance is reduced from

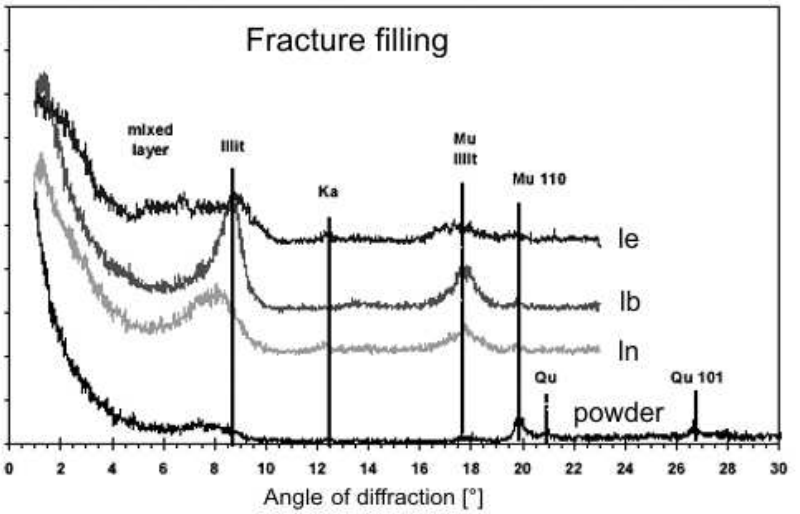

Fig. 5.20. X-ray diffractogram of a fracture coating at the field block side wall (le = LuBO ethylene glycol vaporized, lb = LuBO cauterized, ln = normal LuBO).

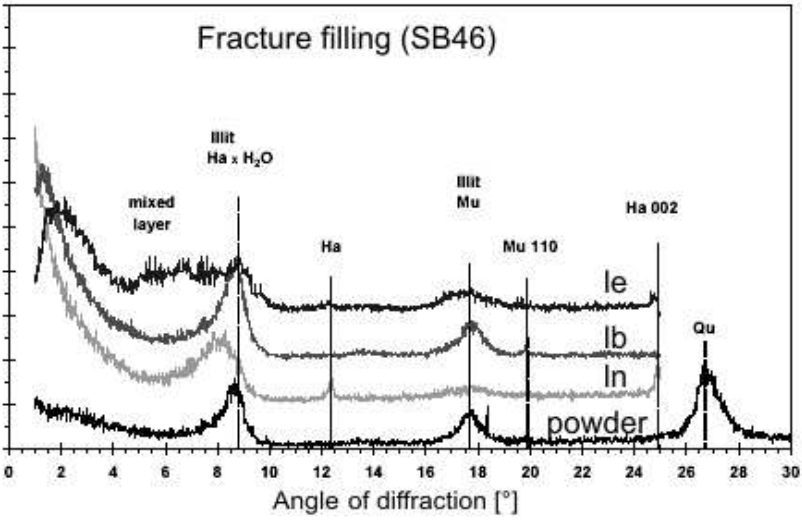

Fig. 5.21. X-ray diffractogram of fracture coating inside investigation borehole SB 46 (le = LuBO ethylene glycol vaporized, lb = LuBO cauterized, ln = normal LuBO).

10 Å (diffraction at 8.8°) to 7 Å (diffraction at 12.4°) by the loss of water during the drying process (Schachtschabel *et al.*, 1992).

The appearance of montmorillonite is indicated by a diffuse increase of concentration at about 5° within the ethylene glycol vaporized samples of fracture fillings. The absence of one well-defined single peak shows that there is presumably no pure montmorillonite but a mix of different smectites and mixed-layer minerals. The diffractograms suggest that the swellable clay minerals make up about 15 %.

5.4 Geostatistical Analysis of the Fracture Lengths and Fracture Distances

A. Silberhorn-Hemminger, Y. Rubin, R. Helmig

In Sect. 5.3.1, the results of a univariate evaluation of fracture-trace parameters such as orientation, length, aperture, distance, and fracture density are presented. Here, a geostatistical analysis, which includes the spatial distribution of the investigated parameters, is conducted. This leads to an improved understanding of the spatial variability of discontinuities in fractured media. In a detailed geostatistical analysis of the fracture density and the fracture orientation, La Pointe and Hudson (1985) show that fractured media can follow a systematic spatial pattern. Further geostatistical investigations in fractured media are done by Lunn and Mackay (1996). They analyze the vertical and horizontal correlation structure of the permeability of core sample data in fractured media. Desbarats and Bachu (1994) investigate the heterogeneity of the hydraulic conductivity of a sandstone aquifer using a geostatistical approach. The investigation considers the core scale up to the regional scale.

In the following sections, the spatial variability of the fractured media is analyzed by considering fracture-trace lengths and fracture distances. The fractures are recorded on a fracture-trace map of the surface of the field block shown in Fig. 5.22. First, the analysis concept of the spatial variability of the fractures using a modified scanline method is introduced in Sect. 5.4.1. The geostatistical analysis of the side walls is presented in Sect. 5.4.2. Finally, the results of the analysis are discussed in Sect. 5.4.3.

5.4.1 Strategy

The field block is characterized by high matrix porosity and is densely fractured. Three main fracture clusters are identified. Figure 5.22 clearly shows these three clusters on the side walls and on the top of the block: a strong horizontally oriented and two strong vertically oriented clusters. The data of the fracture clusters can be seen in Table 5.2. A detailed presentation of the field block including the geological characterization and the description of the material and hydraulical properties can be found in Sect. 5.3.

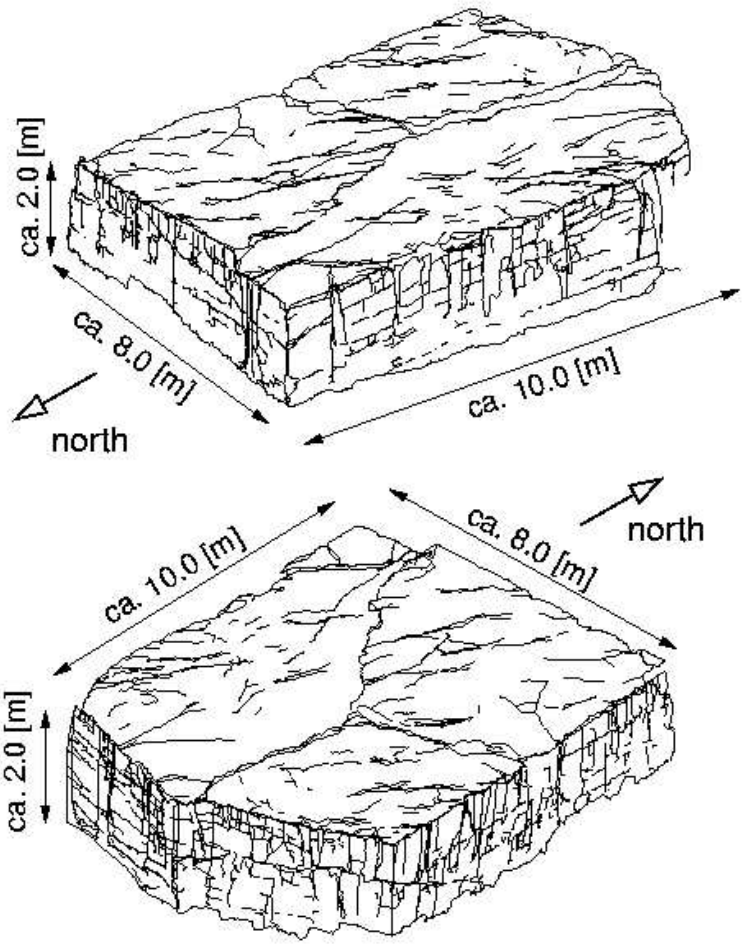

Fig. 5.22. View of the field block from the north-west and the south-east.

The spatial analysis of the fracture system is conducted using a modified scanline method. A set of parallel scanlines is distributed over the investigation domain. The scanlines themselves are divided into segments of equal length l. The scanlines are arranged perpendicular to one main fracture cluster. Furthermore, only fractures which are almost perpendicular to the scanlines are investigated with respect to intersection points with the scanlines. This allows a separate variogram investigation for each fracture cluster. Along the single scanline segment, the number of intersection points between fracture traces and the scanline segment itself is recorded.

In order to investigate the spatial variability of fractures (fracture arrangement and extension), the fracture frequency $FF(x_i)$ and the indicator variable $I(x_i)$ are analyzed. Here, the fracture frequency is indicated as the number of intersection points *(fracture - scanline segment)* which is recorded along the scanline segment with center x_i. The indicator variable $I(x_i)$ represents the existence or non-existence of one or more intersection points *fracture - scanline segment* which are recorded along the scanline segment with center x_i

$$I(x_i) = \begin{cases} 1 & \text{intersection "fracture - scanline" exists} \\ 0 & \text{no intersection "fracture - scanline" exists.} \end{cases} \tag{5.2}$$

The property of *fracture* is not continuously present in space. When a certain point in space is observed, a fracture either exists or not. Therefore, the indicator variable seems to be the right choice in order to investigate the spatial variability of fractures in space. Additionally, observations of the field block show that single fractures often do not appear as a single trace. They appear as two traces laying very close together. The fracture maps in Figs. 5.23 and 5.24 of the south-east, south-west and west wall show this very clearly. The advantage of the indicator variable is that two fracture traces which actually represent one single fracture are interpreted as one single fracture. However, the investigation of the variable fracture frequency interprets the two traces as two single fractures. The disadvantage of the indicator variable becomes clear when larger scanline segments are used. The indicator variable means a loss of information: two or more real fracture traces cannot be interpreted correctly, because the indicator variable just records the existence or non-existence of intersection points, but not the number of intersection points. Therefore, the investigation of the variable fracture frequency is preferable for larger scanline segments.

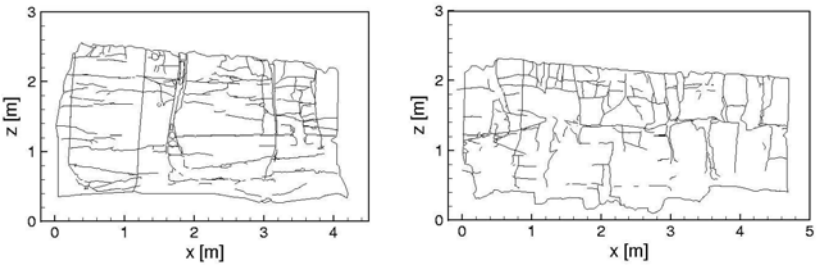

Fig. 5.23. Fracture map of the south-west and the south-east wall.

Within this study, different lengths l of scanline segments are investigated ($l = 0.04$ m, 0.10 m, 0.20 m, 0.30 m). With smaller scanline segments, the natural fracture structure and the small-scale behavior can be recorded in detail. The use of larger scanline segments leads to a higher smearing of the small-scale behavior and to the indication of spatial patterns which can be found

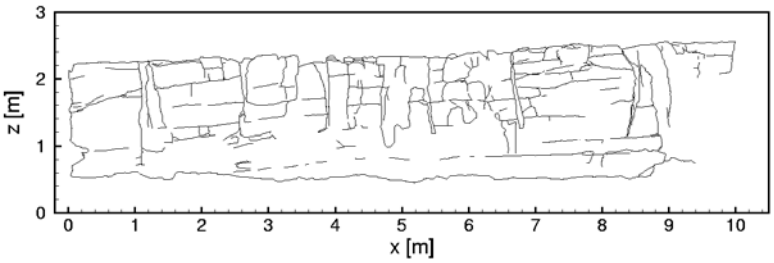

Fig. 5.24. Fracture map of the west wall.

on larger scales. The connection between fracture system, set of parallel scanlines, scanline segments, fracture frequency, and indicator variable is shown in Fig. 5.25.

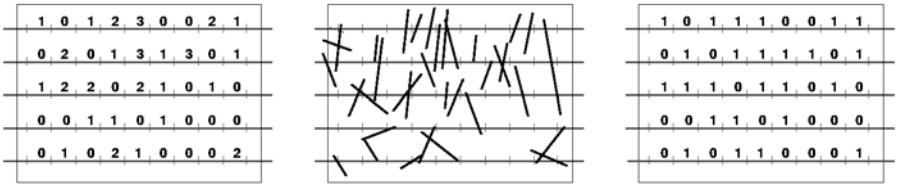

Fig. 5.25. Recording the fracture frequency and the indicator variable using the scanline method. Left: Fracture frequency $FF(x_i)$. Middle: Fracture system. Right: Indicator variable $I(x_i)$.

In the next step, the spatial variability of recorded fields is investigated. For this purpose, the experimental variogram of the fracture frequency

$$\gamma_{\mathrm{FF}}(h_i) \;=\; \frac{1}{2}\,\frac{1}{n(|h_i|)}\,\sum_{\alpha=0}^{n}\,[FF(x_{i_\alpha}+h_i)\;-\;FF(x_{i_\alpha})]^2 \tag{5.3}$$

and the experimental variogram of the indicator variable

$$\gamma_{\mathrm{I}}(h_i) \;=\; \frac{1}{2}\,\frac{1}{n(|h_i|)}\,\sum_{\alpha=0}^{n}\,[I(x_{i_\alpha}+h_i)\;-\;I(x_{i_\alpha})]^2 \tag{5.4}$$

are determined. Here, h_i is the separation vector, n is the number of pairs of distance $|h_i|$, and α is the index of the sample number.

The experimental variograms are determined in the directions parallel and perpendicular to the scanlines. The variograms are calculated using *GSLIB – Geostatistical Software Library* (Deutsch and Journel, 1992).

5.4.2 Geostatistical Analysis of the Side Walls

The fracture traces which can be detected on the side walls and the top of the field block are analyzed as described in Sect. 5.4.1. The fracture-trace map of the five side walls (north, east, south-east, south-west and west), which have uneven surfaces, is taken in three-dimensional spaces and then it is projrcted into two-dimensional planes. The error between the real and the projected surface is negligible.

The analysis of the spatial variability of the indicator variable and the fracture frequency is done by a variation of the parameters shown in Table 5.4.

Table 5.4. Experimental variogram investigation: variation of the parameter.

Aim of investigation	Scanline direction	Distance d between scanlines	Length l of scanline segments	Direction of separation vector h_i
Vertical fractures	Horizontal	0.10 m	0.04, 0.10, 0.20 m	h_i = (x,0), $\parallel$ to scanlines h_i = (0,z), $\perp$ to scanlines
Horizontal fractures	Vertical	0.20 m	0.04, 0.10, 0.20 m	h_i = (0,z), $\parallel$ to scanlines h_i = (x,0), $\perp$ to scanlines

The detailed analysis of the variogram investigation is shown later for the segment length $l = 0.10$ m. The results of the variogram investigation for the segment lengths $l = 0.04$ m, 0.10 m, 0.20 m are discussed in Sect. 5.4.3.

5.4.2.1 Horizontal Scanlines: Segment Length $l = 0.10$ m

The indicator and fracture-frequency fields of the south-west and the west walls can be seen in Figs. 5.26 and 5.27. The black cells of the indicator field represent the indicator value $I(x_i) = 0$ and the white cells represent the indicator value $I(x_i) = 1$. Comparing the variable fields of the south-west and the west wall with the real fracture traces of the two walls (Fig. 5.23, left, and Fig. 5.24) shows the basic structure of the fracture traces within the variable fields. A similar result is obtained using a scanline-segment length of $l = 0.04$ m (not shown here); however, for the shorter segment length, smaller scale variations are captured.

The indicator fields no longer show the small scale information. On the one hand, the fields only show the *no existence / existence* of one or more intersection points along a scanline segment in accordance with equation (5.2). On the other hand, the fracture-frequency fields represent the small scale differences indirectly by a higher fracture-frequency value. The fracture-frequency field of the south-west wall shows this clearly. The number of segments with

a fracture frequency of $FF(x_i) \geq 2$ is quite high compared to the total amount of segments with a frequency of $FF(x_i) > 0$. One can even find segments with a frequency of $FF(x_i) = 5$. The fracture-frequency field of the west wall includes a high number of segments with a fracture frequency $FF(x_i) = 1$ and $FF(x_i) = 2$. The number of segments with a frequency $FF(x_i) > 2$ is relatively small compared with the total number of segments with a frequency of $FF(x_i) > 0$. The number of segments without intersection points (fracture frequency $FF(x_i) = 0$) is equal for both types of variable field. The trend of smearing the smaller scale differences with larger segment length becomes more obvious for the variable fields of segment length $l = 0.20\,\text{m}$.

Figures 5.28 and 5.29 show the experimental variograms of the indicator variable and the fracture frequency. Some of the variograms of the investigation with vector h_i=(x,0) parallel to the scanlines (Fig. 5.28) show a slightly oscillating and periodic behavior. In order to infer a periodic behavior from the variogram, the shape of the graph should be more distinct. Hence, the behavior represented by the variograms is interpreted as a nugget-effect behavior. This means that the appearance of one or more fractures and their spatial location perpendicular to their extension (fracture trace, fracture plane) is independent of the neighboring fractures. There is no correlation. The appearance of the fractures is based on a random process.

Figure 5.29 shows the experimental variograms with vector h_i=(0,z) perpendicular to the scanlines. The variograms focus on the spatial fracture extension, the length of the fracture traces. The graphs of the two investigation variables show very similar characteristics. The curves increase strongly for small separation distances $|h_i|$. For larger separation distances $|h_i|$, the rate of increase is reduced until it reaches a horizontal plateau for a separation distance of about $|h_i| = 0.70\,\text{m}$. The variograms show a correlated behavior approximately up to the distance $|h_i| = 0.70\,\text{m}$. Within this range, the spatial extension of the fractures is based on a correlated process. This means that, within this range, there is a spatial dependency of the fracture extension (fracture length) between the neighboring points in the direction of the fracture trace. The feature *no existence/existence of one or more fractures* at point x_i depends on the features of the neighboring points which are located within a distance smaller than the range $|h_i| = 0.70\,\text{m}$ in the direction of vector h_i. The features of the points which are located at a distance greater than the range $|h_i| = 0.70\,\text{m}$ have no influence of the feature at point x_i.

The similarity between the indicator and the fracture-frequency fields can be observed in the variograms as well. A comparsion of the average indicator variogram with the average fracture-frequency variogram (e.g. Fig. 5.29) shows very similar characteristics. However, the $\gamma_{\text{FF}}(|h_i|)$ values of the fracture-frequency variogram are higher than the $\gamma_{\text{I}}(|h_i|)$ values of the indicator variogram. This behavior can be observed in all graphs. The use of larger scanline-segment lengths (e.g. $l = 0.10\,\text{m}$) even increases this difference. This behavior is explained by the variogram equations. On the basis of

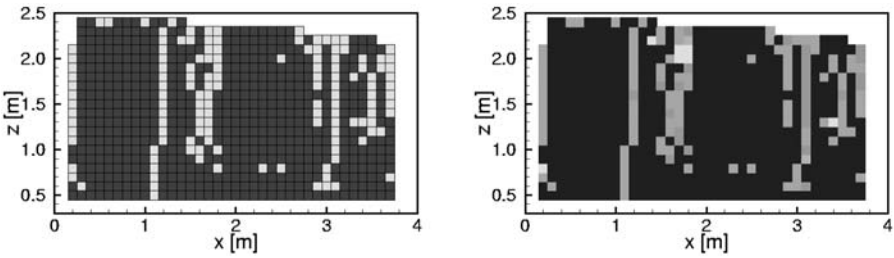

Fig. 5.26. South-west wall: indicator field and fracture-frequency field, scanlines in x-direction, segment length $l = 0.10\,\text{m}$, distance between the scanlines $d = 0.10\,\text{m}$.

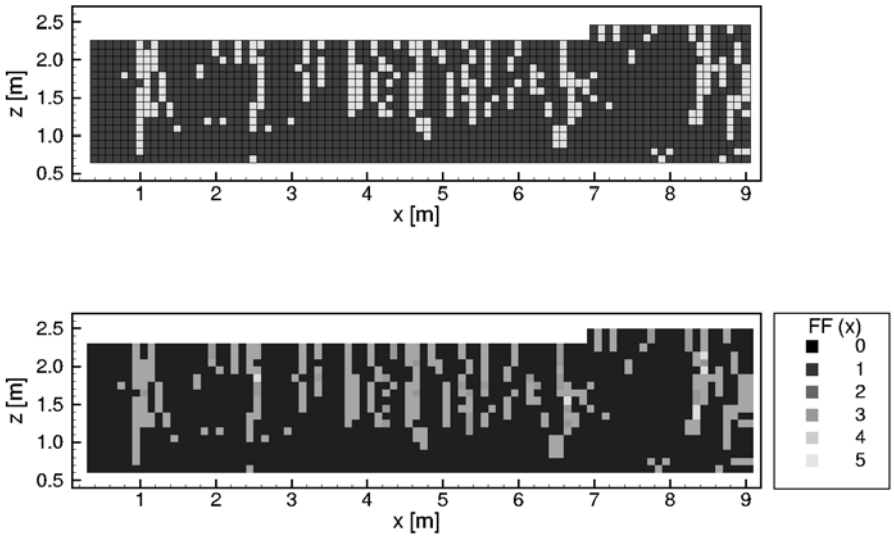

Fig. 5.27. West wall: indicator field and fracture-frequency field, scanlines in x-direction, segment length $l = 0.10\,\text{m}$, distance between the scanlines $d = 0.10\,\text{m}$.

the variable fields, the indicator variogram is calculated using equation (5.4) and the fracture-frequency field is calculated using equation (5.3)

The increment $[I(x_{i_\alpha} + h_i) - I(x_{i_\alpha})]$ of the indicator variogram is exclusively 0 or 1. In contrast, the increment $[FF(x_{i_\alpha} + h_i) - FF(x_{i_\alpha})]$ of the fracture-frequency variogram can have values higher than 1. The total number of point pairs n and the number of the point pairs with increment 0 are

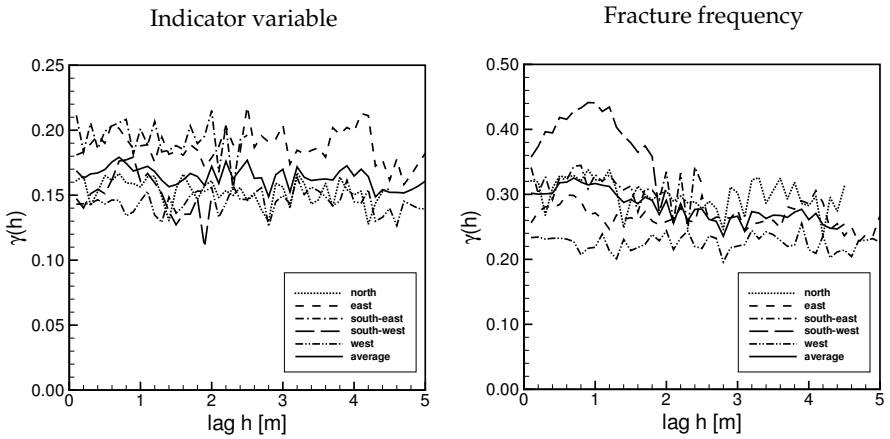

Fig. 5.28. Experimental variograms of the five walls: vector h_i parallel to the scanlines, segment length $l = 0.10$ m.

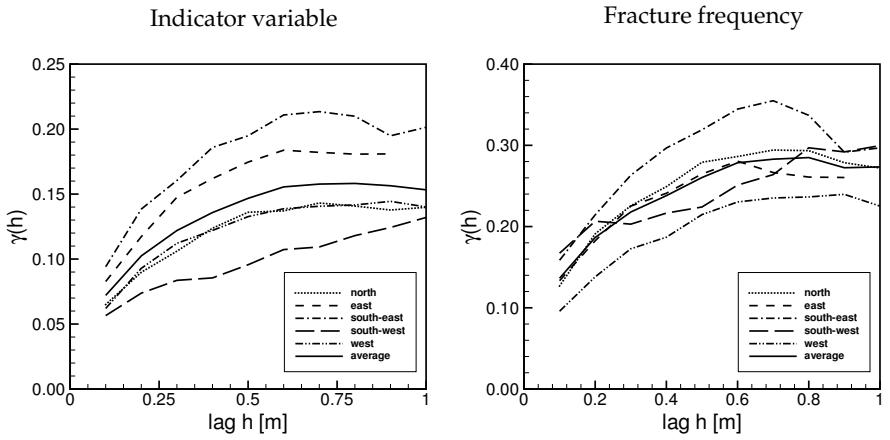

Fig. 5.29. Experimental variograms of the five walls: vector h_i perpendicular to the scanlines, segment length $l = 0.10$ m.

equal for both variogram types. Resulting from this, there is a higher variability in the fracture-frequency variograms, which can be observed in a higher mean and a higher variance. The values of the univariate statistic (mean, variance) and the number of segments for the indicator variable and the fracture frequency are shown in Fig. 5.34 for the five side walls.

5.4.2.2 Vertical Scanlines: Segment Length $l = 0.10\,\mathrm{m}$

Figures 5.30 and 5.31 show the variable fields of the south-west and the west wall as exemples of the five walls of the field block. The indicator and the fracture-frequency field of the single walls are rather similar. The number of segments with a fracture frequency $FF(x_i) > 1$ is not very high compared to the total number of segments. The horizontal fracture distance is generally $\geq 0.10\,\mathrm{m}$, and the natural fractures are indicated clearly by single fracture traces. The opposite case can be observed in the fracture-frequency field of the south-west wall shown in Fig. 5.26. The two variable fields of the south-west wall (Fig. 5.30) show many fracture traces which are longer than 1.0 m. On the other hand, the number of long fracture traces is not very high in the variable fields of the west wall. Here, the short fracture traces dominate the field.

Figures 5.32 and 5.33 show the experimental variograms. As can be seen in the four plots, the variogram values of the south-west wall are clearly higher than the values of the other four walls. The higher proportion of the number of segments with $I(x_i) = 0$ to the number of segments with $I(x_i) = 1$ leads to the higher variogram values. This fact can be observed in the mean and in the variance as well. Figure 5.35, left, shows the values of the univariate statistic of the five different walls.

The variogram analysis with separation vector h_i parallel to the vertical scanlines indicates a nugget effect. This means that the location of the fractures in space is based on a random process. However, the variograms differ in their variability: the variogram values are significantly higher and the expected range of the fracture extension (see Fig. 5.33) is about $2.0 - 2.5\,\mathrm{m}$. The higher variability is based on the larger segment length, as described in Sect. 5.4.2.1 in the case of the horizontal scanlines. The larger segment length leads to a reduced total number of segments. Additionally, the number of segments with $I(x_i) = 1$ within the indicator fields increases, and the number of segments with $I(x_i) = 0$ decreases. This fact leads to higher variogram values.

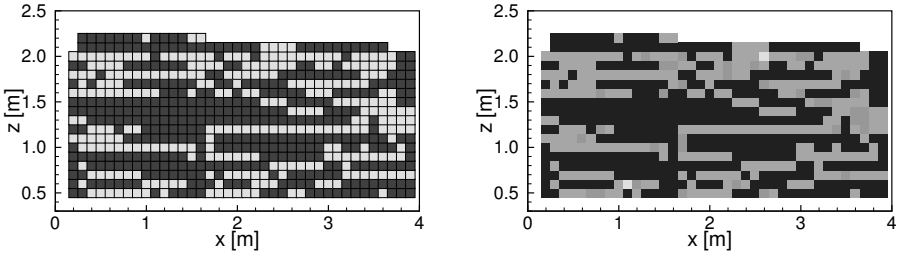

Fig. 5.30. South-west wall: indicator field and fracture-frequency field, scanlines in z-direction, segment length $l = 0.10\,\mathrm{m}$, distance between scanlines $d = 0.20\,\mathrm{m}$.

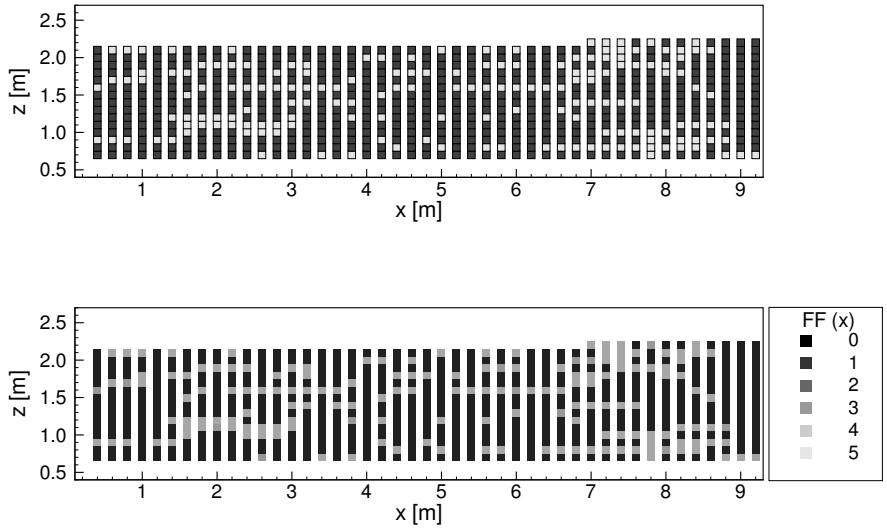

Fig. 5.31. West wall: indicator field and fracture-frequency field, scanlines in z-direction, segment length $l = 0.10\,\mathrm{m}$, distance between scanlines $d = 0.20\,\mathrm{m}$.

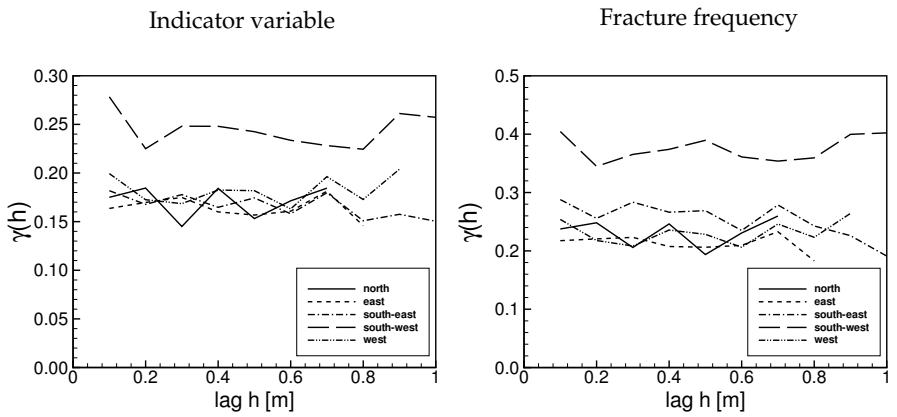

Fig. 5.32. Experimental variogram of the five walls: vector h_i parallel to the scanlines, segment length $l = 0.10\,\text{m}$.

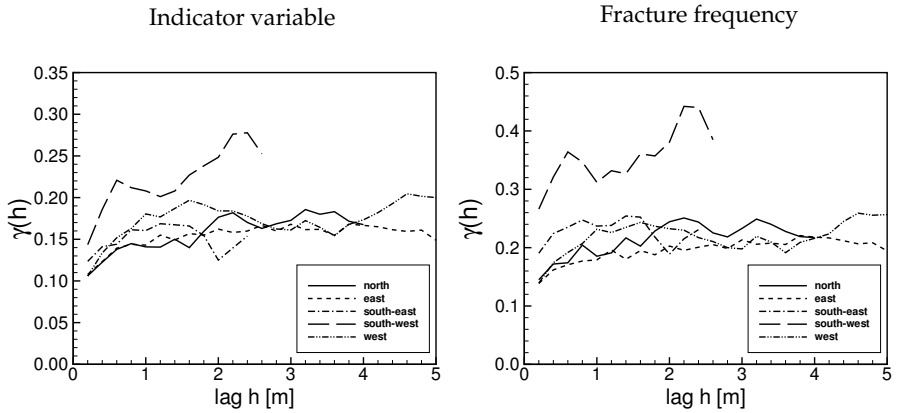

Fig. 5.33. Experimental variogram of the five walls: vector h_i perpendicular to the scanlines, segment length $l = 0.10\,\text{m}$.

5.4.3 Discussion of the Results

A geostatistical analysis of the fracture-trace maps of the five side walls and the top of the field block is conducted. The fracture-trace maps are overlaid by a set of parallel scanlines. The set of scanlines itself is oriented perpendicularly to the main fracture orientation. The scanlines are divided into segments of equal length. The number of intersection points *fracture - scanline segment* leads to the indicator variable (minimum one intersection point existing yes/no) and to the fracture frequency (number of intersection points per scanline segment). The experimental variogram investigations are done in two directions: separation vector h_i parallel to the scanlines, and separation vector h_i perpendicular to the scanlines.

The geoststistical analysis improves the characterization of the field block. It is, however, of great interest to actually implement the knowledge that can be obtained from a geostatistical analysis in discrete numerical simulation models. Currently, the fracture generator FRAC3D (Sect. 2.4.2) is being extended to enable fracture generation based on variograms.

5.4.3.1 Variograms with Separation Vector Parallel to the Scanlines

The variogram investigations parallel to the scanlines focus on the position of the fractures and on the distances of the fractures perpendicular to their main fracture orientation. Some of the variograms show a slight periodic behavior. In the average variogram, the nugget effect dominates the variograms. This means that the spatial arrangement of the fractures is a random process and independent of the neighboring fractures. This is supported by extensive field investigations showing that a Poisson process of the fracture midpoints corresponds to an exponential distribution of the fracture distances (Sect. 2.1). In Sect. 5.3.1, it is shown that the fracture distance distribution at the test site follows an exponential distribution. The assumption that the spatial arrangement of the fractures follows a random process is supported by the exponential distribution of the fracture distances and by the nugget effect of the variograms.

5.4.3.2 Variograms with Separation Vector Perpendicular to the Scanlines

The variogram investigations perpendicular to the scanlines focus on the extension of the fractures along the existing fracture trace. Almost all of the variograms show a steep ascent for small distances $|h_i|$ followed by a flatter ascent. As soon as a threshold value $\gamma(|h_i|) = C$ is reached, the variograms follow an almost horizontal graph. The distance $|h_i|$, at which the threshold value is reached, is called range. Along the direction of the fracture extension, the existence and the extension of a fracture is correlated within this range. This means that the feature *no existence / existence of one or more fractures* at point $x_{i_{P1}}$ depends on the feature at the points $x_{i_0}, x_{i_1}, ..., x_{i_n}$, which

are located in the direction h_i at a distance smaller than/equal to the range to the point $x_{i_{P1}}$. A correlation no longer exists for distances greater than the range. This means that the feature at point $x_{i_{P2}}$, which is located at a distance greater than the range from the points $x_{i_0}, x_{i_1}, ..., x_{i_n}$, is independent of the features of points $x_{i_0}, x_{i_1}, ..., x_{i_n}$.

5.4.3.3 Comparing Indicator Variable $I(x_i)$ - Fracture Frequency $FF(x_i)$

The influence of the segment length on the indicator variable and the fracture frequency is pointed out by Fig. 5.34 and Fig. 5.35. Figure 5.34 is based on the variable fields of the vertical fractures which are overlaid by a set of horizontal scanlines. Figure 5.35 shows the results for the variable fields of the horizontal fractures which are overlaid by a set of vertical scanlines. The two figures present the results of the univariate statistic of the indicator and the fracture-frequency fields. The mean value, the variance, and the number of segments per variable field are plotted for the segment lengths $l = 0.04$ m, 0.10 m, 0.20 m.

Here, the difference between the indicator variable and the fracture frequency is discussed for the example of south-west wall for the vertical fractures. For the segment length $l = 0.04$ m, the mean value and the variance are almost equal for the indicator-variable fields and the fracture-frequency fields as can be seen in Fig. 5.35 and in Table 5.5. This means that the measurement set with a segment length of $l = 0.04$ m is so fine that almost all fracture traces are detected in an individual segment. Only a few segments comprise a fracture frequency of $FF(x_i) > 1$. The fracture frequency of $FF(x_i) > 1$ points to the following fact: fracture traces which are located very close together (within a segment of $l = 0.04$ m) have to be interpreted as one single natural fracture trace. For the segment length of $l = 0.10$ m, there are clearly higher values for the mean and the variance and smaller values for the number of segments. This trend continues for the analysis with segment length $l = 0.20$ m, the reason being that the number of segments with $I(x_i) = 0$ and $FF(x_i) = 0$ decreases and the number of segments with $I(x_i) = 1$ and $FF(x_i) > 0$ increases for larger segment lengths. This leads to a higher mean value and variance.

As a result of larger segment lengths, the difference between the mean value and the variance gets more significant for the indicator variable and

Table 5.5. South-west wall: mean, variance, number of segments.

Segment length	Indicator variable		Fracture frequency		Number of
	Mean $\bar{x}_I$	Variance s_I^2	Mean $\bar{x}_F$	Variance s_F^2	segments
0.04 m	0.0929	0.0843	0.1084	0.1311	1743
0.10 m	0.1994	0.1596	0.2713	0.3971	682
0.20 m	0.3647	0.2317	0.5500	0.7887	340

the fracture frequency. Considering the mean value

$$\bar{x} = \frac{1}{n} \sum_{i=1}^{n} x_i \tag{5.5}$$

and the variance

$$s^2 = \frac{1}{n-1} \sum_{i=1}^{n} (x_i - \bar{x})^2 \tag{5.6}$$

leads to a better understanding of the differences. A comparison of indicator field and a fracture frequency field based on the same scanline measurement set shows that the total number of segments n and the number of 0-segments ($I(x_i) = 0$, $FF(x_i) = 0$) are equal for the two fields. The maximum value of the indicator field can reach $I(x_i) = 1$. In contrast, the maximum value of the fracture-frequency field can reach $FF(x_i) \geq 1$. The sum $\sum_{i=1}^{n} x_i$ of the fracture-frequency field is at least equal to the sum $\sum_{i=1}^{n} x_i$ of the indicator field. In most cases, the sum of the fracture-frequency field is higher than the sum of the indicator field. Therefore, the mean value $\bar{x}_F$ of the fracture-frequency field is equal to or larger than the mean value $\bar{x}_I$ of the indicator field. The total number n and $n-1$ of the segments is equal for both variable fields. Based on the higher variability of the fracture frequency, the increment $(x_i - \bar{x})$ reaches higher values as in the case of the indicator variable as well. These different facts lead to higher variance values for the fracture-frequency fields. Figure 5.26 clearly shows the different segment values for the indicator field and the fracture-frequency field on the basis of the same scanline measurement set for the south-west wall.

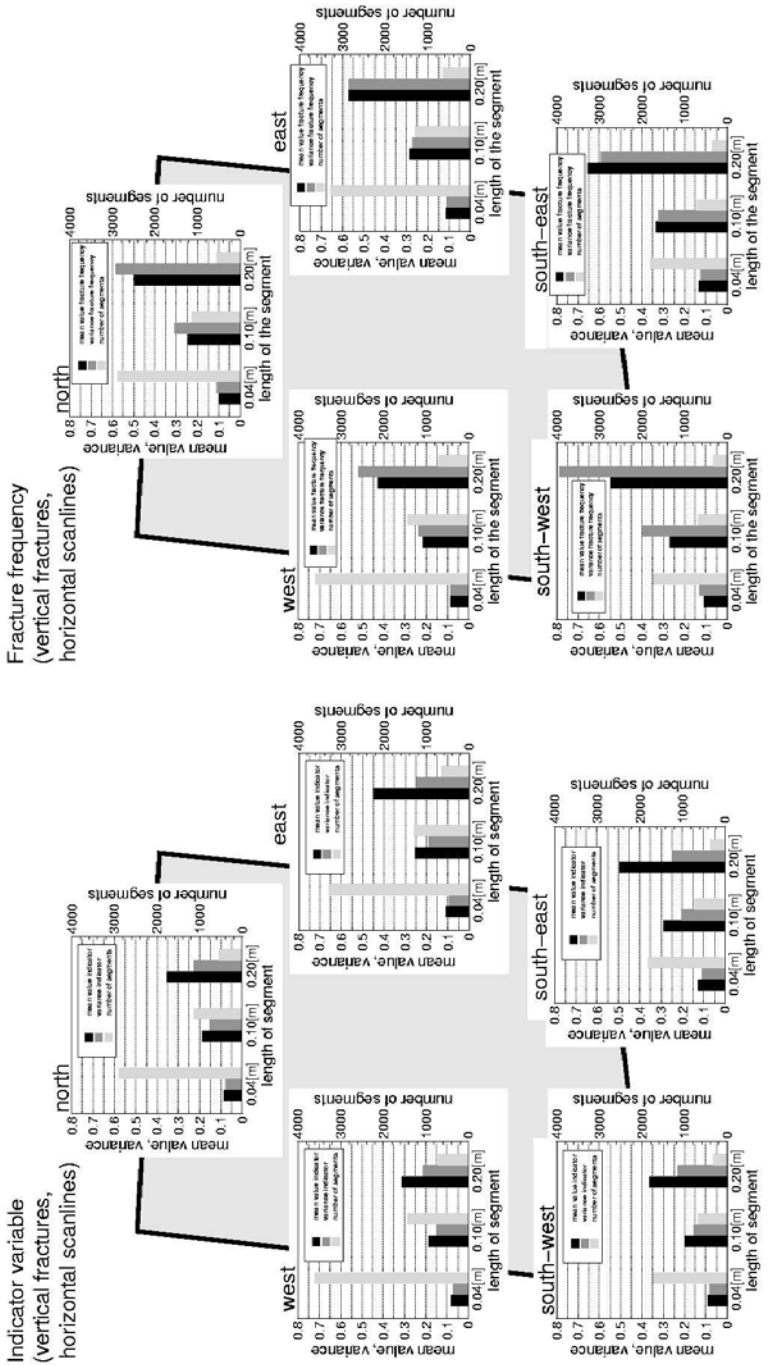

Fig. 5.34. Mean, variance, number of segments of the variable fields (left: indicator variable, right: fracture frequency) for vertical fractures.

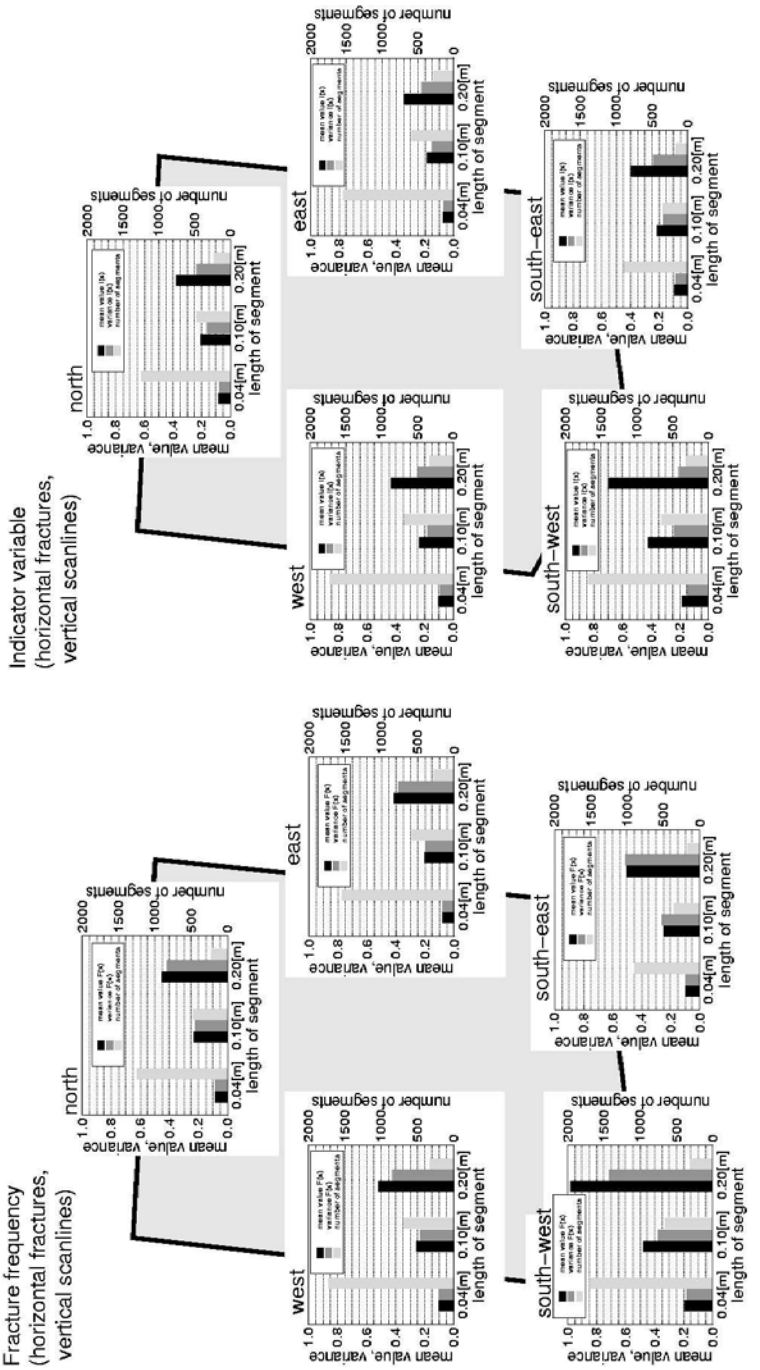

Fig. 5.35. Mean, variance, number of segments of the variable fields (left: indicator variable, right: fracture frequency) for horizontal fractures.

5.4.3.4 Top of the Field Block: Comparing the Variability of the Vertical Fractures

A trend of the variogram values can be observed in the experimental variograms with separation vector $h_i = (0, y)$ of the vertical fractures of segment length $l = 0.04\,\text{m}, 0.10\,\text{m}, 0.20\,\text{m}$. As can be seen in Fig. 5.29, the variogram values of the west wall are generally the lowest, whereas the values of the south-east and the east wall are generally the highest. An additional hint of a possible north/west - south-east/east trend can be gained from a comparison of the mean and the variance of the different side walls in Fig. 5.34. The mean and the variance are mostly higher for the southern and eastern walls than for the western and northern walls. This leads to the assumption that the number of fractures may be higher in the south-east area of the field block than in the north-west area.

In addition to the variograms, the mean and the variance of the different side walls, the top of the field block gives further information about a possible north/west - south-east/east trend. The fractures which can be seen on the top of the field block in Fig. 5.36, left, are fracture traces of the two vertical fracture clusters. The fracture map is overlaid by a mesh of size $0.10\,\text{m} \times 0.10\,\text{m}$. The number of fractures which intersect one cell is recorded in Fig. 5.36, right. Figure 5.36, right, does not give a significant suggestion of a higher fracture frequency for the south-east/east corner of the field block.

However, there is a higher fracture frequency for the cluster $S_t = 56^\circ$ than for the cluster $S_t = 139^\circ$. Comparing the experimental variograms of the vertical fractures of the top plane shows that the variogram values for the cluster $S_t = 56^\circ$ are higher than the variogram values for the second cluster with direction $S_t = 139^\circ$.

5.4.3.5 Comparing the Range and the Segment Length

The influence of the segment length on the range is investigated by assessing the experimental variograms with separation vector h_i perpendicular to the scanlines. Figure 5.37 presents the comparison of the approximated average value of the range of all side walls versus the segment length $l = 0.04\,\text{m}$, $0.10\,\text{m}$, $0.20\,\text{m}$, $0.30\,\text{m}$. The values of the ranges come from the experimental variograms. Three pairs of graphs are seen in in Fig. 5.37. There is no large difference between the range of the indicator variograms and the range of the fracture-frequency variograms for the single pairs.

The pair of graphs of the vertical fractures (fracture traces on the side walls) does not show a strong dependence of the range and the segment length. The vertical fractures are always recorded as single fracture traces and not as different, disconnected fracture traces. The surface maps, which can be seen in Figs. 5.23 and 5.24, support this fact. Additionally, the direction of the fracture traces is almost parallel to the z-axis. The scanline mesh (set of horizontal scanlines perpendicular to the almost vertical fractures) causes

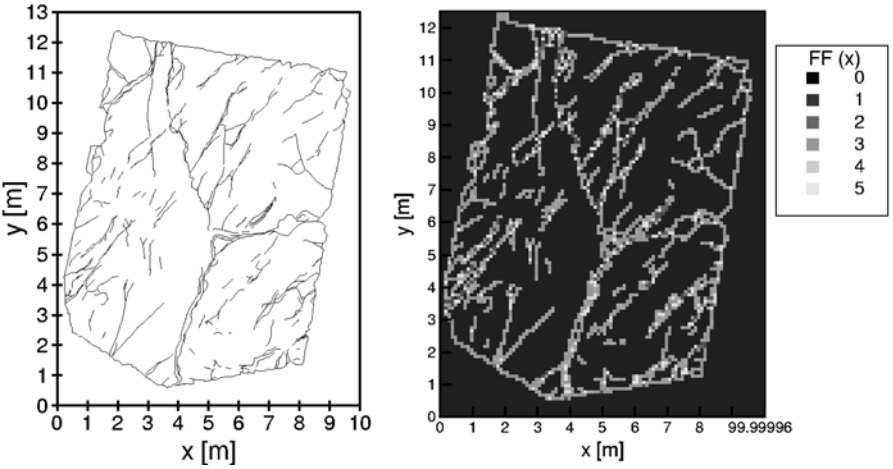

Fig. 5.36. Top of the field block. Left: fracture mapping. Right: fracture frequency per grid element 0.10 m × 0.10 m.

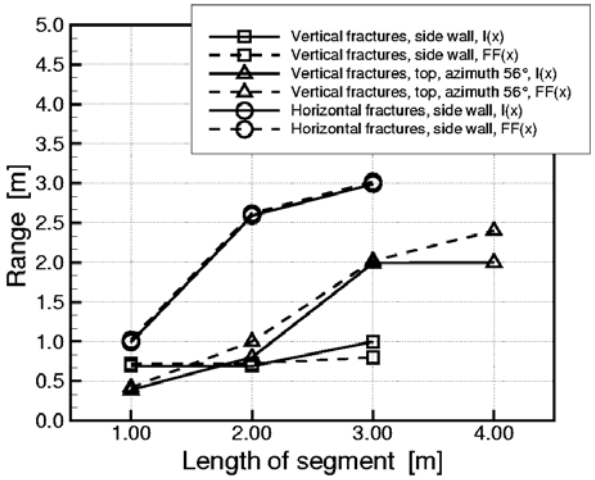

Fig. 5.37. Comparing range versus segment length.

the following effect: the single fracture traces are not recorded in diagonal scanline segments. They are recorded in segments, which lie on a straight line, independently of the segment length used.

The second pair of graphs of vertical fractures from the top of the field block (Fig. 5.37) shows a significant dependence of the range and the segment length. Between the segment lengths $l = 0.04$ m and 0.10 m, the range

increases very slowly. This is followed by a strong increase of the range between the segment lengths $l = 0.10\,\mathrm{m}$ and $0.20\,\mathrm{m}$. Between the segment lengths $l = 0.20\,\mathrm{m}$ and $0.30\,\mathrm{m}$ the range is almost constant. The reason for the strong increase of the range is that, with the use of a larger segment length, single fractures which lie very close together and almost parallel on a line form a quasi-new longer fracture trace. The scanline mesh runs perpendicularly to the main fracture direction (strike $S_t = 56^\circ$ and azimuth $A_z = 146^\circ$, Table 5.2) but the orientation of the fracture traces varies slightly around the main direction. This is seen in Fig. 5.36, left. Consequently, the scanline mesh does not run exactly perpendicular to the fracture traces. A scanline mesh based on small segment lengths divides a single fracture trace into several "new" shorter fracture traces. A variogram investigation based on such an incorrect variable field (indicator or fracture-frequency field) leads to a smaller range, which does not represent the real natural range of the fracture traces. The choice of a larger segment length reduces or prevents this error.

The pair of graphs of the horizontal fractures shows a relatively steep ascent of the range between the segment length $l = 0.04\,\mathrm{m}$ and $0.10\,\mathrm{m}$. However, the ascent of the range between length $l = 0.10\,\mathrm{m}$ and $0.20\,\mathrm{m}$ is very small. The reason for the large ascent is the same as described above. The horizontal fractures are not oriented absolutely parallel to the main direction, the x-axis. The choice of a fine scanline mesh (set of vertical scanlines with small segment lengths) and the more or less horizontal fractures lead to the same error: single, not exactly horizontal fractures are divided in new shorter fractures. By the use of a coarser mesh (larger segment lengths with $l = 0.10\,\mathrm{m}$, $0.20\,\mathrm{m}$), the error can be avoided. However, using a mesh which is too coarse leads to the following problem: real single fractures are interpreted as new, longer fracture traces. One has to investigate different sizes of mesh (different distances between scanlines, different segment lengths) in order to indicate the jumps within the graphs of range versus segment length.

5.5 Orientating Measurements at the Unsealed Field Block

C. Thüringer, M. Weede, R. Bäumle, H. Hötzl

Before the final shaping and sealing of the field block, some orientating experiments are conducted. On the one hand, information about the fracture connectivity and the range of flow velocities inside the field block are gathered by applying simple connectivity and flow experiments with gas tracers. On the other hand, ground-penetrating radar (Georadar) provides the opportunity, of making structural inhomogeneities inside the field block visible, before it is encapsulated, making this method impossible to use.

5.5.1 Connectivity and Flow Tests

To assess the fracture connectivity inside the field block experimentally, gas-tracer tests are conducted, using carbon dioxide (CO_2) as an artificial tracer. CO_2 is injected into the sandstone through several injection boreholes in a certain area of the test site. The injection occurs by an excess pressure of 1 bar and a flow rate of 5 to 10 m^3/h, using a packer system in order to seal the borehole against external atmospheric influences.

The tracer gas is injected both as a continuous injection over a period of several minutes and as a short impulse of 120 seconds. In this way, not only the horizontal extension of interconnected fractures, but also the effective flow velocity of the gas impulse between points of injection and detection can be determined.

Gas detection occurs at gas measuring gauges. These consist of 20 cm drill holes with embedded polyamide tubes and quick-release couplings. In order to make the measuring gauges airtight, the annulus between tube and drill hole has to be filled with clay and ideally secured with cement. The measuring gauges are installed on the surface of the sandstone field block along the fracture trace lines and, where appropriate, between the fractures directly on the rock matrix.

To determine the CO_2 concentration, an infrared spectrometer is used. Its effective measuring range is from 0.05 to 50 vol.-% CO_2. Data acquisition occurs every 20 seconds.

Figure 5.38 shows a sketch map of the unsealed raw test site with the three horizontally oriented gas-tracer-injection boreholes (GTB1 to GTB3). The thin black lines represent the trace lines of the main fractures, the black dots the 45 gas measuring gauges.

Connectivity tests applied at the test site prove that fractures are well interconnected, in some cases over a horizontal distance of about 5 m. Effective flow velocities of 1 to 4 m/min were determined by impulse tests, using the direct distance between the points of injection and detection.

5.5.2 Electromagnetic Reflection Method

The electromagnetic reflection method (EMR) is also known as Georadar. It is a geophysical technique, based on the reflection of high-frequency electromagnetic waves from 10 MHz up to 4000 MHz at material boundaries with different dielectric properties (Vogelsang (1991); Militzer *et al.* (1986)). Basically, this method is used to identify inhomogeneities in physical parameters in the ground, such as electrical conductivity [S/m] and the relative dielectric constant.

Electrical conductivity affects the depth of intrusion of the electromagnetic wave. The attenuation of the electromagnetic signal and consequently the maximum depth of intrusion is inversely proportional to the electrical

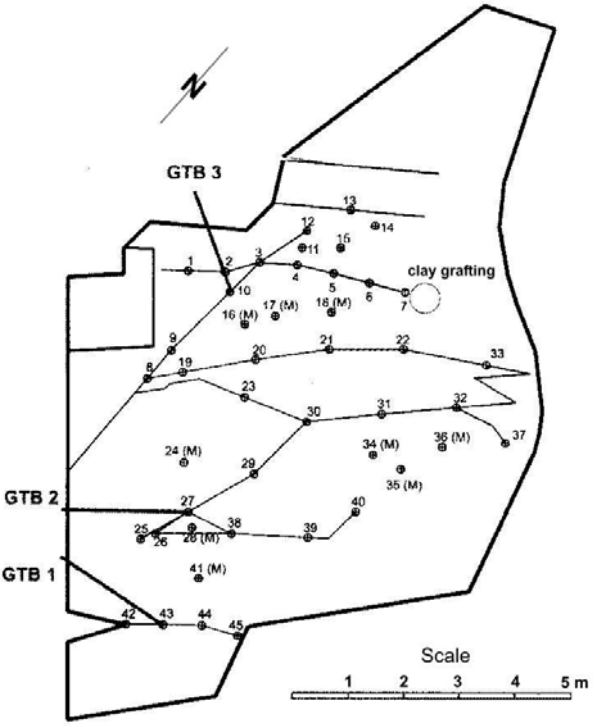

Fig. 5.38. Experimental setup of the fracture connectivity tests at the raw test site with 45 gas measuring gauges and three gas tracer injection boreholes (GTB).

conductivity of the medium. Clay minerals and water-filled pores or fractures normally increase the electrical conductivity and thus decrease the depth of intrusion dramatically.

The velocity of propagation of the emitted and reflected wave and the amount of reflected energy is affected by the non-dimensional relative dielectric constant. In natural materials, this parameter is between 1 (air) and 81 (water). The relative dielectric constant of dry sand, for example, is 3 to 5. With increasing frequency of the electromagnetic wave, the wavelength decreases and the resolution increases, independently of the material under investigation. In contrast to this effect, the depth of intrusion decreases with increasing frequency. The decision on which range of frequency to use depends on the required depth of intrusion and the favored resolution. Thus, EMR measurements should be applied with at least two different frequencies. Which frequency to use is not only a question of the availability of technical equipment, but also of the geological conditions and the structures being investigated. At the *Pliezhausen* test site, EMR measurements were carried out in cooperation with the Department of Geophysics (Karlsruhe Uni-

versity) in September 1997, using SIR-3-equipment with both 900 MHz and 500 MHz antennas. As the data evaluation occurs at the raw field block before the side walls are finally cut, it is also possible to record radargrams along two orthogonal cutting lines marking the east and north faces of the future field block. After the final cuttings, these radargrams can be compared to the created outcrops, making a quantifiable geological interpretation possible.

The whole field block is scanned and the positions and orientations of fractures and sedimentary structures are determined with EMR technology. The measurements were carried out in cooperation with GUS, geophysical services Karlsruhe, in March 1999. The following specifications mainly refer to the GUS report (GUS, 1999).

The measurements are carried out on the surface of the field block along crossing profiles fixed every 25 cm (900 MHz antenna) and every 100 cm (500 MHz antenna). On the side walls, the distance from line to line was 50 cm (900 MHz antenna).

Radargrams are digitally recorded and saved with the dipole direction of the antennas situated vertically to the profile directions. The time window for recording the radargrams is 40 ns (900 MHz antenna) and 60 ns (500 MHz antenna). Before they are analyzed, they are filtered and migrated several times. To locate extensive reflectors, time slices of the radargrams are calculated by averaging over the absolute amplitude in each time and distance interval. Amplitudes of a time slice affect the reflection intensity in the depth and distance range. For 900 MHz measurements, the time interval is chosen in such a way that it represents a depth interval of 5 cm. For this range of frequency (5 cm interval, 0-150 cm depth), 30 time slices are calculated whereas 20 time slices are calculated for 500 MHz measuring (10 cm interval, 0-200 cm depth).

As a bench mark, a geodetic point at the south-east corner of the field block surface is chosen. The coordinates of each reflector, identifiable in at least two adjacent measuring profiles and reaching over more than 1 m, are saved in a separate file. To avoid misinterpretation, smaller reflectors are only recorded at less than 1 m distance to the sidewalls of the test block. The intensity of reflections is dominated by their distance to the measuring profile, fracture filling, saturation, fracture geometry and aperture. Reflections of water- or clay-filled fractures are generally of higher intensity than reflections of air-filled, open fractures. For a reliable detection, the fracture aperture must not be considerably smaller than 1 mm.

The depth of the water-table below the test-site surface is about 5 m during the EMR measurements. Thus, the sandstone block with its thickness of 2 m is completely unsaturated with no afflux at the base. Both in the calculated time slices and in the radargrams, many reflectors, their orientation and their contours can be identified.

The two most dominant, almost horizontally oriented reflectors inside the test block recorded by EMR measuring at the surface are:

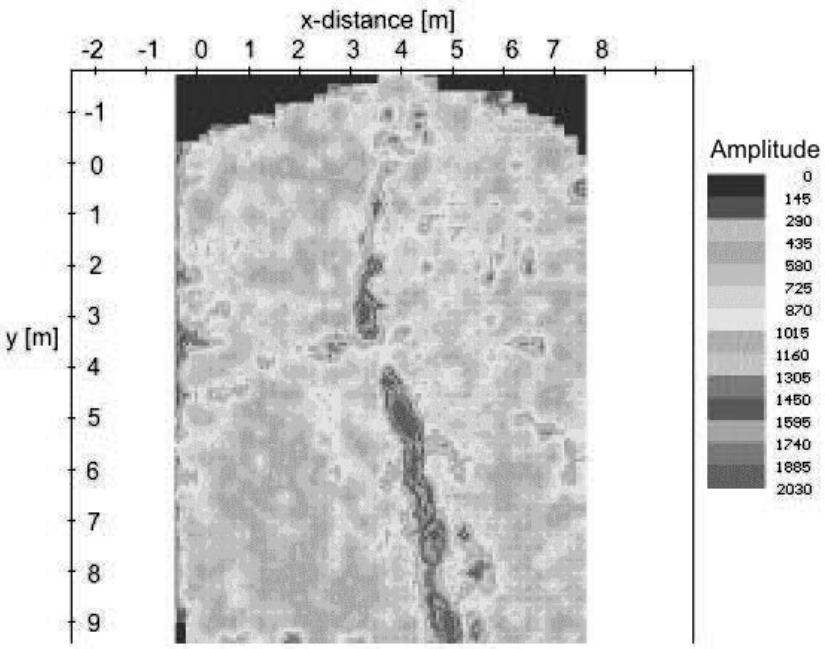

Fig. 5.39. Time slice of depth range 0.95 m to 1.00 m, calculated from unmigrated radargrams with 900 MHz antenna at the field block.

- reflector x = 2.0 to 3.5 m, y = 3.5 to 5.2 m, z = 0.85 to 1.05 m below the surface dipping north-east,
- reflector z = 0.90 to 1.10 m extending almost across the entire field block.

The depth range 0.95 m to 1.00 m below the surface of the block shows a reflection plane oriented north-west to south-east (in Fig. 5.39, north is oriented downwards). It seems to dip steeply and bend to the south in the middle part of the field block. A second, less dominant and orthogonally oriented (south-west to north-east) reflector is visible in the middle left part of Fig. 5.39.

5.6 Flow and Transport Tests at the Sealed Field Block

M. Weede, C. Thüringer, H. Hötzl

With completely encapsulating the whole field block, one fundamental precondition for setting up controlled flow fields within the test site can be

achieved. In the following chapter, the technical background as well as the results of the gas-flow and gas-tracer tests applied at the test site *Pliezhausen* are described.

5.6.1 Tracer Injection and Detection Techniques

In order to gain information about the flow and transport parameters of fractured porous media, gas tracer tests are conducted in the gas-saturated field block. For this purpose, a flow field is artificially created over a certain distance via boreholes and gas tracers are injected into the system to investigate.

For each conducted flow and transport experiment two boreholes are used: one borehole is connected to an extraction device to generate low pressure in the borehole and therefore in the field block. The second borehole is opened in order to allow free inflow into the otherwise sealed system. After a certain period of time, a constant flow field will be set up from one borehole to the other inside the fractured porous block. The resulting boundary conditions at the boreholes are constant extraction pressure ($P_{extract}$) and constant inflow pressure, which equals atmospheric pressure ($P_{inflow} = P_{atmos}$). Certain ranges of depth within the boreholes can be tested separately when using packer systems.

After steady flow conditions are reached, impulses of gas tracers (helium (He) and sulfur hexafluoride(SF_6)) are unpressurized injected into the injection borehole while recording the time-depending change of concentration within the air, extracted at the extraction borehole. During the experimental investigation of transport processes by gas tracer tests, the unpressurized injection is an important criterion to fulfill when developing a suitable injection method. By doing so, a significant compression of the gas tracer inside the injection borehole can be avoided.

Tracer injection by a bypass arrangement, as usually applied in aquatic tracer tests, is inappropriate at the test site as the injected gas-tracer mass is insufficient for a significant signal at the detection borehole. Therefore, tracer injection occurs as a direct impulse from the gas bottle. To ensure an unpressurized injection, a pressure equalization box is interposed, in which the temperature of the injected gas can be determined simultaneously (Fig. 5.40). The flow rate of tracer gas out of the bottle and into the box is adjusted to be higher than the passive, unpressurized borehole inflow in order to achieve an injection of undiluted tracer gas into the system.

The injected tracer mass is calculated on the basis of the flow rate and injection time. Actually, this procedure is only correct for incompressible NEWTON fluids as it is based on the continuity equation of the volume. Water, which can be assumed to be incompressible, fulfills this condition in contrast to compressible gases (air, He, SF_6,CO_2...). On the assumption of a non-compressible, constant density flow of air for the time of tracer test, this method can be accepted as sufficiently accurate, provided that the injection is unpressurized and the temperature constant. In addition, investigations

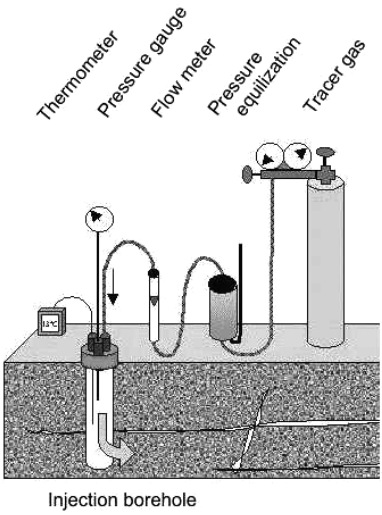

Fig. 5.40. Experimental set-up for gas-tracer injection at test site *Pliezhausen*.

by Jaritz (1999) show that, under steady-state conditions, the error regarding gas as a non-compressible fluid is negligibly small.

The injected tracer gas and the extraction rate are determined by volume flow meters. Pressures at the boreholes are measured by horseshoe-bend manometers with an accuracy of 0.5 mm to 1.0 mm water column (according 5.0 Pa to 10.0 Pa). Rock humidity is selectively measured by a TDR system inside the boreholes.

Tracer gas is detected within the extraction flow at the detection borehole by an online measuring system. To determine helium, a gas detector (HELITEST®) is used. The tracer gas is sampled and analyzed continuously. The measured concentration is recorded every second or every several seconds, depending on the controlling software with a measuring range up to 65 000 ppm.

Sulfur hexafluoride is detected by a field gas chromatograph with an electron collection detector (GC-ECD). When it is in automatic sampling mode, the minimum sampling interval is 120 seconds. This is the period of time needed for the automatic flushing of the measuring chamber and a sampling line with inert gas.

For a more detailed resolution of the tracer breakthrough, an additional manually operated sampling is applied every 20 seconds at the detection borehole. A common measuring range is between 0.02 ppb and 20 ppb.

It should be mentioned that for all conducted experiments, the rate of extraction was always higher than the volume flowing into the field block.

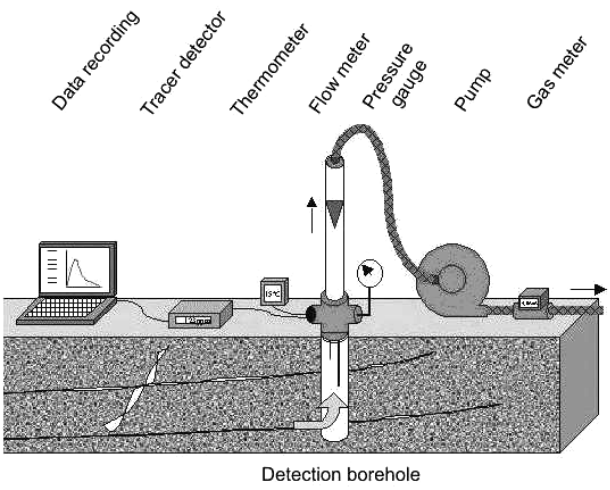

Fig. 5.41. Experimental set-up for gas-tracer detection at test site *Pliezhausen*.

The ratio between extraction rate and flow rate into the block was never balanced. Even an extraction lasting several days with unvaried boundary conditions did not make a change, as expected for a completely sealed system. Although the flow rates and pressure conditions are constant at both boreholes after several hours of testing and steady flow can be expected, the rate of extraction was still a multiple of the flow into the block.

Two reasons can be causal for this observation:

- influence of gas compressibility:
  By the pressure difference at the injection and extraction borehole, differing gas density due to compressibility and therefore differing volumetric gas flow rates can be expected at the boreholes. However, as investigations by Jaritz (1999) show, the error of dealing gas as a non-compressible fluid under steady state conditions in the pressure range of the experiments is negligibly small.
- incomplete sealing of the field block:
  It can be expected that the sealing of the block was not completely gas proof. By different technical arrangements as the afflux of water at the block basement, this problem can partly be equalized.

The permanent air draft within the field block causes a drying of the clay marls which has to be compensated by an extensive drenching of the basal layers in order to prevent them from cracking and leaking. At outcrops existing during the construction phase of the test site, the changing consistency

of this material, depending on its water content can be examined. This phenomenon bases on the high content of swellable clay minerals within the basal layers, which get hydrated and expand in contact with water. Drying the base marls causes the risk of fracturing and thus the generation of flow channels for the air outside to intrude into the depressurized block. Earlier investigations indicate the enormous influence of gas flowing through the basement into the field block using high conductivity fractures, when assuming a close contact between sandstone and marl basement.

5.6.2 Measurements at Marginal Boreholes

During the initial experimental phase of this study,exclusively marginally installed boreholes are used for tracer experiments on the field block. This is based on the idea of investigating transport processes at as long experimental distances between two boreholes as possible. At that time, the influences of the field block boundaries, appearing along the defining test site walls, are not regarded in the analysis. However, a detailed discussion of the influence of the field block boundaries is given in Sec. 5.9.

By using the boreholes in the edges of the field block (Fig. 5.11), several variably shaped breakthrough curves can be recorded. As a result of these experiments, information about transport velocities (e.g. maximum velocity, dominating velocity, and mean velocity) and tracer concentration can be gathered. Furthermore, the shape of the curve can give indications for kind and number of the different flow channels, involved in the transport. Narrow and temporally sharp defined peaks can be interpreted as fast, advective dominated transport through well accessible fractures. In contrast, wide and flat peaks indicate a more dispersive-diffusive dominated transport through small ancillary fractures or the rock matrix. Figure 5.42 reviews the different shapes of breakthrough curves, measured in tracer tests between the marginal boreholes in the field block. It accentuates the variable curve shapes and the different ranges of time and concentration scales.

Influence of Thermal Fluctuations

In addition to the type of flow path (main or ancillary fractures, rock matrix) it is found that variations in temperature have great influence on the experimental results when applying gas flow and tracer tests to the field block. This influence of system temperature is exemplarily investigated by the comparison of helium tracer tests applied in winter and in summer time. The most noticeable difference has been recognized during field work in summer: detection of tracer gas at the detection borehole is difficult as the recorded concentration of helium is much smaller than in winter tests. Also the recovery rate of the tracer mass injected, is only a fraction of comparable winter tracer tests. The recovery rate of helium in summer is at an average of about 1 to 5 %. Helium tracer tests in winter show recovery rates of mostly 40 to 80 %, with temperature below zero even up to 90 %. In Fig. 5.43 tracer break-

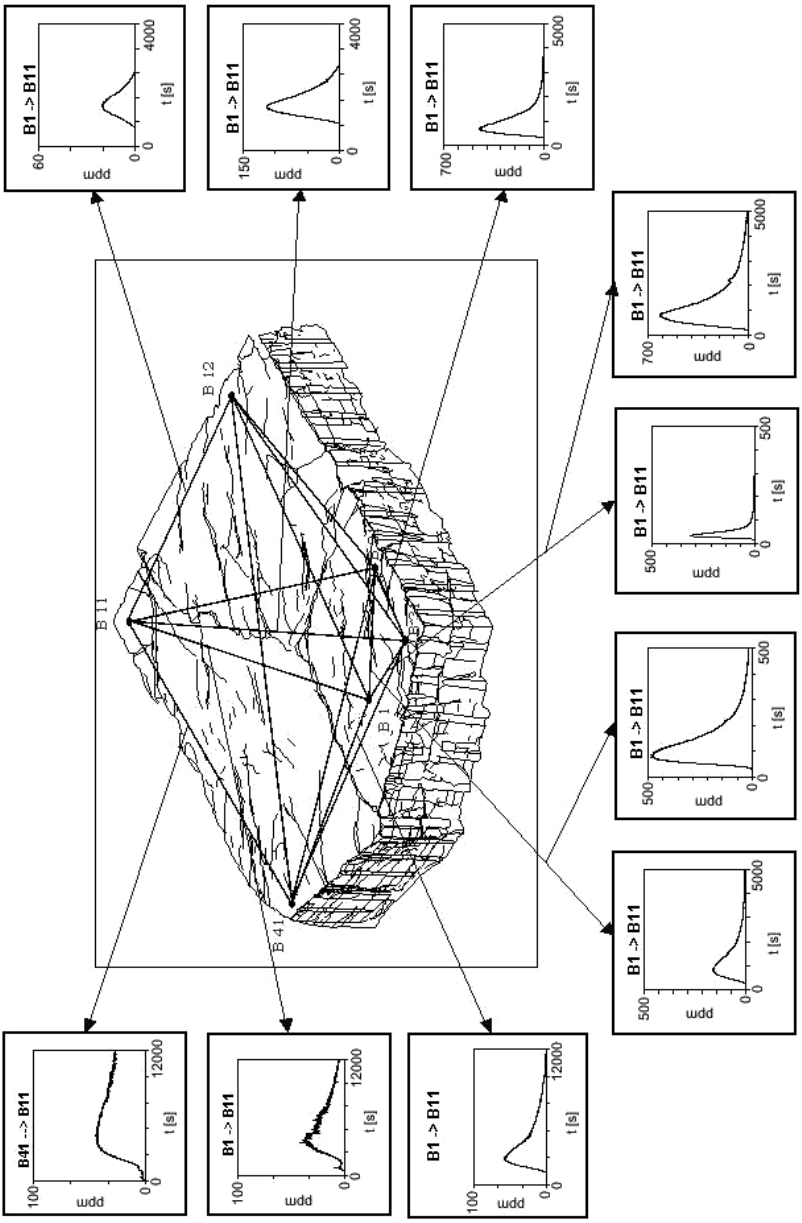

Fig. 5.42. Experimentally determined tracer-breakthrough curves at different hole-to-hole connections in the field block.

through curves of helium-tests in summer and in winter between B31 and B1 are compared. During these experiments, the temperatures at detection boring B1 are -2.1 °C during the winter test and 19.5 °C during the summer test.

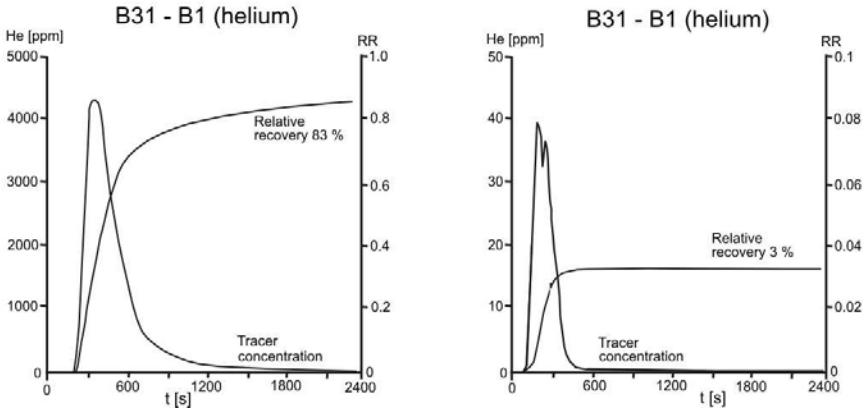

Fig. 5.43. Breakthrough curves and recovery rates of helium tracer tests in winter (left) and summer (right). Note the different scaling between the graphs.

Another significant difference, shown in the diagrams of Fig. 5.43 is the range of concentration, recorded in winter (left) and summer (right). The maximum concentration in winter is 4500 ppm and in summer about one hundredth (42 ppm). This is only partly caused by the higher pressure gradient between extraction borehole B1 (p_{out} = 550 Pa) and injection borehole B31 (p_{in} = 120 Pa) in winter and the 10-times higher tracer input mass M of 327 mg He (28.7 mg He in summer), which is sucked passively into the system (using the same extraction rate Q).

Table 5.6. Experimental parameters of tracer tests with He.

Test type	T [°C]	P_{out} [Pa]	P_{in} [Pa]	Q [l/sec]
He-winter	-2.1	-550	120	1.05
He-summer	19.5	-560	40	1.13

Peak shape and number of the helium tracer test breakthrough curves between B31 and B1 differ depending on temperature, too. Whereas in winter there is always one clearly defined single helium peak, in summer in He-tracer tests two peaks are recorded (Fig. 5.43). The single peak, measured in winter tests, is characterized by a quick concentration increase and a relative

Table 5.7. Experimental parameters of tracer tests with He.

Test type	M [mg]	t_1 [sec]	C_{max} [ppm]	RR [%]
He-winter	327.0	160	4500	92.9
He-summer	28.7	124	42	3.2

short but wide tailing. The recovery rate rises up to 93 % at the end of the observation time, 100 min after tracer injection. In summer tests, the recorded time-related concentration rises very quickly to the first of the double peak and then decreases rapidly with a small second peak. The shape of the recovery rate indicates that right after the second peak no more tracer can be recovered, which is only 7 min after the injection. Altogether only about 3 % of the helium can be recovered at the registration borehole.

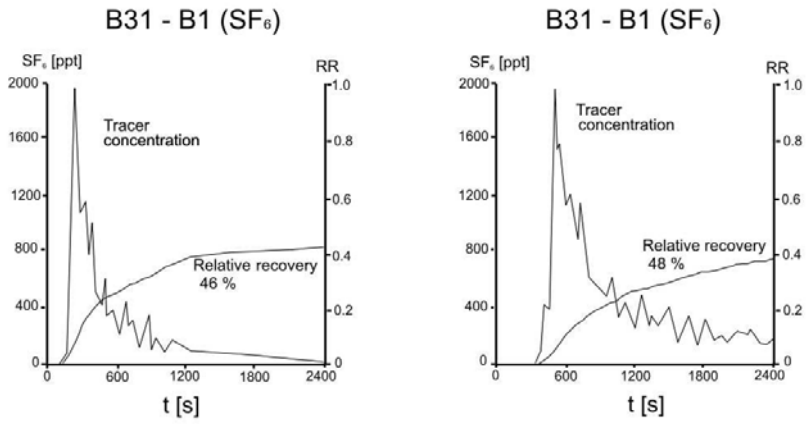

Fig. 5.44. Breakthrough curves and recovery rates of SF6-tracer tests in winter (left) and summer (right).

The tracer gas SF_6 does not show such significant variations when applied in changing temperature conditions. As displayed in Fig. 5.44, also the SF_6 tracer breakthrough recorded in summer includes at least two different peaks and a significant tailing, similar to the He tracer tests in winter. But the recovery rate of the summer test is continuously increasing until the end of observation time after 5400 s, up to 48 % (compared to about 3 % with He in summer). Obviously, the tracer gas SF_6 seems to be less affected by temperature variations.

Preliminary Analytical Parameter Study

As an initial interpretative approach, the measured breakthrough curves are described by simple analytical models in order to gain information about the dominating transport mechanisms.

The recorded tracer breakthrough curves are adapted by the general transport equation (Lever *et al.* (1985) and Tang *et al.* (1981)) for two-dimensional transport of water solute material in a single fracture, in a radial convergent flow field (Sec. 2.3). Each part of this differential equation represents one of the different mechanisms taking place during mass transport. Solutions of the differential equation for the two-dimensional transport in a fracture in a radially convergent flow field are given by Lenda and Zuber (1970) in form of an advection-dispersion-model (ADM) and by Maloszewski and Zuber (1990) in form of a single-fissure-dispersion-model (SFDM). The time dependent tracer concentration at an observation point in transport direction is:

SFDM (Maloszewski and Zuber, 1990):

$$C_f(t) = \frac{aM}{2\pi Q}\sqrt{(Pe \cdot t_0}\int_0^t exp\left(-\frac{Pe(t_0-u)^2}{4ut_0} - \frac{a^2u^2}{t-u}\right)\frac{du}{\sqrt{u(t-u)^3}} \quad (5.7)$$

ADM (Lenda and Zuber, 1970):

$$C(x,t) = \frac{M}{Q}\frac{x}{\sqrt{4\pi D_L t^3}}exp\left(-\frac{(x-v_a t)^2}{4D_L t}\right) \quad (5.8)$$

with:

$$D_L = \frac{v_a x}{Pe}; a = \frac{n_e\sqrt{D_P}}{b}; t_0 = \frac{x}{v_a} \quad (5.9)$$

The application of this approach requires the following simplification of initial and boundary conditions:

- Gas flow primarily occurs at few fractures. By the injection and detection of tracer gas at single boreholes in connection with an orthogonal fracture network this condition can be assumed as approximately fulfilled.
- Transversal dispersion is negligible. Tracer is injected directly into the main flow between injection and detection boring. Thus the effect of transversal dispersion can be prevented particularly at tracer detection boring.
- Tracer is uniformly distributed inside the whole injection borehole at test initiation. This condition has been assumed without the possibility of verification, due to the unavailable recording of tracer injection concentration.

By an iterative adaption of the parameters to fit the experimental tracer breakthrough curves (Fig. 5.42), transport in the field block can be described, using the Peclet number *Pe*, the mean transit time t_0 and the diffusion parameter *a*. Figures 5.45 and 5.46 show that a satisfying adaption to the breakthrough curves, measured at the field block by Thüringer (2002) can be achieved, applying the SFDM.

Table 5.8. Fitted transport parameters of gas tracer tests at test site *Pliezhausen*.

		t_0 [min]	Pe	α_L [m]	a
He	ADM	7.6	13.1	0.15	-
	SFDM	5.9	30.7	0.06	0.011
SF_6	ADM	11.5	4.8	0.40	-
	SFDM	5.4	31	0.06	0.025

This composition clarifies the main differences between ADM and SFDM. As the ADM describes transport only by advective and dispersive processes, the SFDM also implements diffusion-caused retardation by the introduction of the diffusion parameter *a*. Thus the dispersive part of the tailing decreases and the Peclet-number increases, applying the SFDM.

Experiments in fissured aquifers frequently show a tailing in concentration declension which can have many different reasons. This must in no case

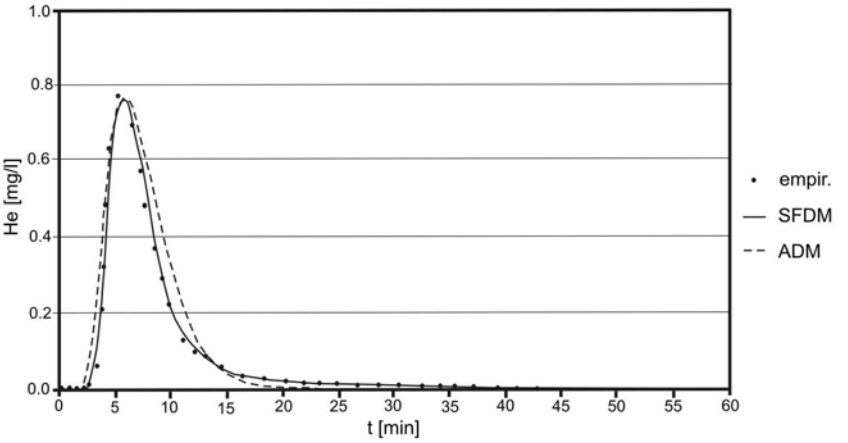

Fig. 5.45. Experimental tracer-breakthrough curve (B31 - B1) and adaption by ADM and SFDM with He as tracer gas.

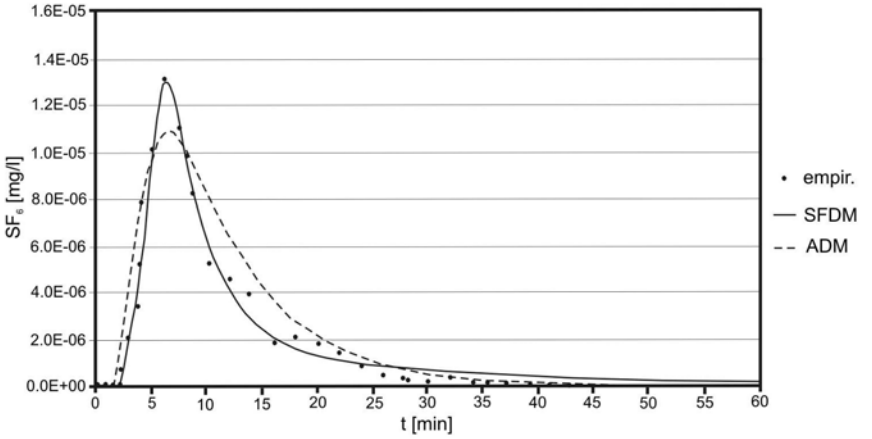

Fig. 5.46. Experimental tracer breakthrough curve (B31 - B1) and adaption by ADM and SFDM with SF_6 as tracer gas.

be interpreted as a proofed sign for diffusive mass transport between fracture and matrix. When discussing the tailing of tracer tests breakthrough curves, investigations by Thüringer (2002) show that also differential advection processes, caused by the use of different and independent flow channels and the technique of tracer injection play a major role. A tailing in tracer breakthrough curves, caused by mixing effects inside the injection boreholes, can hardly be differed from a tailing, caused by diffusion. According to Lever *et al.* (1985) and Tsang *et al.* (1996) a diffusive tailing for an aquatic one-phase-system can be detected in log-log-presentation of the time-concentration-curve. Here a straight line with a slope of -1.5 should appear. The gas tracer tests, done at the unsaturated test site, meet this criteria only between B31 and B1 (Figs. 5.47 and 5.48). Both using He and SF_6, the decrease of concentration follows a straight line with a slope of -1.5 in log-log-presentation. However the number of experiments conducted is too small to deal this result as a proof for the influence of matrix diffusion.

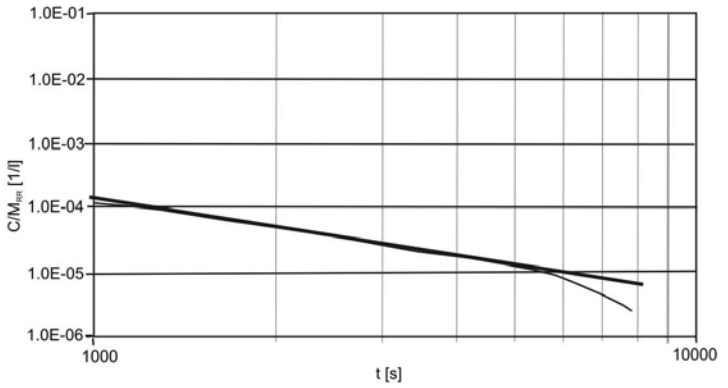

Fig. 5.47. Analysis of tailing behavior with He (B31 - B1), $f(t) = 4t^{-1.5}$.

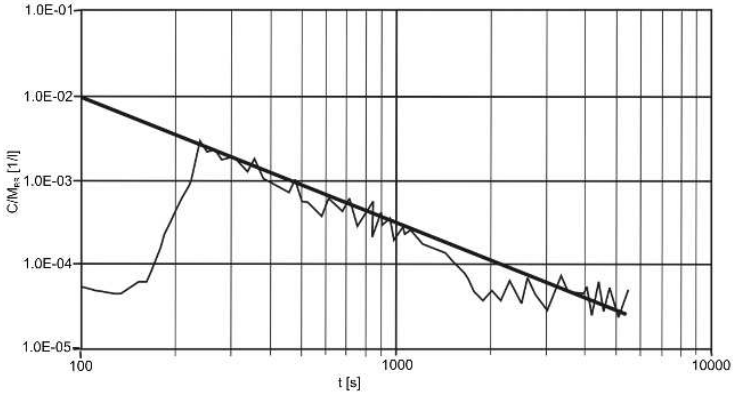

Fig. 5.48. Analysis of tailing behavior with SF_6 (B31 - B1), $f(t) = 10t^{-1.5}$.

5.6.3 Measurements at Central Boreholes

The influence of boundary effects (Sec. 5.9) cannot be neglected at a test site on the field-block scale. After the initial measurements at the marginally installed boreholes (Sec. 5.6.2), experiments were relocated to the central part of the field block. A radial symmetrical arrangement of boreholes (Sec. 5.2.2) ensures that boundary effects are comparable during the experimentation in different directions.

5.6.3.1 Gas-Flow Experiments

In order to quantify the influence of the fracture-system orientation on flow and consequently on solute transport processes within the fractured porous sandstone on the field-block scale, gas flow experiments are applied. A radial symmetrical arrangement of boreholes in the center of the test site with one central borehole and 6 holes in a circle with 2 m radius around it is used. Thus, twelve different flow/transport directions (every 30°) can be reverted to (Fig. 5.50). Every borehole has a diameter of 50 mm and a depth of 1.80 m to 2.20 m through the sandstone bed into the underlying silt and clay.

Pressure gradients are set up between two boreholes of the otherwise completely sealed test block and the air-flow rates measured from hole to hole. In this way, altogether 42 different borehole-to-borehole connections are tested and every direction is represented by three to five different borehole-borehole connections. Without the use of packer systems, the entire thickness of the fractured sandstone is accessible to setup a flow field between the two boreholes.

Every experimental leg is run with gradually increasing and decreasing pressure gradients. A particular air flow rate can be assigned to every pressure gradient (Fig. 5.49). The mean proportion of flow rate and pressure gradient provides information about conductivity with respect to gas flow for every borehole-to-borehole flow path. Figure 5.49 exemplifies this proportion of flow rate and pressure difference using borehole Z3 as the extraction hole.

As is typical of heterogeneous fractured systems, great differences can be detected among the flow rates per pressure gradient when changing the experimental leg. Besides, the relation between flow and pressure gradient is not linear very often. Initially, a slightly decreasing flow-rate change per change of pressure $\frac{\partial Q}{\partial \Delta P}$ can be observed. But when a certain threshold pressure is exceeded, an excursive increase of flow per pressure gradient occurs in some cases. This phenomenon can be interpreted by the sudden opening of numerous flow paths with rather small cross sectional area, beyond a certain pressure gradient.

In order to correlate relative flow rates to the fracture orientation, the mean values of flow per pressure gradient are determined for every flow

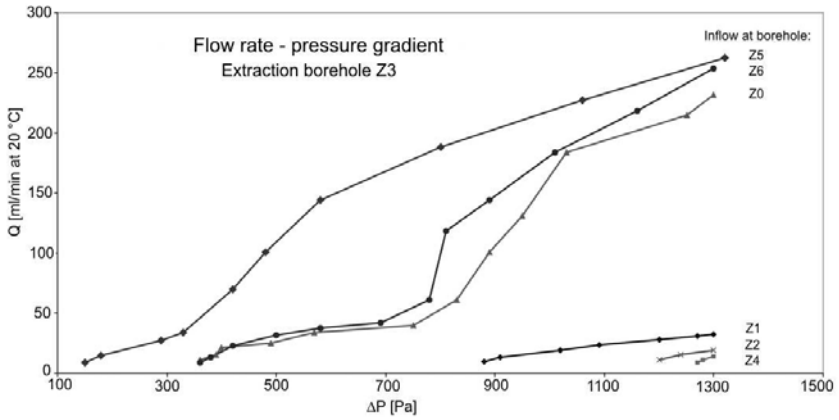

Fig. 5.49. Proportion of air-flow rates and pressure gradients at extraction hole Z3.

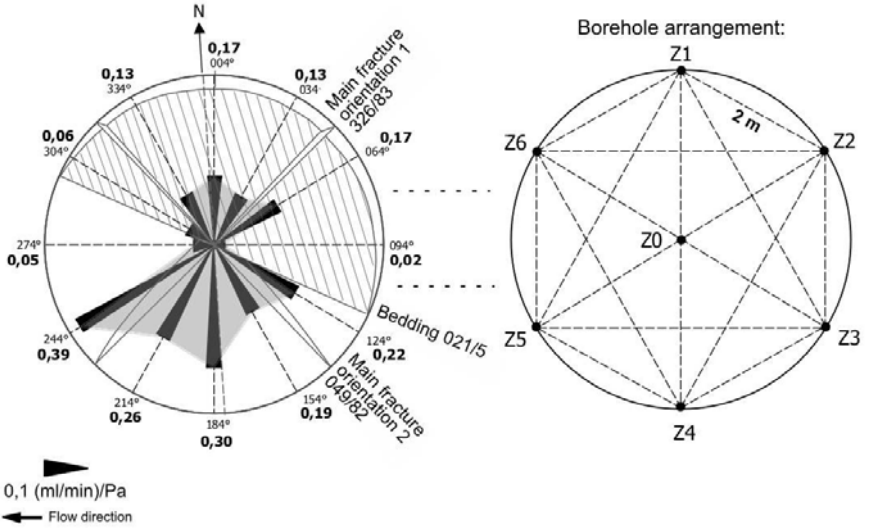

Fig. 5.50. Mean flow rates per pressure gradient [(ml/min)/Pa] (left) for twelve different flow directions (right) compared to the three main discontinuity plains at test site *Pliezhausen*.

direction. Twelve mean proportions of flow rates and applied pressure gradients can be measured, corresponding to the twelve different borehole to borehole connections. The ratios of flow rate per pressure gradient and the three main fracture plains are illustrated in Fig. 5.50.

It is obvious that a direct correlation between flow rates and main fracture plains is not possible. On the one hand, the fractures striking south-west - north-east are well defined at high flow rates in the direction 244° or 64°. On the other hand, there is a high conductivity in the north-south direction at borehole Z0, which has an effect on the mean value of the north-south conductivity of all other boreholes. In order to clarify the influence of discontinuity plains on the gas-flow conductivity, some more detailed investigations are necessary.

5.6.3.2 Dipole Tracer Tests

The borehole annulus in the center of the field block provides the opportunity to apply tracer experiments without the interfering influence of the field-block side walls. With the central borehole (Z0) as the injection or extraction borehole, twelve experiments in six different transport directions are possible. The length of each experimental leg is 2 m. The radial symmetrical arrangement of boreholes allows a direct comparison of the tracer experiments to each other and to the results of the flow experiments (Sec. 5.6.3.1). Furthermore, the influence of the relative orientation of the transport direction to the statistically analyzed fracture system can be assessed.

Experimental Set-Up

In contrast to the tracer tests applied to the field block at the marginal boreholes, the tracer experiments on the central boreholes are carried out exclusively in dipole arrangement. An active extraction from the extraction borehole is used together with an active injection of air into the injection borehole. The rate of extraction is chosen to be the same as the rate of injection during these experiments. In this way, a more uniform flow field can be generated using smaller pressure gradients than during the monopole set-up. This is advantageous with respect to gas compressibility.

For the extraction, the same technical set-up is used as that applied during the monopole tests (Fig. 5.41). A constant air flow of 17 l/min is extracted from the extraction borehole using a side channel compressor. The pressure inside the extraction borehole is monitored and the point at which steady-state conditions are achieved is ascertained. The injection occurs by means of a second compressor, which injects a constant air flow of 17 l/min into the field block. The pressure should be monitored in this borehole in order to make out steady state conditions and to avoid an intensive compression of the gases.

In analogy to the monopole tracer tests, helium is used as the tracer gas. The detection occurs directly from the extracted air by a portable mass spectrometer with a measuring range up to 65 000 ppm and an accuracy of 2 ppm. In contrast to the pressureless tracer injection, as applied by Thüringer (2002), the helium is injected in these experiments as an impulse of 30 s by a three-way valve directly into the injection borehole, with a slight overpressure.

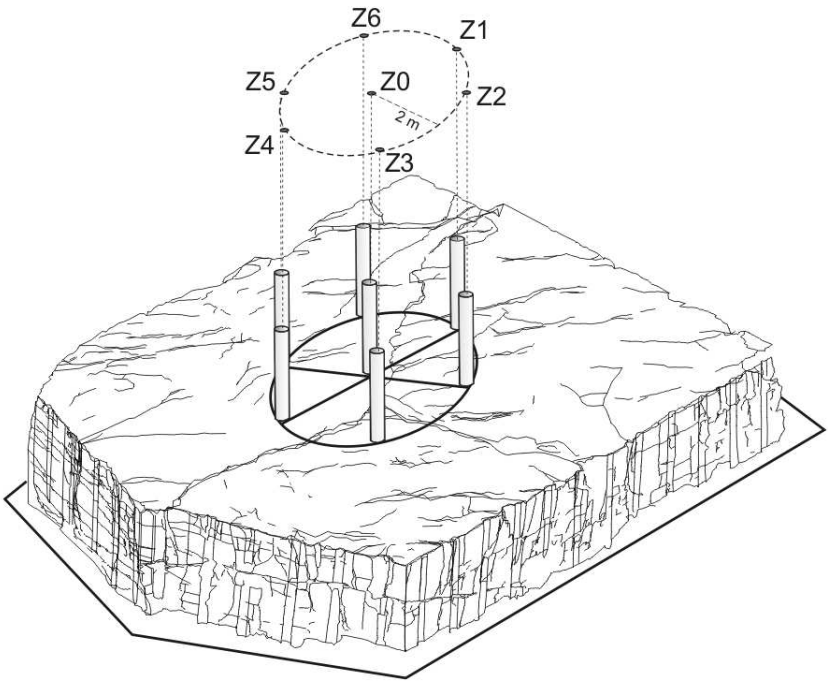

Fig. 5.51. Radial symmetrical borehole annulus in the center of the field block (borehole diameter: 50 mm, borehole depth: 1.80 - 2.20 m, distance between two neighboring boreholes: 2 m).

Thus, an exactly defined mass of helium is introduced into the system, leading to a good reproducibility of the experimental results. To evaluate the injected tracer mass, a gas-volume flow meter is used, which has been calibrated in the run-up by an electronic helium-mass flow meter. During every dipole tracer test, 39.7 mg helium are injected into the field block. Due to the small injected volume of only 0.22 l helium (20°C and 1.0 bar), the temporary disturbance of the steady flow field, caused by the injection at slight overpressure, can be neglected.

Transport to the Central Borehole

In an initial experimental campaign, the tracer transport from the six annulus boreholes (Z1-Z6) to the borehole in the center of the field block (Z0) is investigated. Figure 5.52 illustrates the time-dependent tracer concentration measured in extraction borehole Z0. The helium concentration is displayed in parts per million, in correlation to the experimental time in seconds. All

the concentration and time axes of the diagrams are scaled in the same way to facilitate a direct comparison.

It is obvious that significantly different breakthrough curves are recorded during the six transport experiments. Both, single peaks (e.g. Z6Z0) of different spreading and multiple peaks (e.g. Z5Z0) are recorded with different peak concentrations, ranging from 170 ppm to 750 ppm, with recovery rates from about 14 % to 31 %. The registered times of the first arrival of the tracer

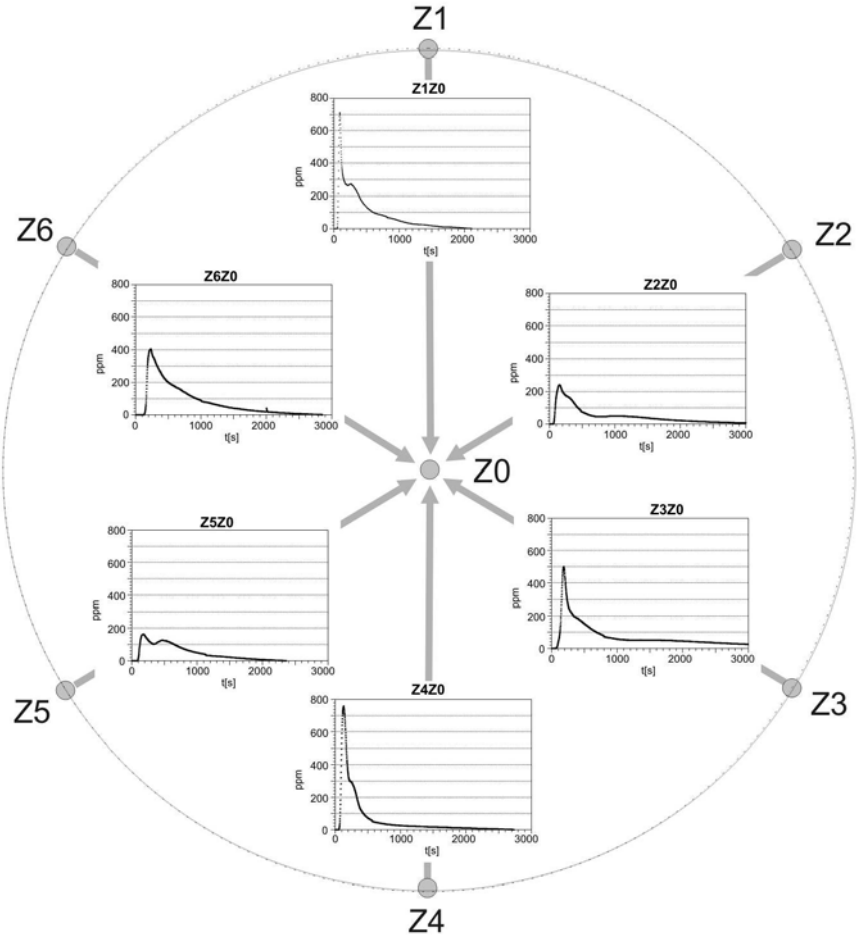

Fig. 5.52. Tracer-breakthrough curves of six helium tracer tests with Z0 as extraction borehole. Distance between two neighboring boreholes: 2 m.

in the central borehole vary from 53 s (injection hole Z1) to 132 s (injection hole Z6).

A comparison of tracer breakthrough curves of the experimental legs lying on a line show noticeable similarities. The breakthrough curves of the injection boreholes Z6 and Z3, Z1 and Z4, as well as Z5 and Z2 represent pairs of curves with comparable maximum concentration, peak number, and peak spreading. Each of the three main directions of the diagonals seems to be characterized by a certain curve shape.

Inversion of Transport Directions and Discussion of Curve Shapes

In a second experimental series, the transport direction on every transportation leg is inverted. Flow field and tracer are now injected at the central borehole (Z0) and extracted successively at one of the six surrounding boreholes (Z1 to Z6). Within these experiments, only five breakthrough curves can be measured and analyzed. Without a stronger side channel compressor and without a significantly lower pressure within the extraction hole, it is impossible to extract a constant air flow of 17 l/min at borehole Z2. Thus, Z2 seems to be only poorly connected to Z0.

When Figs. 5.52 and 5.53 are compared it becomes evident that the inversion of the transport direction between two boreholes only leads to a inconsiderable change in the shape of the breakthrough curves. The shapes, defined by maximum concentration, time of first arrival, peak spreading, and the time for the complete tracer transit, also fit into the shape scheme of the tracer tests to the central borehole.

All the breakthrough curves, measured on the Z1-Z0-Z4 leg feature the earliest times of first arrival of less than one minute, the highest maximum concentration of approximately 700 ppm to 800 ppm, and a sharply defined, dominating concentration peak with a noticeable shoulder or a weakly developed second peak at about 300 ppm. The transport process on this leg seems to be the most significantly fracture-dominated transport mechanism of all these tracer tests. Apparently, there are two independent flow paths with varying participation of the different transport processes. The measurements on the Z6-Z0-Z3 leg feature one dominating concentration peak as well. But this one shows a significantly stronger spreading and tailing and a lower maximum concentration of about 400 ppm to 600 ppm. The time for the complete tracer transit on leg Z3-Z0 is 4800 s and thus more than twice the time for the tracer transit from Z1 to Z0 (2100 s). These breakthrough curves also seem to reflect the coaction of several, variably characterized flow paths. One relatively sharply defined peak is followed by a widely spread tailing, with the decreasing concentration staying on one level over several minutes. At this point, the influence of sparsely dominating auxiliary fractures and the sandstone matrix with its porosity of 20 % (Vol.) defines the shape of the breakthrough curve. The breakthrough curves between Z5 and Z2 indicate an interaction of several, partly poorly conductive small fractures and

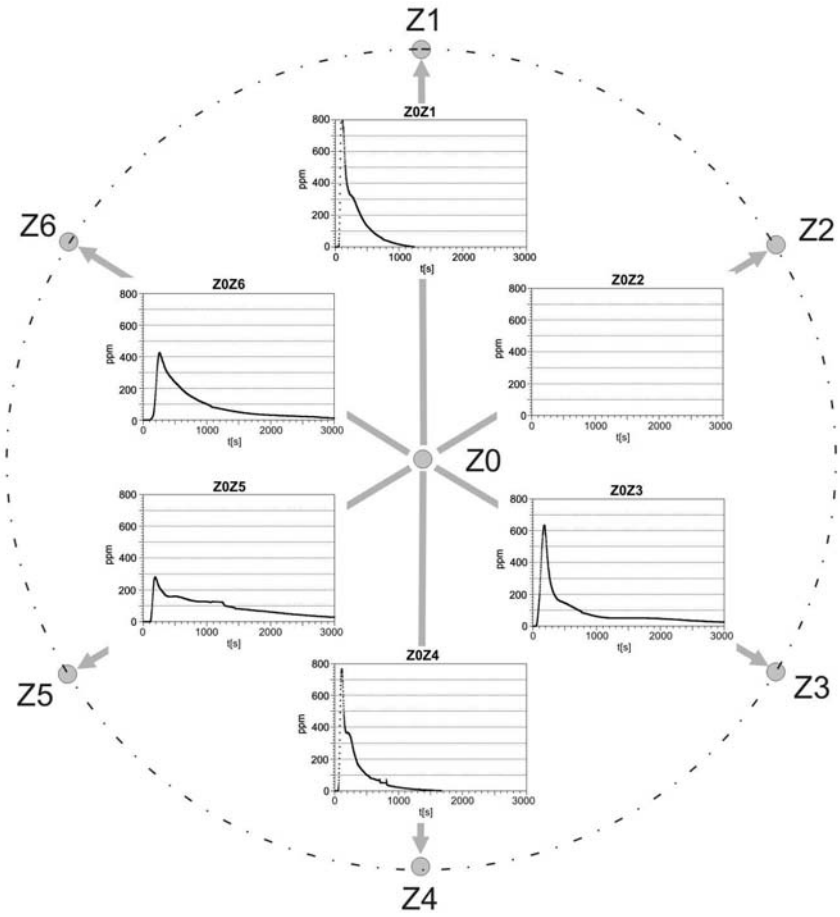

Fig. 5.53. Tracer-breakthrough curves of helium tracer tests with Z0 as injection borehole. Distance between two neighboring boreholes: 2 m.

a probably substantial participation of the highly porous sandstone matrix in the transport process. The measured peaks are significantly spread and show maximum concentrations of only 200 ppm to 300 ppm. Interestingly, however, the first arrival of Z2-Z0 is only inconsiderably later than the first arrival of the mainly fracture-dominated Z1-Z0 leg. Thus, the permeability of at least one of the involved flow paths cannot be considerably lower than that of the dominating main fracture of the Z1-Z0 leg.

Transport Direction and Fracture System

A correlation of the twelve tracer tests described here with the statistically determined fracture system is hardly possible. The significantly dominating

fracture between Z1 and Z4 does not fit into the orthogonal fracture system with fractures striking north-west - south-east and south-west - north-east (Fig. 5.50). The EMR measurements described in Sec. 5.5.2 make this dominating discontinuity plain visible (Fig. 5.39).

The results of the flow experiments, conducted at the central boreholes, reflect the position of this fracture roughly. In this case, the most dominating conductivities around borehole Z0 are measured along the north-south direction. Figure 5.51 shows several fractures around the borehole annulus which are oriented in that direction. These fractures do not play a role in the fracture statistics of the whole field block, but they have great influence on the measured transport processes around the central borehole Z0. They mainly cause an early time of first arrival, a high maximum concentration, a quick concentration declension, and a short tailing in tracer tests in north-south or south-north direction.

5.6.4 Conclusions

In a sandstone quarry in Southern Germany, the sealed in-situ hardrock test site *Pliezhausen* is setup, where experiments to evaluate flow and transport parameters of fractured porous media are applied on the field scale. With different experimental set-ups as well as different tracers, the influence of changing boundary conditions and tracer-specific characteristics can be investigated.

The field and laboratory tests, described in this chapter, show that a basic characterization of transport parameters of an unsaturated porous fractured hard rock is possible by using the following techniques in combination:

- statistical evaluation of fracture parameters (orientation, length distribution and distance distribution),
- multidirectional gas tracer tests with He and SF_6,
- analysis of porosity, permeability and fracture-fillings in core samples,
- electro-magnetic-reflection measuring in different orientations.

Within the air-saturated (water-unsaturated) hard-rock system, two different tracer gases were used. Helium is significantly lighter than air, and could be called "floater" in analogy to an aquatic system. The other tracer gas is sulfur hexafluoride, which is heavier than air and could be called "sinker". An exact evaluation of the analogue potential in terms of investigation of pollutant transport of floating and sinking hydrocarbons seems to be profitable. The significant temperature-dependence of physical and chemical gas parameters can be used for worst-case studies on transport parameters. Gas-tracer tests conducted at the frozen test site in winter make the evaluation of transport parameters at extremely reduced retardation potentials (diffusion and gas solution) possible. Such investigations are hardly applicable to a saturated system. The unsaturated in-situ hard-rock test site *Pliezhausen* offers

the opportunity to carry out basic research on flow and transport processes in fractured porous media.

5.7 Application of the Discrete Model on the Field-Block Scale

A. Silberhorn-Hemminger, R. Helmig

The investigation of flow and transport processes on the field-block scale using the discrete modeling approach (Sect. 2.4) has the aim of improving the understanding of flow and transport processes occurring in complex fractured porous media. The aim is to achieve the best possible agreement between measured and simulated flow and transport results; bearing in mind that the various processes and geometries have a significat influence on the results. Here, the characteristics of the results rather than exact fit is essential. Figure 5.54 shows the surface of the field block. The fracture traces along the side walls and the top of the field block are clearly seen. First, a three-dimensional deterministic fracture model for the south-east/east area of the field block is developed and presented in Sect. 5.7.1. In Sect. 5.7.2, the flow and transport processes are investigated using a two-dimensional model of the vertical plane between two vertical boreholes. In order to include the outer boundaries of the field block and the surrounding area, an extended two-dimensional model is presented in Sect. 5.7.3. The simulated and the experimental results are compared in Sect. 5.7.4.

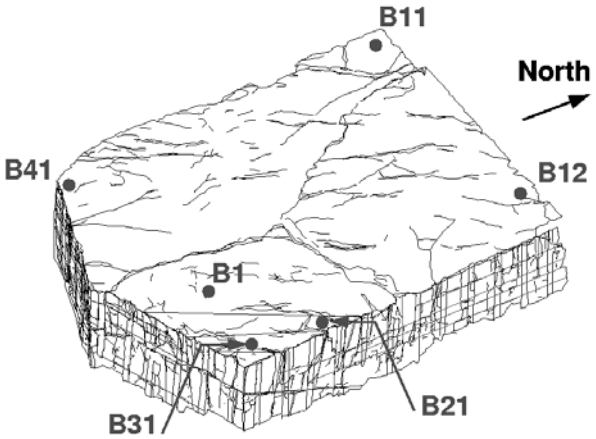

Fig. 5.54. View of the field block from the south-east. Mapping of the fracture traces on the side walls and approximation of the fracture traces.

5.7.1 Deterministic Fracture Model for the South-east/East Area and Boundary Conditions

First, a three-dimensional deterministic fracture model for the south-east/east area of the field block is developed. The relevant and significant fractures on the surface are detected by using stereo-photogrammetric plots (Sect. 5.3.1) and photos of the side walls and of the top. The detected fractures can be seen in Fig. 5.55 a)–c). In order to obtain a three-dimensional fracture model, the fracture traces detected on the different side walls and the top must be linked. The fracture traces of the three vertical fracture planes V1, V2, and V3 are visible on the two side walls (south-east and east wall) and on the top. Hence, the position and extension of the three vertical planes are well known.

However, the detection of the horizontal fracture planes, which are visible on the eastern side wall, are more difficult. The horizontally dominated structure elements represent the boundaries of different geological layers. These boundary layers have a dip to the north-east with an angle of 5°- 10° (Sect. 5.3.1). A first assumption is that the horizontal boundary layers, later called the horizontal fracture planes, extend almost horizontally through the complete field block. On the Basis of the detected vertical and horizontal fracture planes, a three-dimensional deterministic fracture model for the south-east/east corner of the field block is developed. Figure 5.55d) shows the fracture model.

In order to obtain a better understanding of the highly complex flow and transport processes within the field block, the model domain with its material properties, the geological structure and the boundary conditions reduced to a simple but still realistic model. The model is used as a *learning model*, which supports the analysis of the complex process behavior. Therefore, a two-dimensional plane which is located between boreholes B21 and B31 is extracted from the three-dimensional fracture-network model. The boundary conditions around this two-dimensional plane between boreholes B21 and B31 and around the field block are shown in Fig. 5.56. The field block sits on a sandy clay silt layer. There is atmospheric pressure along the outer surface of the silt layer. The whole surface of the field block is sealed. As described in Sect. 5.2.2, the surface can be regarded as almost impermeable. There is a direct contact area between the field block and the sandy clay silt layer along the layer boundary.

5.7.2 Two-Dimensional Case Study: Simulation 1

Tracer measurements between boreholes B21 and B31 show that the injection rate is significantly smaller than the extraction rate (Sect. 5.6.1). Two possible reasons are given: first, in addition to the injection borehole, there could be another inflow area which leads to the large difference between the controlled inflow and outflow rates. Because of the sealed surface of the field

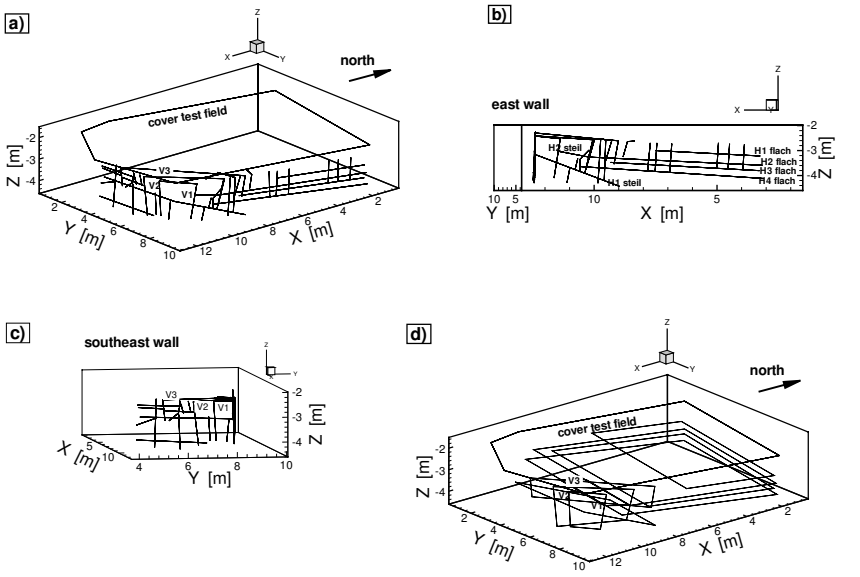

Fig. 5.55. Detected fracture traces (a–c) and the developed three-dimensional deterministic fracture model (d).

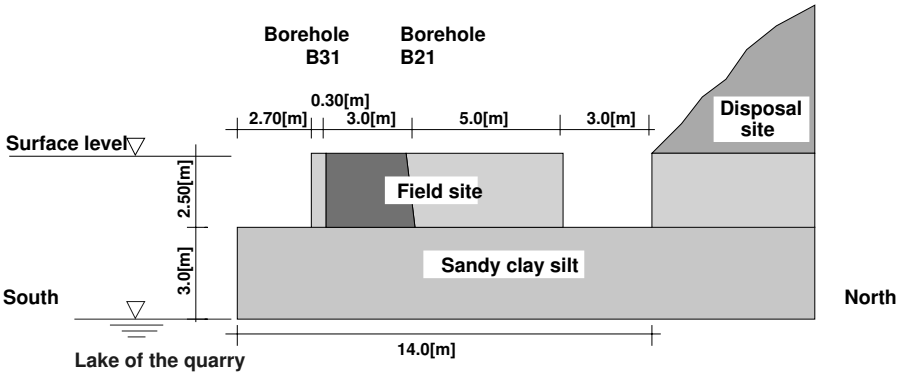

Fig. 5.56. Vertical section of the field block from north to south (year 2000).

block, an additional inflow area must be located at the bottom of the field block. Second, the in- and the outflow discharges can vary due to the compressibility of the gas. Since the imposed pressure ratio between the in- and the outflow boreholes is small (≈ 1.005), the first reason is considered to be the more realistic explanation.

In the first simulation, the additional inflow along the boundary between the field block and the silt layer is taken into account using a pressure boundary condition at the bottom of the simulation domain (see Fig. 5.57). For the two-dimensional fracture matrix model (Fig. 5.58, left), which is extracted from the three-dimensional fracture-network model, one receives only a very small inflow rate along the bottom boundary ($Q_{\text{in,bottom}} = 0.02\% \cdot Q_{\text{out}}$). Because there is no direct connection between the highly permeable fracture network system and the bottom boundary of the simulation domain, representing the boundary to the silt layer, the inflow rate along the bottom boundary is very small.

From the evaluation of the field-block surfaces, information about the statistical distribution of the fractures is available (Section 5.3.1). This additional

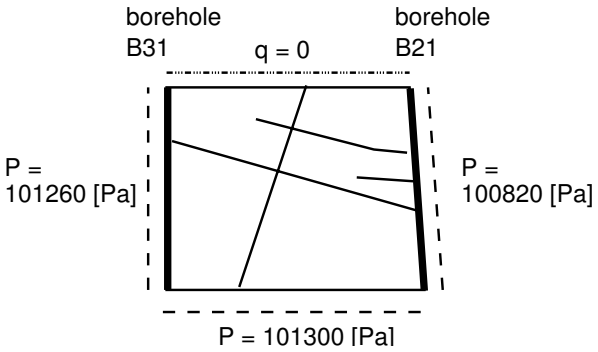

Fig. 5.57. Simulation domain 1: boundary conditions.

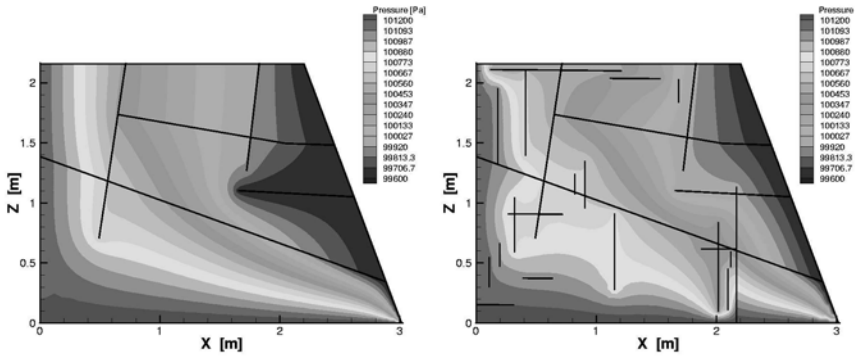

Fig. 5.58. Simulation domain 1, pressure distribution. Left: deterministic fracture network. Right: combination of deterministic and stochastic fracture network.

data is used to generate a stochastic fracture network that is combined with the deterministically detected fractures. The purpose of including the statistical information is to achieve a more realistic model of the actual fracture network. The extracted two-dimensional simulation domain of the fracture matrix system and the pressure distribution are shown in Fig. 5.58, right. There is one fracture which connects the bottom boundary with the highly permeable fracture network. With regard to the inflow and outflow rates, the influence of this fracture is very clear: 68% of the extraction rate Q_{out} flows along the outer boundary into the simulation domain. The simulations lead to the following results:

- There is a significant inflow into the investigation domain along the boundary layer field block / silt layer.
- A purely matrix-dominated connection between the field block and the silt layer does not cause the high inflow rates along the bottom boundary. In order to reach this high inflow rate, the field block and the silt layer must be connected directly by highly permeable fractures.
- The atmospheric-pressure boundary condition along the bottom boundary has the effect of a worst-case condition. However, the simple model clearly shows the relation between the influence of the bottom boundary and the fracture network.

5.7.3 Two-Dimensional Case Study: Simulation 2

In order to obtain a more realistic model, the above model is modified. The sandy clay silt layer is included into the model domain and the deterministic three-dimensional fracture network is updated using more detailed data of the field block and the boreholes themselves. The vertically dominated fractures reach the silt layer. Figure 5.59, left, shows the modified simulation domain and the chosen boundary conditions. To the right, the notation of the fractures as used in Table 5.9 is presented.

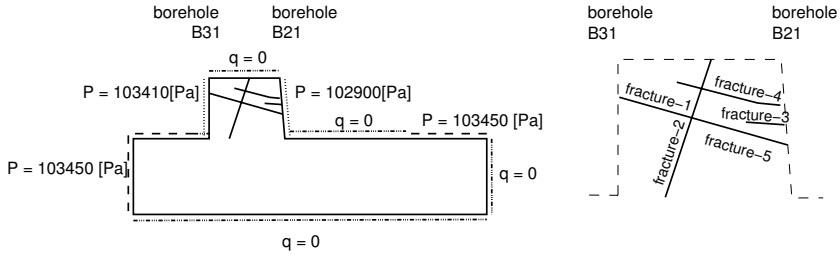

Fig. 5.59. Extended simulation domain. Left: boundary conditions following the selected experiment. Right: notation of the fractures.

5.7.3.1 Flow Simulation

First, the flow model and the experimental results of the selected measurement must correspond. Therefore, the model parameters matrix permeability, permeability of the silt layer, and fracture apertures are varied. Table 5.9 presents the variations of the model parameters and the inflow and outflow rates obtained.

Table 5.9. Variation and calibration of the flow parameters. If no parameter is given, the parameter is the same as in the previous column.

	run01a	run01b	run01c	run01d	run01e	run01f	run01g
Permeability (m^2)							
Matrix	$2.26{\cdot}10^{-15}$			$5.0{\cdot}10^{-13}$			
Clay silt	$1.33{\cdot}10^{-12}$					$1.0{\cdot}10^{-11}$	$7.07{\cdot}10^{-10}$
Aperture (m)							
fract. 1	0.001	0.002	0.0005		0.00045		0.00047
fract. 2	0.001	0.010			0.015	0.02	
fract. 3	0.001	0.002			0.005		
fract. 4	0.001	0.002			0.005		
fract. 5	0.001	0.002			0.010	0.02	
Permeability (m^2)							
fract. 1	$8.33{\cdot}10^{-8}$	$3.33{\cdot}10^{-7}$	$2.08{\cdot}10^{-8}$		$1.69{\cdot}10^{-8}$		$1.84{\cdot}10^{-8}$
fract. 2	$8.33{\cdot}10^{-8}$	$8.33{\cdot}10^{-6}$			$1.88{\cdot}10^{-5}$	$3.33{\cdot}10^{-5}$	
fract. 3	$8.33{\cdot}10^{-8}$	$3.33{\cdot}10^{-7}$			$2.08{\cdot}10^{-6}$		
fract. 4	$8.33{\cdot}10^{-8}$	$3.33{\cdot}10^{-7}$			$2.08{\cdot}10^{-6}$		
fract. 5	$8.33{\cdot}10^{-8}$	$3.33{\cdot}10^{-7}$			$8.3{\cdot}10^{-6}$	$3.33{\cdot}10^{-5}$	
Q_{in} ($m^3\,s^{-1}$)							
Meas. Qin=$1.83{\cdot}10^{-5}$ ($m^3\,s^{-1}$) (at B31)							
Sim.	$1.15{\cdot}10^{-4}$	$9.90{\cdot}10^{-4}$	$2.25{\cdot}10^{-5}$	$2.26{\cdot}10^{-5}$	$1.67{\cdot}10^{-5}$	$1.67{\cdot}10^{-5}$	$1.90{\cdot}10^{-5}$
Q_{out} ($m^3\,s^{-1}$)							
Meas. $Q_{out} = 9.24{\cdot}10^{-4}$ ($m^3\,s^{-1}$) (at B21)							
Sim.	$1.15{\cdot}10^{-4}$	$9.91{\cdot}10^{-4}$	$2.43{\cdot}10^{-5}$	$2.96{\cdot}10^{-5}$	$2.37{\cdot}10^{-5}$	$3.68{\cdot}10^{-5}$	$9.32{\cdot}10^{-4}$

A comparison of case *run01a* and case *run01b* shows that the larger fracture aperture of case *run01b* leads to a significant higher flow rate. The simulated outflow rate is similar to the experimental outflow rate. However, the simulated inflow rate along borehole B31 is too high. In a next step, the fracture between boreholes B21 and B31 is divided in two fracture segments (*fracture-1* and *fracture-5*) with different material properties (see Fig. 5.59). A very small aperture for *fracture-1* minimizes the inflow rate along bore-

hole B31 (see case *run01c*). But the small outflow rate obtained is not desired. As shown in case *run01d*, the fracture network dominates the flow rates strongly, while the sandstone matrix contributes only to very small changes of the flow rates. The chosen permeability of the sandstone matrix $k_M = 5.0 \cdot 10^{-13}\,\mathrm{m}^2$ represents an effective permeability. The effective permeability combines the sandstone matrix and additional fractures which are not included in the pure fracture network.

The experimental measurements and the simulation results presented in Sect. 5.7.2 show that the main inflow into the investigation domain occurs along the boundary layer field block / silt layer. To represent this behavior in the model, a larger aperture of the vertical fracture *fracture-2* is chosen (see case *run01b*, *run01e*, *run01f*). Additionally, a larger permeability for the silt layer is chosen (case *run01f*). The inflow and outflow rates obtained are very close to the measured rates. The flow parameters of case *run01f* are the basis of the following transport simulations.

Figure 5.60 shows the pressure distribution for the flow simulation of case *run01a* and *run01f*. Comparing the two cases, one notices the larger reduction of the pressure along the silt layer as well as along the vertical fracture *fracture-2* in case *run01f*. This larger reduction in case *run01f* is based on the higher permeability of the silt layer, the larger aperture of the vertical fracture *fracture-2*, and the very small aperture of fracture *fracture-1* in case *run01f*.

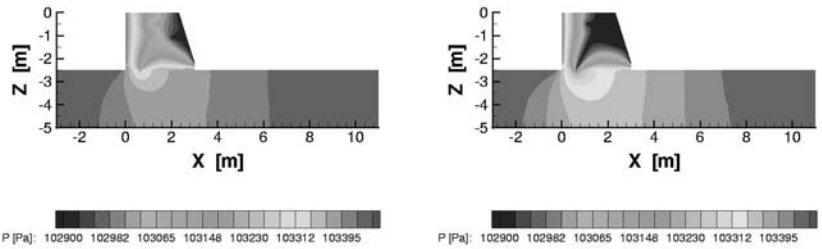

Fig. 5.60. Pressure distribution: case *run01a* and *run01f*.

5.7.3.2 Transport Simulation

The following boundary conditions are chosen for the transport simulations. At the injection borehole, a constant concentration $c/c_o = 1.0$ is injected over

an injection time of $t_{in} = 60$ s. At the extraction borehole, a free-flow boundary is defined. Figure 5.63 shows the tracer-breakthrough curves for the various transport simulations presented in Table 5.10. If no parameter is given, the parameter is the same as the previous column. The right plot of Fig. 5.63 does not include the results of case *run03*. Furthermore, the scale of the y-axis is different from the left plot.

Table 5.10. Variation of the transport parameters.

	run01	run02	run03	run04	run05	run06
Porosity (-)						
Matrix	0.30					
Silt	0.30					
Fractures 1 - 5	0.30			0.40	0.30	
Dispersivity (m)						
Matrix longitudinal	0.002	0.01	0.001		0.01	
Matrix transversal	0.002	0.01	0.001		0.01	
Fractures 1 - 5	0.001				0.01	0.01
Molecular						
Diffusion ($m^2\,s^{-1}$)	$6.12{\cdot}10^{-5}$		0.0	$6.12{\cdot}10^{-5}$	0.0	$6.12{\cdot}10^{-5}$

The concentration distributions for the two simulations case *run01* and case *run03* are shown in Figs. 5.61 and 5.62 for three time steps. Note that Figs. 5.61 and 5.62 show only the area of the field block and not the complete simulation domain. The simulation results of case *run01* (Fig. 5.61) show that the fractures still dominate the transport, but the matrix has an additional important influence. Tracer infiltrates into the matrix and flows slowly towards the fracture network. The main tracer transport occurs in the fracture-network system.

The transport behavior in case *run03* (Fig. 5.62) is characterized by a small hydrodynamic dispersion which leads to an advectively dominated transport. As can be seen in Fig. 5.62, tracer mainly flows through the fracture network ($t = 60$ s, $t = 180$ s). At the intersection point of fracture *fracture-1*, *fracture-2*, and *fracture-5*, the tracer concentration is significantly reduced because of the zero concentration in the lower segment of *fracture-2*. After the tracer injection stops, a large amount of tracer remains in the matrix area around *fracture-1*.

All five curves in Fig. 5.63, left, show a very early first arrival time. Curve *run03* ascends very steeply and, after reaching the maximum peak, it descends very fast. A second, much smaller peak indicates a second flow path within the fracture network. This second flow path can be seen clearly in Fig. 5.62 ($t = 180$ s) along *fracture-4*. The advectively dominated transport is due to the small hydrodynamic dispersion: the molecular diffusion is zero and

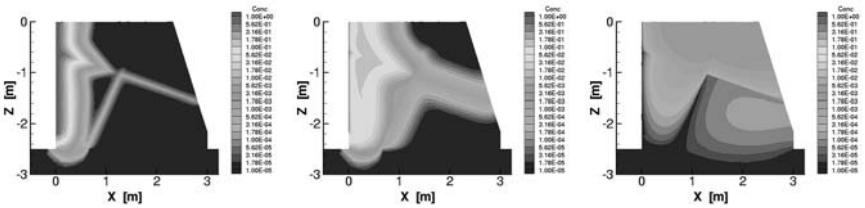

Fig. 5.61. *run01*: concentration c/c_0 after $t = 60\,\text{s}$,$t = 180\,\text{s}$,$t = 3000\,\text{s}$.

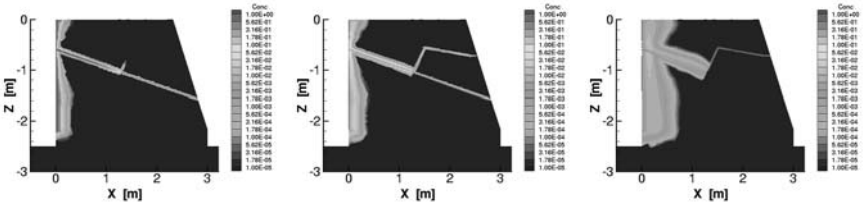

Fig. 5.62. *run03*: concentration c/c_0 after $t = 60\ \text{s}$,$t = 180\,\text{s}$,$t = 3000\,\text{s}$.

the dispersivity of the fractures and the sandstone matrix is very small. The breakthrough curves of the simulations *run01*, *run02*, *run04*, and *run05* (see also Fig. 5.63, right) are very similar. They ascend steeply as well. However, the maximum peak is smaller than in case *run03*. The observed tailing indicates that the influence of the matrix is not negligible. Curve *run05* reaches a higher maximum than curves *run01*, *run02*, and *run04*. As in case *run03*, the molecular diffusion is zero, but the high dispersion of case *run05* prevents the development of a strong advectively dominated transport process.

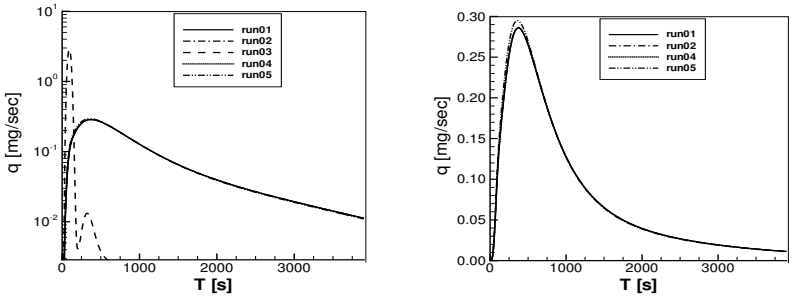

Fig. 5.63. Breakthrough curves for simulations listed in Table 5.10. Left: *run 01 – 05*, logarithmic tracer mass flux scale. Only *run03* differs from the other curves. Right: *run 01, 02, 04, 05*, linear tracer mass flux scale. All curves are very similar.

5.7.4 Comparing Measured and Numerical Results

Figure 5.64 shows the breakthrough curves of the selected experiment and the results of the simulations *run01*, *run02*, *run04*, and *run05*. It can be observed that the first arrival occurs much earlier for the simulation than for the experiment. Just shortly after the start of the tracer input at the injection boundary, the tracer plume reaches the extraction boundary in the simulations. In contrast, the measured breakthrough curve reaches the extraction borehole after a couple of minutes. The simulated and the measured curves differ in their maximum peak; however, the characteristics (increase, decrease, tailing) are similar. The tailing of the curves indicates the influence of the matrix.

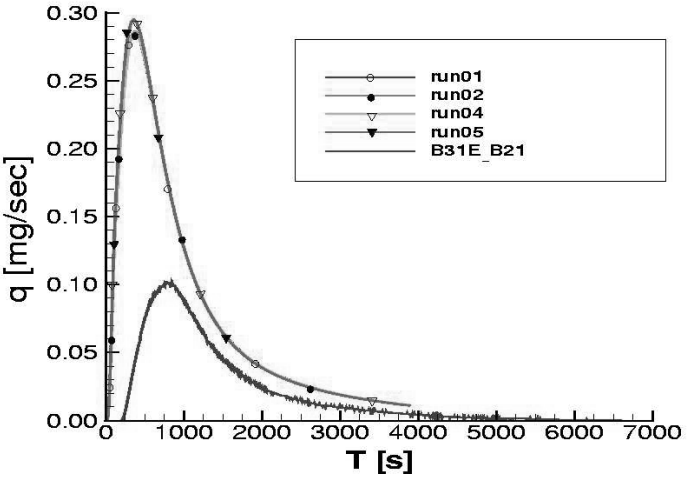

Fig. 5.64. Experimental and simulated breakthrough curves.

When the experimental and the simulated results are compared, it must be kept in mind, that the simulation domain does not represent the natural system of the field block. The simulations are based on a two-dimensional model, which cannot represent the strong three-dimensional flow and transport behavior within a fractured porous aquifer system. The same conclusion is drawn for the cylindrical bench-scale sample (Sect. 4.3.2.2)

The fractures are represented by parallel plates with a constant aperture. However, observations show that the fractures are partly filled with clay or sand. This heterogeneous structure of the fractures probably leads to channeling effects within the fracture planes, which cannot be reproduced by the parallel-plate concept.

Further improvement is expected if the deterministic fracture model is combined with stochastic fracture models which are based on recorded field data. The combined fracture models include more information on the field block than the single deterministic fracture model. Stochastically generated fracture systems are only single realizations of an infinite number of possible realizations. Therefore, the use of stochastic data requires a large number of simulations in order to achieve an average behavior that can be compared to measured data. Since one single measured curve is likely to deviate from the average behavior, several measurements at more that one location are a pre-requisite for achieving useful results.

In Chapt. 10, an approach for characterizing tracer breakthrough curves, measured at different locations within a domain, is presented. This approach is based on the classification of breakthrough curves using multivariate statistical methods. The method is tested on the bench scale, on $60 \times 60 \times 60\,\mathrm{cm}^3$-block which does not contain very significant fractures. It is planned to conduct measurements which would allow this characterization method to be applied to the field block as well. Such multiple measurements would also allow simulations of stochastically generated fractured porous domains to be carried out.

5.8 Integral Transport Behavior on the Field-Block Scale

T. Vogel, D. Jansen, J. Köngeter

In the following study, a hypothetical aquifer system (based on the parameters of the field experiments) is used to present the capabilities of the developed multi-continuum model STRAFE (cf. Sec. 2.5) for three identified hydraulic components. This study is only a conceptual investigation and is used to gain an understanding of the processes.

5.8.1 Model Area and Boundary Conditions

In the study, a simplification of the sandstone block (near Tuebingen, Germany) is used. The horizontal circumference is approx. $10.0\,x\,7.0\,\mathrm{m}^2$, the thickness approx. 2.0 m in the three-dimensional case study. For the one-dimensional case study, a transport distance of 10.0 m is considered.

The boundary conditions for the one-dimensional case study to identify the integral transport behavior are shown in Fig. 5.65. The tracer is infiltrated locally at one point. At the beginning ($t = t_0$), the whole area is free of tracer and the piezometric water level is 3.0 m. The boundary conditions are kept constant during the simulation. A Dirichlet boundary condition is chosen for the transport simulation, with a relative concentration of 1.0 at the inlet. The

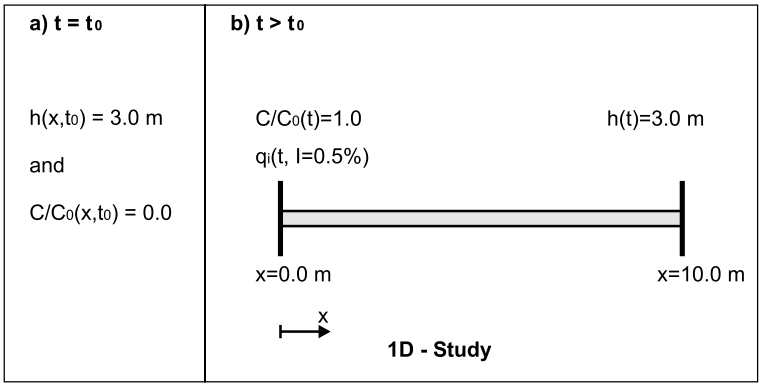

Fig. 5.65. Boundary conditions of the one-dimensional case study.

flow field is stationary, with a hydraulic gradient of 0.5 %. The outlet is on the side opposite to the inlet.

In the three-dimensional case study, a regional flow from one of the smaller face surfaces to the other is considered. The other surfaces are designed to be impermeable. It is very complicated to find an arrangement of integral boundary conditions on the face surfaces for an experiment. For this reason, punctiform boundary conditions are created (cf. Fig. 5.66). For the three-dimensional simulations, the z- and y-dimensions are reduced to half width for reasons of symmetry. This results in a modeling area of $10.0\,x\,3.5\,x\,1.0\,\mathrm{m}^3$. At the beginning ($t = t_0$), the whole area is free of tracer and the piezometric water level is 3.0 m. At the point in time $t > t_0$, the hydraulic gradient between in- and outlet is 0.5 %. The point of the inlet or the outlet is situated at the middle of the respective face surface.

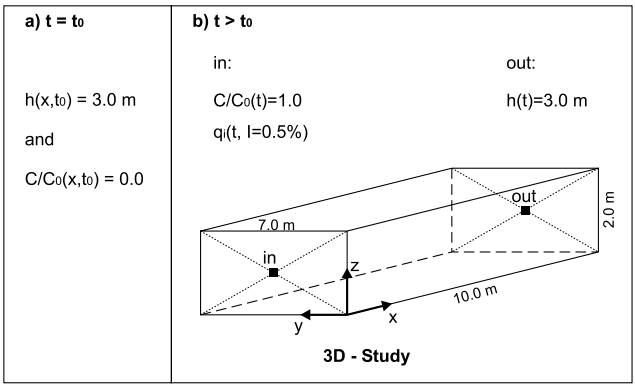

Fig. 5.66. Boundary conditions of the three-dimensional case study.

5.8.2 Aquifer Properties

During the laboratory and field experiments, three hydraulically active components could be identified, including a macro-fracture system, a micro-fracture system and the host matrix. The orientation of the fractures is assumed to be orthogonal, implying that the matrix blocks are rectangular. The equivalent and exchange parameters used for the basic configuration of the multi-continuum model are summarized in Tables 5.11 and 5.12.

Table 5.11. Equivalent parameters for the basic configuration of the multi-continuum model.

Equivalent parameter			Macro (f1)	Micro (f2)	Matrix (m)
Permeability	$\bar{k}$	(m^2)	$5.00 \cdot 10^{-12}$	$5.00 \cdot 10^{-13}$	$5.00 \cdot 10^{-14}$
Specific storativity	$\bar{S}_s$	(m^{-1})	$1.00 \cdot 10^{-5}$	$1.00 \cdot 10^{-5}$	$1.00 \cdot 10^{-5}$
Porosity	$\bar{n}_e$	(-)	$1.00 \cdot 10^{-3}$	$5.00 \cdot 10^{-3}$	$1.00 \cdot 10^{-1}$
Dispersivities:		(m)			
- longitudinal	$\bar{\alpha}_l$		$5.00 \cdot 10^{-2}$	$1.00 \cdot 10^{-1}$	$2.00 \cdot 10^{-1}$
- transversal horizontal	$\bar{\alpha}_{th}$		$5.00 \cdot 10^{-3}$	$1.00 \cdot 10^{-2}$	$2.00 \cdot 10^{-2}$
- transversal vertical	$\bar{\alpha}_{tv}$		$2.00 \cdot 10^{-3}$	$5.00 \cdot 10^{-3}$	$1.00 \cdot 10^{-2}$
Coefficient of Diffusions	$\bar{D}_m$	($m^2 s^{-1}$)	$8.00 \cdot 10^{-10}$	$6.00 \cdot 10^{-10}$	$4.00 \cdot 10^{-10}$
Relative volume	Ω	(-)	1.00	1.00	$9.94 \cdot 10^{-1}$

Table 5.12. Exchange parameters for the basic configuration of the multi-continuum model.

Exchange parameter			Macro / Micro f1f2	Macro / Matrix f1m	Micro / Matrix f2m
Shape of blocks			cube	cube	cube
Penetration depth	$\bar{s}_{max}$	(m)	$5.00 \cdot 10^{-1}$	$5.00 \cdot 10^{-1}$	$2.50 \cdot 10^{-1}$
Specific surface	$\bar{\Omega}_0$	(m^{-1})	6.00	6.00	$1.20 \cdot 10^{+1}$
Specific fracture surface	$\bar{\Omega}_W$	(m^{-1})	2.00	2.00	4.00
Geometric factor	ϵ	(-)	5/3	5/3	5/3
Exchange parameter:					
- flow	$\bar{\alpha}_Q$	(ms^{-1})	$8.33 \cdot 10^{-6}$	$8.33 \cdot 10^{-7}$	$8.33 \cdot 10^{-7}$
- transport	$\bar{\alpha}_c$	($m^2 s^{-1}$)	$5.00 \cdot 10^{-12}$	$6.67 \cdot 10^{-11}$	$6.67 \cdot 10^{-11}$
Interface function	$\bar{A}(s)/\bar{A}_0$	(-)	$1-(2-\sqrt{\bar{s}_{max}})s+(1/\bar{s}^2_{max})s^2$		

For the basic configuration, all components of the system influence the regional transport behavior. In accordance with the conceptual idea of the study homogeneous properties are assumed. A high connectivity is then assumed for the chosen transport parameter.

5.8.3 One-Dimensional Case Study

The results for the basic configuration of the triple-continuum model, compared to the single double-continuum models, are presented in Fig. 5.67. These simulations are performed with a one-dimensional model. The coupling chosen for the basic configuration is the parallel coupling method, i.e. all components are coupled with each other.

In the basic configuration, a consistent temporal development for the transport phenomenon is observed (cf. Fig. 5.67). This development cannot be explained simply with a double-permeability model. The three phases distinguished for the transport behavior are drawn schematically in Fig. 5.67. The breakthrough curve f1f2m (BTC) exhibits a "fast breakthrough" at the beginning, and this phase is defined as phase I.

Within the second phase, which is clearly dominated by the interaction of all components, two subphases can be distinguished (the 1st part and the 2nd part of phase II). When the double-continuum model results are compared with the triple-continuum result, it is evident that there are two significant changes in inclination for the TPTP model. The first change indicates the beginning of phase I, resulting from the interaction of the macro-fracture system with the micro-fracture system (f1f2). The second change in inclination is induced by the interaction of the fracture systems with the matrix, because the point in time corresponds with the point in time for simulation f1f2, where the gradient between the components can no longer be observed.

A comparison of the coupling methods and their influence on the transport behavior is presented in Fig. 5.68. The system reacts differently for the selective coupling method than for a parallel or serial coupling method. This is because of the missing interaction of the micro-fracture system and the host matrix which results in a faster equilibrium in concentration between the macro- and micro-fracture system. This can be observed at the breakthrough curve for the first half of the interaction. The slope of the breakthrough curve for selective coupling is less steep than for serial or parallel coupling within the second half of the interaction phase. This behavior can be explained by the fact that, for these points in time, mass transfer only takes place between the host matrix and the macro-fracture system. This transport mechanism results in a slower regional transport.

5.8.4 Three-Dimensional Case Study

The numerical experiment of the conceptual three-dimensional case study allows an evaluation of the transport behaviour when tracer tests are performed. Because of the isotropic, homogeneous material parameters of the

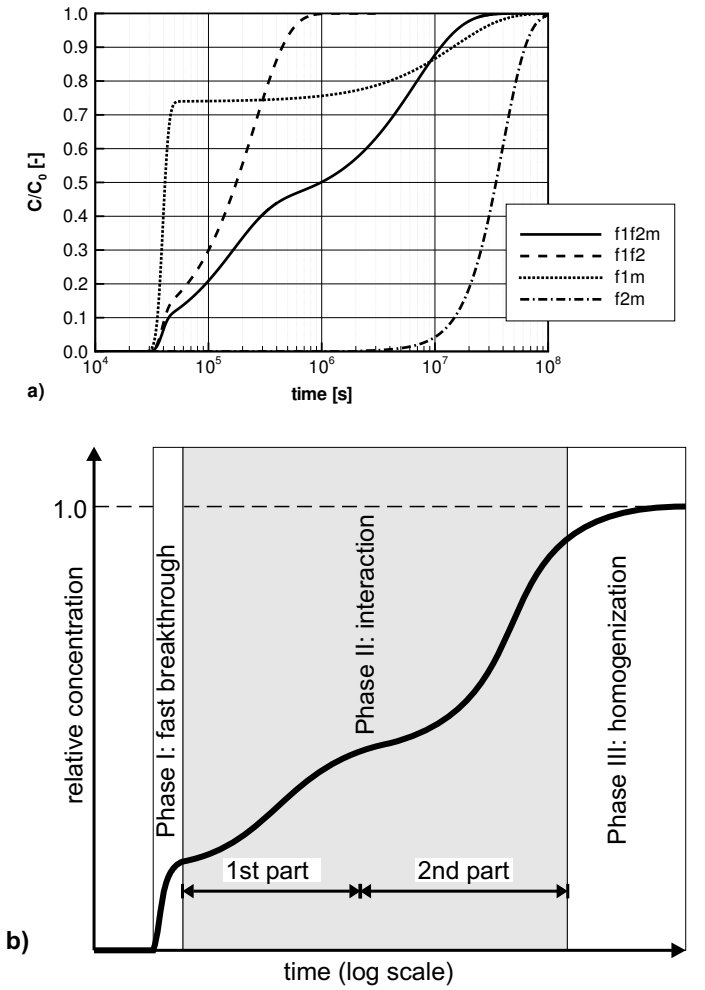

Fig. 5.67. Breakthrough curves for the numerical experiments: (a) comparison of the TPTP model with the different double-continuum models; (b) typing of the integral transport behavior of the TPTP system (Jansen, 1999).

basic configuration and the symmetric boundary conditions (cf. Fig. 5.66), the model area is reduced to a quarter of the original cuboid. The origin of the coordinate system lies at the point of the tracer discharge. The x-axis connects the point of the tracer discharge on the front surface of the cuboid with the measuring point at the back surface. The dimension of the reduced model area is $L_x/L_y/L_z = 10.0/3.5/1.0$ [m].

Figure 5.69 shows the three-dimensional distribution of tracer on the surface of the model area in all components (f1+f2+m) of the multi-continuum

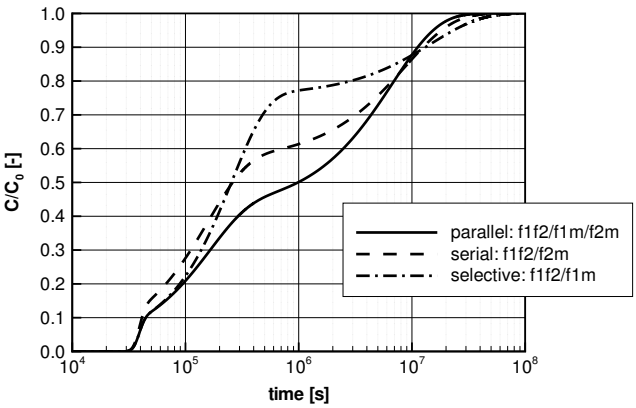

Fig. 5.68. Breakthrough curves for the numerical experiments and a comparison of the coupling models (Jansen, 1999).

system. The distribution is illustrated at the time $t = 2.00 \cdot 10^{+05} s$. This is during the first half of the interaction phase as shown in the one-dimensional case study.

The distribution of tracer in Fig. 5.69 indicates the different transport behaviour of the components. Areas of high tracer concentration are shown in gray, areas of low tracer concentration are displayed in black. At the time of $t = 2.00 \cdot 10^{+5}$ s, almost the whole fracture system is full of tracer. In the micro-fracture system, the tracer resides in an area $x < 0.5$ m whereas, in the matrix, the tracer can be found only near the point of the tracer injection. This means that only the fracture systems account for the transport properties at this early point in time. The comparison of concentration values at a certain point within the domain shows the different transport velocities in the continua.

5.8.4.1 Summary

This conceptual study on the field-block scale, including two hierarchical fracture categories and a host matrix in a triple-continuum model, illustrates a characteristic transport behavior which may not be explained by a homogeneous single- or double-continuum model. The transport behavior is divided into three characteristic phases.

Further investigations are presented by Lagendijk (2003), in which tracer breakthrough curves in fractured porous media are analyzed. A method is developed that allows tracer pulses to be used as boundary conditions with respect to transport and the given signal (breakthrough curve) of the effluent

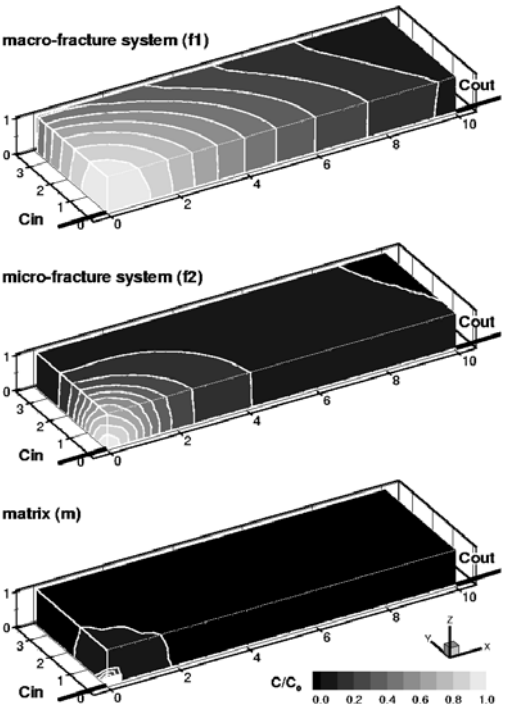

Fig. 5.69. Concentration distributions in the three-dimensional model area; discharge of the tracer in all components occurred at the point in time $t = 2.00 \cdot 10^{+5}$ s.

to be transformed to the signal provided by infinite tracer injection. A variety of studies has been performed for those breakthrough curves and the number of components relevant for flow and transport in fractured porous media identified.

It is proposed that these approaches be applied to experimental data in order to evaluate their capabilities.

5.9 A Study Concerning Boundary Effects on the Field-Block Scale

D. Bachmann, T. Vogel, J. Köngeter

Several boreholes are positioned on the field block (cf. Sect. 5.1) to carry out flow and transport studies. By dint of numerical simulations with the multi-continuum model STRAFE, the extent to which the model boundary affects the shape of the breakthrough curves is analyzed. Because of the fractures in the sandstone block, the flow velocities observed in reality are noticeably larger than those modelled in the context of this study. The influence of the

model boundary should be smaller in reality than predicted by the model. Therefore, the simulations can be regarded as a *worst-case-scenario* study. The simulations are performed by using a homogeneous two-dimensional model composed of two coupled media (cf. Sect. 5.9.1).

First, a preliminary study of the flow is performed to calibrate the model and test the boundary conditions used at the input and output ports. Then, a transport calculation is conducted to determine the boundary effects on the tracer-breakthrough curves.

5.9.1 Model Design

The model of the sandstone block is set up as a two-dimensional model with a two-dimensional subdomain, which represents the layer of poor clay found underneath the sandstone block on the test site. It also allows for the model to take into account all of the leaks of the sandstone block, thus simulating flow rates comparable to the ones observed by tracer tests on the test site (cf. Sect. 9.1.1). Both media are coupled by one-dimensional line elements. Figure 5.70 shows a top view of the model area, the section in the middle representing the field block. The outer boundary defines the model area of the subdomain, which exceeds that of the sandstone block by two meters on all sides, to represent natural conditions better. The inner part of the mesh for the subdomain, however, corresponds to the one for the sandstone block. The two lines crossing each other represent the paths on which the in- and output ports are moved for the flow and transport calculations (cf. Sect. 5.9.3). Figure 5.71 presents a profile of the model, illustrating different configurations of the boundary conditions (cf. Sect. 5.9.3).

The boundary of the sandstone layer is impervious, but the system can aspirate air via the subdomain, where the pressure at the boundary is set to air pressure.

5.9.2 Material Properties

Table 5.13 shows the material properties of the model, those of the fluid (air) and the tracers (helium and SF_6) used for the transport simulations. The orders of magnitude of these parameters are taken from Jaritz (1999) and from Sect. 5.6. The dynamic viscosity η, the density ρ and the diffusion coefficients D_{m} are given at a temperature of 20°C and a pressure of 101.30 kPa. The material properties of the subdomain are the same as those of the sandstone block, except for the permeabilities k_{xx} and k_{yy}, which are the values used for calibration of the model (cf. Sect. 5.9.3).

The effective diffusion coefficient $D_{\mathrm{m,e}}$ in porous media is calculated by means of

$$D_{\mathrm{m,e}} = D_{\mathrm{m}}\omega \,, \tag{5.10}$$

where ω is an empirical coefficient that takes into account the effects of the matrix on diffusion and ranges from 0.01 to 0.50 (Freeze and Cherry, 1979).

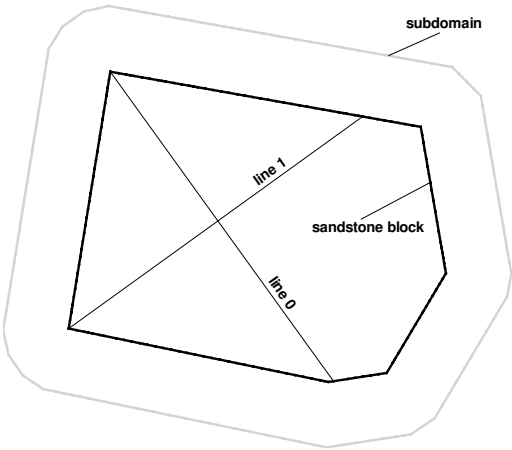

Fig. 5.70. Top view of the model area.

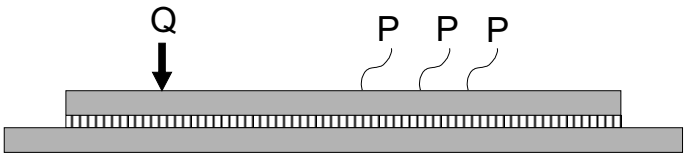

Fig. 5.71. Profile of the model area.

For this study, a value of $\omega = 0.10$ is chosen. The values for the molecular diffusion coefficients D_{m} are taken from Thüringer (2002).

5.9.3 Flow Simulation

The dual-media model is calibrated on the basis of the tracer tests conducted on the sandstone block. The boundary conditions at the input and output are varied between Dirichlet pressure and Neumann flow. Different values for the hydraulic conductivity of the poor clay subdomain are tested.

The variant Neumann - Dirichlet (Q - P) (cf. Fig. 5.71) provides the best results in comparison to the field experiments, so the transport calculation is based on the related boundary conditions. At the output port, a pressure of $p = -420\,\mathrm{Pa}$ is fixed, while the discharge is set to $Q = 1.3 \cdot 10^{-5}\,\mathrm{m^3 s^{-1}}$ at the input port.

Table 5.13. Material properties of the sandstone block, fluid properties and tracer properties.

Material properties of the sandstone block		
n_e	(-)	0.18
k_{xx}	(m^2)	$4.00 \cdot 10^{-14}$
k_{yy}	(m^2)	$4.00 \cdot 10^{-14}$
α_l	(m)	$1.00 \cdot 10^{-2}$
α_t	(m)	$2.00 \cdot 10^{-3}$
Fluid properties		
ρ	($kg\,m^{-3}$)	1.00
μ	($kg\,m^{-1}s^{-1}$)	$1.81 \cdot 10^{-5}$
Tracer properties		
$D_{m,He}$	(m^2s^{-1})	$5.80 \cdot 10^{-6}$
$D_{m,SF6}$	(m^2s^{-1})	$0.83 \cdot 10^{-6}$
ω	(-)	0.10

The value for the permeabilities of the subdomain is set to $k_{xx,sub} = k_{yy,sub} = 10^{-11}\,m^2$. This is a rather high permeability for a clay, but it is in accordance with the observation at the test site that the layer underneath the sandstone block has dried out and as a consequence fractures appeared, increasing the permeability of the clay. Moreover, this permeability value takes into account the leaks of the sandstone block as mentioned above.

The flow calculations are carried out for various distances between the input and output ports (cf. Fig. 5.71). The results are summarized in Table 5.14. When compared to the results of the tracer tests made at the block, they exhibit the same order of magnitude. For a distance of 2 m between the input and output ports, a pressure of -100 Pa and a discharge of $1.3 \cdot 10^{-5}\,m^3s^{-1}$ are measured at the input port, and -420 Pa and $-9.0 \cdot 10^{-4}\,m^3s^{-1}$ at the output port (Hötzl *et al.*, 2000).

Different configurations of the input and output ports are tested. The distance between the ports is varied from 1.00 m to 5.00 m in 1.00 m steps. Furthermore, the ports are moved towards the center of the model area, also in 1.00 m steps, on the crossing lines (cf. Fig. 5.70). The input port at a distance of 1.00 m from the boundary is referred to as *position 1*, the input port at 2.00 m from the boundary as *position 2*, and so on. This is illustrated in Fig. 5.72, which shows the results of the flow simulations for two different configurations: in Fig. 5.72 (a), the input node is in the middle of the model area (*position 7*) while in Fig. 5.72 (b), it is in the upper left-hand corner (*position 1*). In both configurations, the distance between the input and output ports equals 1.00 m. The tracer is injected continuously throughout the whole simulation.

Table 5.14. Results of the flow simulations.

Distance between input and output port (m)	Pressure at the input port (Pa)	Discharge at the output port ($m^3 s^{-1}$)
1	-109	$-9.0 \cdot 10^{-4}$
3	-36	$-8.4 \cdot 10^{-4}$
5	-15	$-7.9 \cdot 10^{-4}$

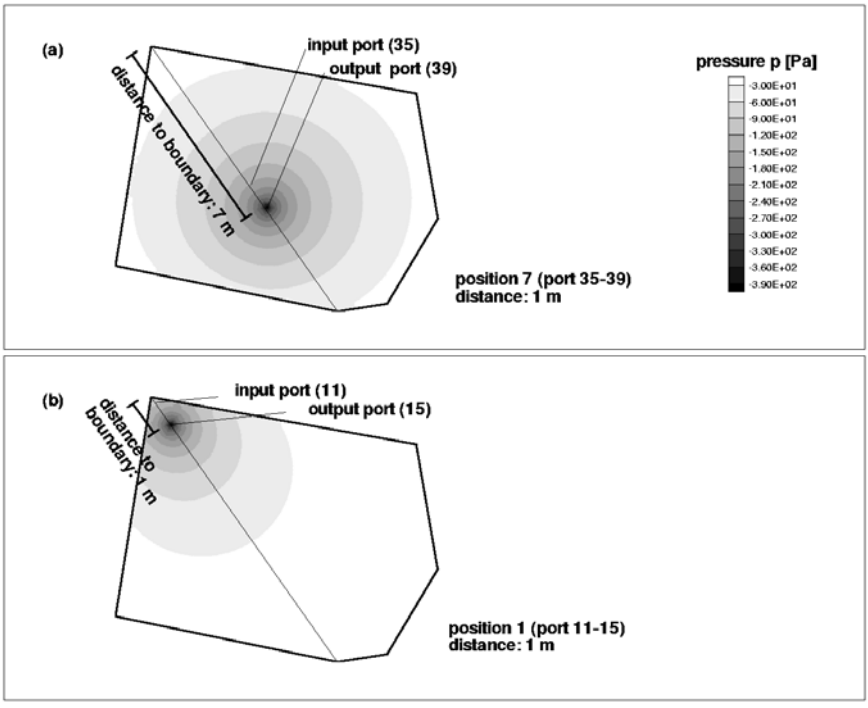

Fig. 5.72. Results of the flow simulation for two different configurations: (a) *position 7*, (b) *position 1*.

5.9.4 Transport Simulation

The results of the transport simulations illustrate the influence of the model boundary on the breakthrough curves. Figure 5.73 presents the breakthrough

curves with helium as the tracer, at a distance of 2.00 m between the input and output ports. It can be observed that moving the ports towards the center of the model area, away from the boundary, evokes correspondingly fewer differences in the breakthrough curves. Thus, the boundary has a significant influence on the shape of the breakthrough curves for configurations close to the boundary. From a certain distance onwards, there is also a noticeable influence on the breakthrough curves, but the shape and tailing of the breakthrough curves are affected in a similar way.

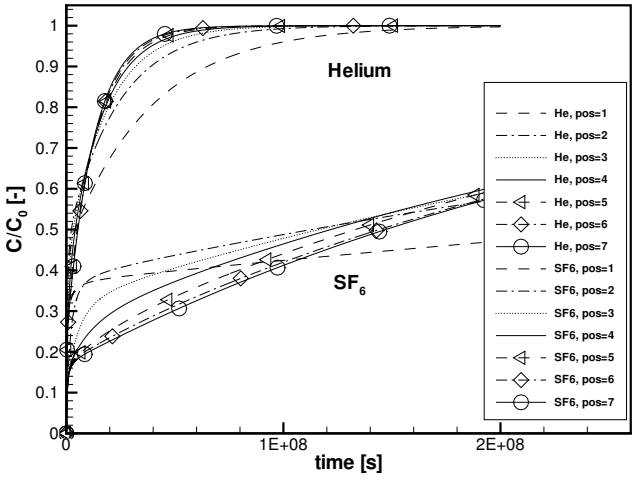

Fig. 5.73. Breakthrough curves for helium and SF_6, with the distance between the input and output ports set at 1 m.

For the present choice of boundary conditions, another phenomenon is observed. Since the boundary of the sandstone block is impervious, once the concentration front arrives at the boundary, the tracer is reflected. So the model starts to fill up with tracer until a concentration of 100% is reached at all nodes. Figures 5.74 (a) and (b) illustrate the distribution of the relative concentration of two different port configurations (*position 7* and *1*) for the same point in time, which is near the intersection point of these breakthrough curves (cf. Fig. 5.73). The reflection of the concentration front is demonstrated by the greater concentration for a port configuration in the center of the block (cf. Fig. 5.74 (a)) than for one close to the boundary (cf. Fig. 5.74 (b)).

The reflection of the concentration front can also be observed in the breakthrough curves (cf. Fig. 5.73): while in position 1, a concentration of 100 % is achieved latest, the breakthrough curves get steeper as the ports are moved

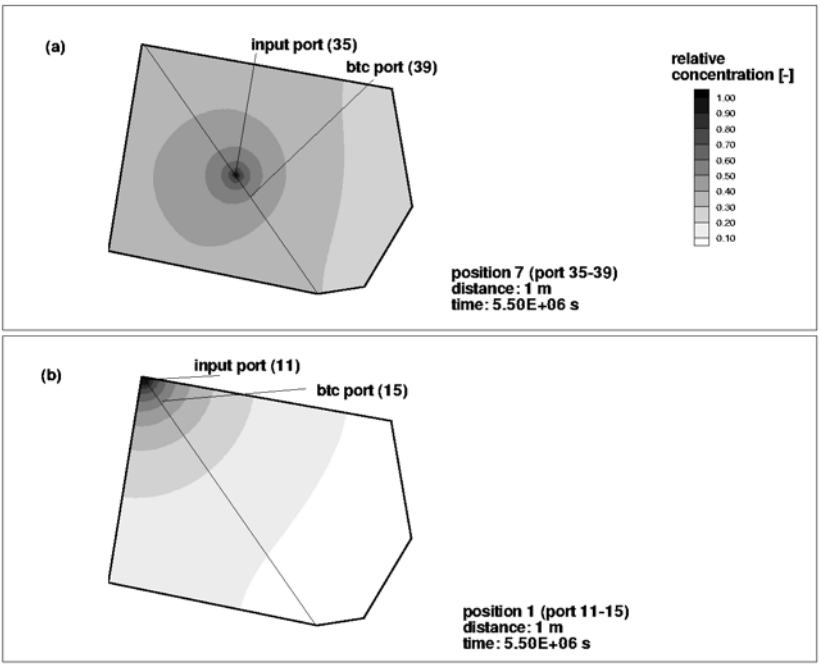

Fig. 5.74. Distribution of the relative concentration (helium) in the sandstone block for two different configurations: (a) *position 7*, (b) *position 1*.

toward the center of the block. At the more central positions, the boundaries are closer to the ports on all sides, so the reflected concentration fronts arrive at the output port earlier. To compare the influence of diffusion on the result, the simulations are carried out for two different tracers, helium and SF_6, the diffusion coefficient of the latter being much smaller than that of helium. Since the flow velocities in the porous medium are relatively small, the dominant transport phenomenon is diffusion. Therefore, the less important diffusion of SF_6 makes the concentration front move more slowly, so that the breakthrough curves are flatter than those with helium as a tracer (cf. Fig. 5.73). The results for the different distances between the input and output ports are essentially the same.

In Fig. 5.75, the breakthrough curves for helium are compared to those of a so-called dipole test, where the sandstone block is represented by a two-dimensional single-medium model, without the subdomain. The boundary conditions at the input and output ports are the same as those of the dual-media model (cf. Sect. 5.9.3).

Due to the impervious boundary, the discharge into the model at the input port must be equal to the one taken out of the model at the output port. No air is aspirated into the sandstone block, so that, in contrast to the simula-

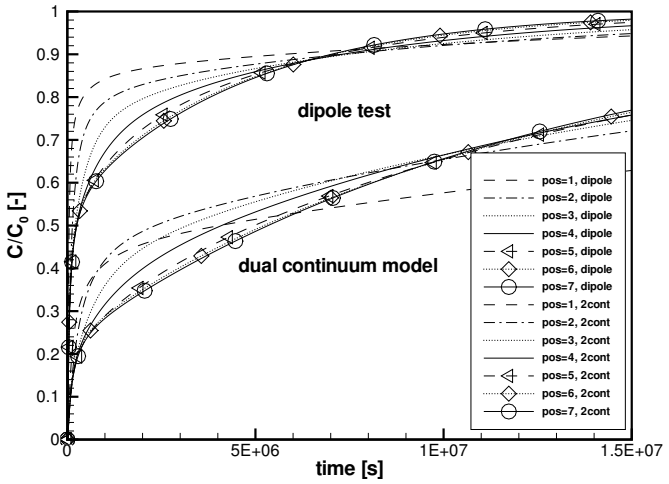

Fig. 5.75. Breakthrough curves of the dipole test compared to the dual medium model (distance between input and output ports = 1 m; helium tracer).

tions with the dual media model, no dilution occurs. Thus, the breakthrough curves of the dipole test are steeper.

Finally, the boundary conditions are changed to simulate pulse injections of a tracer. Figure 5.76 shows the resulting breakthrough curves for configurations with a distance of 3.00 m between the input and output ports, and the curves for the other configurations are essentially the same. The influence of the boundary is obvious as well. The shape of the part of the breakthrough curves before the peak is similar already from a distance of 1.00 m from the boundary onwards. The maximum and the tailing of the curves after the peak do not change significantly for configurations that place the input node more than four meters away from the boundary (from position 5 onwards). Again, the reflection of the concentration front is mirrored in the breakthrough curves, here by the bump in the descending part of the curves, which is especially pronounced for the configurations in the centre of the model area.

5.9.5 Conclusions

The investigation concerning boundary effects on the field-block scale demonstrates that the boundary effects are significant if the input and output ports

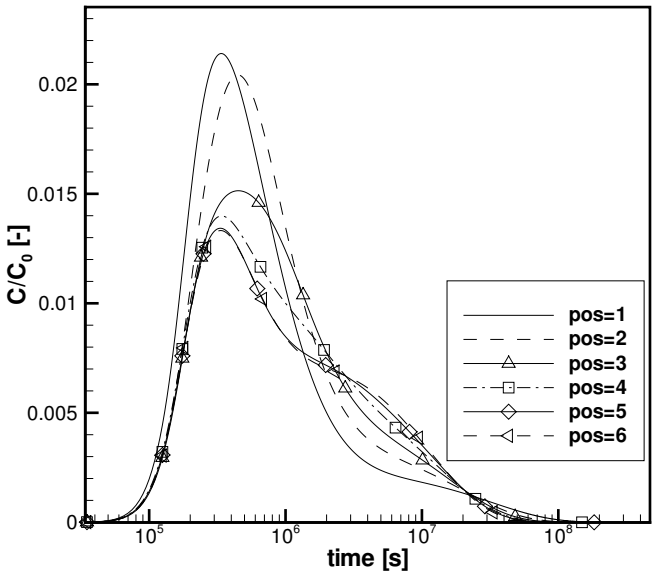

Fig. 5.76. Breakthrough curves for pulse injection (distance between input and output ports = 3 m; Helium tracer).

are positioned near the center of the sandstone block (pos. 4-pos. 6). However, the fact that the breakthrough curves calculated in the center of the block have almost the same shape and tailing (illustrating that the curves converge) shows that breakthrough curves from a test configuration at some distance to the boundary are influenced in a similar way by the boundary effects. This allows for an easier interpretation and makes them more comparable to other field-block scale studies.

The impacts of the boundaries are almost independent of the properties of the tracer (diffusion coefficient), the approach of the model (single-medium model or dual-media model) and the duration of the tracer injection (pulse injection or continuous infiltration).

The results of the numerical investigation of the boundary effects can be transferred to field experiments. They show that tracer experiments on the field block lead to more significant and comparable results when a port configuration in the center of the block is chosen. Therefore, the position of the ports should be chosen as described in Sect. 5.9.4.

Part III

Scale-Independent Approaches and Investigations